UV detection of IR and mm wave absorption in molecules and van der Waals complexes

by

Susannah G. Zhang

(Under the Direction of Henning Meyer)

Abstract

In this thesis, techniques for detecting IR and mm wave absorption are explored. The vacuum system techniques and experimental setups used to collect data are included. Then, chapter 3 demonstrates the effectiveness of measuring the near IR spectrum of NO-X complexes through excitation into the dissociation continuum of NO-Ne. In chapter 4, I show documentation of the first measured near IR spectrum of NO-He in the region of the first NO overtone transition using the same technique as chapter 3. The next chapter details the testing of a new experimental setup to perform mm-UV double resonance experiments. This new technique of measuring mm-wave absorption through Resonance Enhanced Multi-Photon Ionization (REMPI) allows analysis of fully resolved rotational structure.

Index words: Nitric Oxide, Nitric Oxide-Neon, Nitric Oxide-Helium, Carbon Monoxide, Molecular Beam, mm-wave Spectroscopy, IR Spectroscopy, UV Spectroscopy, van der Waals complex, Rydberg states, Dissociation Continuum

UV detection of IR and mm wave absorption in molecules and van der Waals complexes

by

Susannah G. Zhang

B.S.Ed, Indiana University of Pennsylvania, 2012

A Thesis Submitted to the Graduate Faculty
of The University of Georgia in Partial Fulfillment
of the
Requirements for the Degree

Master of Science

Athens, Georgia

2018

UV detection of IR and mm wave absorption in molecules and van der Waals complexes

by

Susannah G. Zhang

Major Professor: Henning Meyer

Committee: Phillip Stancil
Loris Magnani

Electronic Version Approved:

Suzanne Barbour
Dean of the Graduate School
The University of Georgia
August 2018

Acknowledgments

I sincerely want to thank the National Science Foundation, AIP Publishing, and Dr. Meyer.

TABLE OF CONTENTS

CHAPTER

List of Tables

List of Figures

Chapter 1

Introduction and Literature Review

This thesis will explore two different techniques for measuring either IR or mm wave absorption in NO-X complexes, where X is a rare gas atom, or molecules such as CO. The excited states of NO can exhibit either valence or Rydberg character. [4, 5] The lowest lying excited state, A state, has Rydberg character. Different Rydberg states of NO have been investigated though laser-induced fluorescence (LIF) and resonance enhanced multiphoton ionization (REMPI). [6, 7, 8] Likewise, the spectroscopy of NO-X in the excited states correlating with the NO Rydberg states has also been thoroughly studied. [9]

Evaluating the size of the Rydberg orbital and comparing with the van der Waals radii of the noble gas atoms, the Rydberg orbital is larger for all excited states except for the A-state. [9, 10]. For the $\tilde{A}$-state, the expectation value for the size of the Rydberg orbital (2.9 Å) is comparable or even smaller than the van der Waals diameter depending on the rare gas atom. [9] When Ne (1.54 Å radii) or He (1.4 Å radii) are the X in the NO-X complex, the $\tilde{A}$-state Rydberg orbital is comparable to the van der Waals diameter. [10] The bond between NO-X is then a balance between electron-electron repulsion of NO and X electron clouds and the weakly attractive dispersion interaction. The result is that the potential energy surface (PES) minimum of the $\tilde{A}$-state is shifted to larger intermolecular distances in comparison to the ground state and other higher Rydberg states. This shift means that increasingly favorable Franck-Condon factors can be found through increasing vibrational excitation or even through excitation into the $\tilde{A}$-state dissociation continuum. Investigations of excitation into the $\tilde{A}$-state dissociation continuum have been done for NO-Ar by Dr.

Meyer. [11] This method measured the IR absorption in the region associated with the first vibrational overtone of the NO monomer by exciting the vibrationally excited complex into the dissociation continuum of the electronic $\tilde{A}$-state using a 2+1 REMPI scheme. The resulting ionized NO fragment is then detected using a micro-channel plate detector (MCP). The following chapters contain results of excitation into the the $\tilde{A}$-state dissociation continuum of NO-Ne and NO-He. The increased Franck-Condon factors in the dissociation continuum cause this detection method have increased sensitivity and spectral resolution compared to IR-UV double resonance detection methods employed previously. [2, 12]

Another technique that is presented in this thesis is that of UV detected mm waves. Our technique demonstrates that the output of our mm wave generator (Anritsu + VDI Amplifier) has sufficient power to combine mm wave absorption spectroscopy with mass-specific time of flight (TOF) REMPI detection in conjunction with a pulsed molecular beam experiment. Since our Nd:YAG laser has a line width (0.1 cm-1) much smaller than the spacing of rotational transitions, individual levels can be probed independently. Additionally, temperatures achieved in the molecular beam are only a few Kelvin, which limits the initially populated levels and causes the majority of the initial population to be in the rotational ground state. To properly test the setup, we focused on the rotational transition of CO from J=0 to J=1 in the electronic ground state at 115 GHz. This transition is well known, so obtaining signals using hot-band UV detection from the J=1 rotational level demonstrates the validity of both the experimental concept as well as our experimental configuration.

This thesis is organized as follows. Chapter 2 outlines vacuum system techniques and experimental setups used to collect data. Then, chapter 3 demonstrates the effectiveness of measuring the near IR spectrum of NO-X complexes through excitation into the dissociation continuum of NO-Ne. In chapter 4, documentation of the first measured near IR spectrum of NO-He in the region of the first NO overtone transition is included. The next chapter details the testing of a new experimental setup to perform mm-UV double resonance experiments.

This new technique of measuring mm-wave absorption through REMPI allows analysis of fully resolved rotational structure.

Chapter 2

Experimental Setup

To conduct experiments, the equipment must be all set up. The following sections describe considerations for setting up a working experiment as well as the specifics of the equipment used to collect the data for this work.

2.1 Constructing a Vacuum System

Making a successful vacuum system requires pumping the air out of a volume in order to achieve a desired lower pressure. For instance, for mass spectrometers and molecular beam experiments, the desired pressure is in the 10^{-7} torr range [1]. To achieve this final pressure, you would need a pump such as a diffusion pump, which can operate between 10^{-3} - 10^{-7} mbar. Since these pumps cannot work against atmospheric pressure directly, another pump known as a backing pump must be used. For a backing pump, a two-stage rotary vane pump is a possible choice. In a system with a larger diffusion pump that will produce greater throughput in the foreline, using a roots-rotary combination to deal with the larger gas loads in order to keep the foreline pressures below the maximum throughput of the diffusion pump would be a wise choice.

If pumping of condensable vapors as well as gases must be done, then using a backing pump with a gas ballast is necessary. A gas ballast is a device developed in 1935 by Gaede to prevent the condensation of water vapor in a pump when the pump compresses the gas for elimination from the vacuum system [1]. The idea is to allow some air, or other gas if extra oxygen could increase the likelihood of explosion, to enter the pump during the compression stage in order to prevent the pressure from reaching the vapor's saturation pressure, thus condensing the vapor inside the pump. Without using a gas ballast, the pump would be limited by how much vapor it could pump by the following relation [1]:

$$\frac{p_{\text{vapor}}}{p_{\text{total}}} < \frac{p_{\text{sat}}}{p_{\text{sum}}}$$

$p_{\text{vapor}} =$ partial pressure of vapor at pump intake

$p_{\text{total}} =$ pressure of vapor and gases being pumped

$p_{\text{sat}} =$ saturation pressure of vapor at operating temperature

$p_{\text{sum}} =$ pressure at the exhaust of the pump plus pressure difference at both exhaust valve and filter

If the vapor of interest was water vapor at 70°C (typical operating temperature of pump), then the saturation pressure would be 312 mbar. Then knowing the sum of the pressures at the exhaust would tell you the maximum percentage of water vapor that can be pumped without condensation if a gas ballast is not used.

Another consideration for a vacuum system is what gauges to use at various positions in the vacuum system. Gauges such as a Bourdon gauge and a thermocouple gauge will be useful for determining the pressure as pumping starts until the chamber reaches 10^{-3} torr, when the diffusion pumps can be turned on. To determine if the desired final pressure of 10^{-7} torr has been reached, an ion gauge would be a good choice. Care needs to be taken when using a thermocouple or an ion gauge because they are generally calibrated for a certain gas, such as Nitrogen or air. If the thermal conductivity of the gas in the chamber is different from that of the calibrated gas, then the readings on the thermocouple gauge will not be completely accurate. Likewise, if the ionization probability of the gas is low, such as with Helium, the pressure readings on the ion gauge will be lower when in fact, the pressure inside is higher. To account for these differences in gas properties, there are correction factors that can be used. These correction factors can be seen in Table 2.1.

Table 2.1 Correction Factors for Property Dependent Pressure Measurements [1]

Prominent Gas	Calibrated Gas	
	N_2	Air
He	6.9	6.04
Ne	4.35	3.73
Ar	0.83	0.713
Kr	0.59	0.504
Xe	0.33	0.326
H_2	2.4	1.83

To better visualize the pressure ranges that each vacuum component operates in, refer to Figure 2.1.

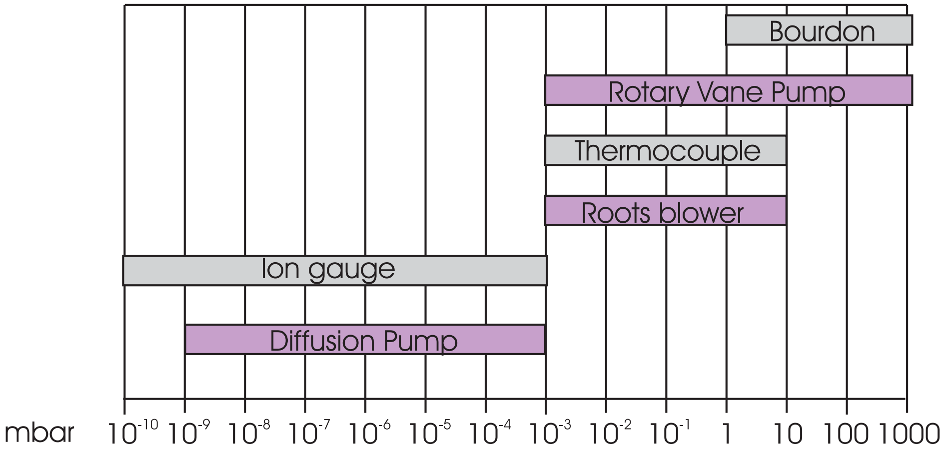

Figure 2.1 Laboratory Vacuum Component Pressure Ranges

In order to design a vacuum system for molecular beam experiments, the gas load of the molecular beam must be taken into account for choosing the necessary pumping speed to maintain a certain vacuum. Assuming a pulsed molecular beam where the temperature of the nozzle and the vacuum chamber are at room temperature, the molecular beam will have a gas load dependent on the pressure of the gas at the nozzle, p_n, the volume of the gas entering at each pulse, V_g, and the frequency of the pulses, f. To find the volume of the gas, we look at the radius of the nozzle for the molecular beam to get the area of the opening and multiply it by the most probable room temperature velocity of the gas beam and the pulse duration . Once the gas load is determined, the pumping speed of the pump needed can be calculated by dividing the gas load by the desired operating pressure of the chamber, p_c.

Working through an example of a pulsed Argon beam, we will use the following values:

Gas Constant	$R = 8.314 * 10^{-3}\ \frac{\text{amu (km/s)}^2}{\text{K}}$	Room Temperature	$T = 300$ K
Mass of Argon	$M = 40$ amu	Radius of Nozzle	$r = 2.5 * 10^{-4}$ m
Duration of Pulse	$t = 70\ \mu$s	Frequency of Pulse	$f = 10$ Hz
Backing pressure	$p_b = 20$ psi $= 1034$ torr	Desired Operating Pressure	$p_c = 10^{-5}$ torr

The pressure at the nozzle will be less than the backing pressure at the lecture bottle and will be taken to be half of the backing pressure ($p_n = p_b/2$) in the following example. Using all of these values, the minimum effective pumping speed of the diffusion pump that would be acceptable for this load would be [1]:

$$\begin{aligned} v &= \sqrt{\frac{2RT}{M}} = 352\ {}^{\text{m}}/_{\text{s}} \\ V_g &= Avt = (\pi r^2)vt = 4.84 * 10^{-9}\ \text{m}^3 = 4.84 * 10^{-6}\ \text{L} \\ Q &= p_n V_g f = 0.025\ \text{torr}\ {}^{\text{L}}/_{\text{s}} \\ S_{diff} &= \frac{Q}{p_c} = 2501\ {}^{\text{L}}/_{\text{s}} \end{aligned}$$

Choosing the proper backing pump for this diffusion pump is also important. If the maximum throughput, Q_{max}, of the diffusion pump is 3.5 torr ${}^{\text{L}}/_{\text{s}}$, and the maximum forepressure, p_f, is 0.55 torr, then the minimum effective pumping speed of a backing pump would be:

$$S_{bp} = \frac{Q_{max}}{p_f} = 6.36\ {}^{\text{L}}/_{\text{s}} = 22.9\ {}^{\text{m}^3}/_{\text{hr}}$$

Another important factor for constructing a vacuum system is the diameter of the foreline. Knowing the length needed for the foreline, L (in cm), to go from the diffusion pump to the backing pump and that the conductance, C of that line must be at least twice the pumping speed of the backing pump, the diameter can be found. If the foreline distance is 1 m and the backing pump has a pumping speed of 40 $^{\mathrm{m}^3}/_{\mathrm{hr}}$ (11.1 $^{\mathrm{L}}/_{\mathrm{s}}$), then the diameter of the line should be [13]:

$$D = \left(\frac{CL}{180\, p_f}\right)^{1/4} = 2.18 \text{ cm}$$

Now consider a differentially pumped vacuum system. To construct such a set up, the diameter of the skimmer and the position of the skimmer must be determined. If the chamber with the detector is desired to be at 10^{-7} torr and contains a 2500 $^{\mathrm{L}}/_{\mathrm{s}}$ pump with a liquid N_2 trap of conductance 133 $^{\mathrm{L}}/_{\mathrm{s}}$, the diameter of the skimmer can be found [13].

$$\begin{aligned}
S_{d.eff} &= \left(\frac{1}{S_{det}} + \frac{1}{C_{trap}}\right)^{-1} = 126\ ^{\mathrm{L}}/_{\mathrm{s}} \\
Q_{det} &= P_{det} S_{d.eff} = 1.26 * 10^{-5} \text{ torr } ^{\mathrm{L}}/_{\mathrm{s}} \\
C_{sk} &= \frac{Q_{det}}{P_{source} - P_{det}} = 1.27\ ^{\mathrm{L}}/_{\mathrm{s}} \\
A_{sk} &= C_{sk}\left[3.7\sqrt{\frac{T}{M}}\right]^{-1} = 0.126 \text{ cm}^2 \\
d_{sk} &= \sqrt{A_{sk}\left(\frac{4}{\pi}\right)} \approx 4 \text{ mm}
\end{aligned}$$

As for the position of the skimmer, the best position for the optimum intensity of a pulsed molecular beam is likely around 3 to 4 cm from the nozzle [14].

2.2 Vacuum Systems

2.2.1 Molecular Beam Machine - Test Apparatus

The vacuum system used for the mm-REMPI experiments is denoted as the "Test Apparatus." The apparatus consists of two differentially pumped vacuum chambers: the source and the detector chamber. The source chamber contains two 2500 L/s diffusion pumps (Varian VHS 6), while the detector chamber contains a single 2500 L/s diffusion pump with a liquid N_2 cooled baffle to prevent oil back streaming. These diffusion pumps are all backed by a 40 m^3/hr two-stage rotary vane pump (Leybold Trivac D40). The two vacuum chambers are separated by wall with a 4 mm skimmer to collimate the molecular beam as it passes into the detector chamber. A horizontal cut of the apparatus can be seen in Figure 2.2.

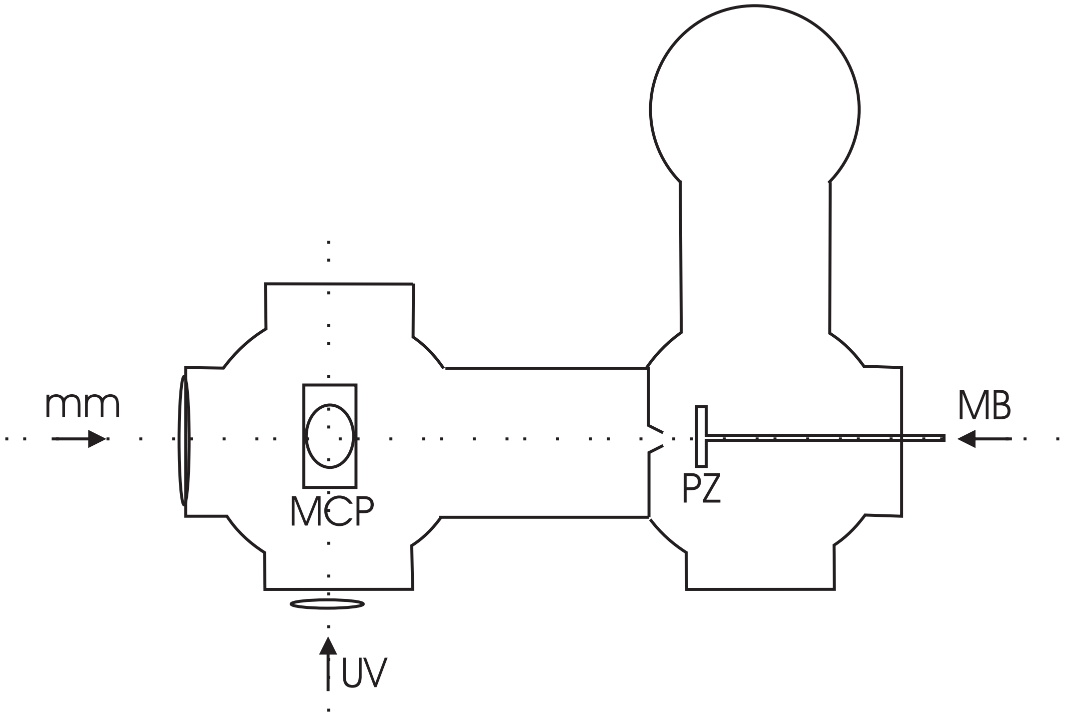

Figure 2.2 Schematic of Test Apparatus. PZ = piezoelectric valve, MB = Molecular beam, mm = millimeter waves, UV = ultraviolet for REMPI, MCP = micro-channelplate detector.

The molecular beam for our experiments enters the source chamber from a home-built Piezo valve (PZ). The gas undergoes supersonic expansion and adiabatic cooling as it passes through a 0.5 mm diameter hole at a frequency of 10 Hz with a pulse duration of approximately 70 μs. From the source chamber, the molecular beam is collimated by the skimmer as it enters the detector chamber. Typical operating pressures for the two chambers are 2 x 10^{-5} torr for the source chamber and 7 x 10^{-7} torr for the detector chamber. Once in the detector chamber, the molecules are ionized and accelerated upward by a bottom plate towards a microchannel plate detector (MCP), which uses electron amplification to generate a signal. This signal is then amplified and recorded using a digital oscilloscope (Tektronix TDS684C).

2.2.2 Molecular Beam Machine - Scattering Apparatus

The vacuum system used for the IR-UV and dissociation continuum experiments is denoted as the "Scattering Apparatus." The apparatus consists of two differentially pumped vacuum chambers, just like the Test Apparatus. The source chamber contains a 11,000 L/s diffusion pump (Balzers DIF 500) with a liquid N_2 baffle to avoid oil back streaming. The molecular beam can enter the source chamber from either a home-built Piezo source or a commercial Jordan source (Jordan Co.). These two sources are positioned at opposite ends of the chamber and each have skimmers for collimation of the beam as it enters the detector chamber. The detector chamber contains a 3000 L/s diffusion pump (Leybold 3000) with a liquid N_2 cooled baffle to prevent oil back streaming. These diffusion pumps are all backed by a roots-rotary pump combination (Edwards EH250 - Edwards E2M40). Once inside the detector chamber, there is an array of electrodes that help to guide the ions to the MCP detector. A schematic can be found in Figure 2.3 along with the electrode arrangement in Figure 2.4.

The molecular beam sources for this apparatus is very similar to the Test Apparatus.

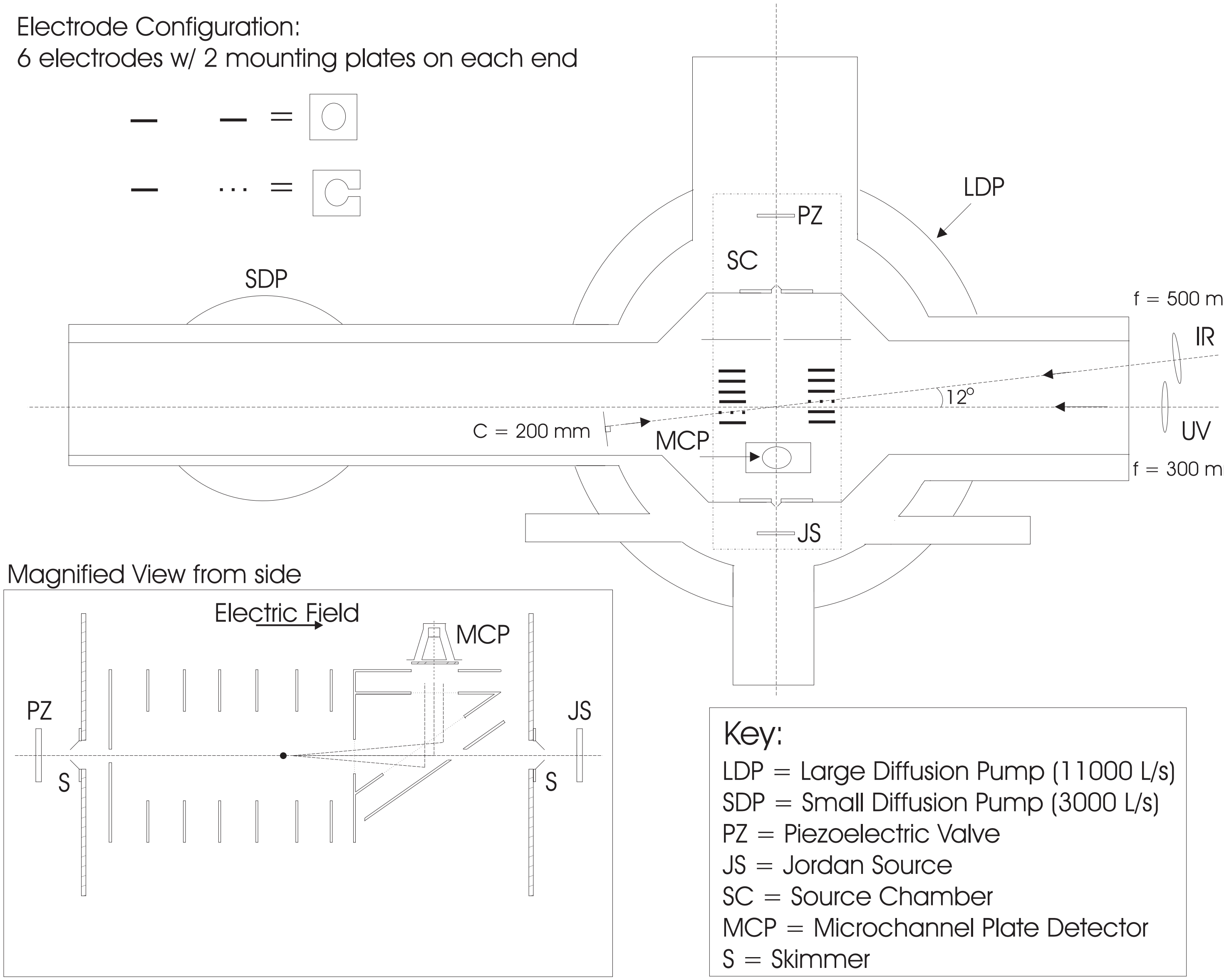

Figure 2.3 Schematic of Scattering Apparatus.

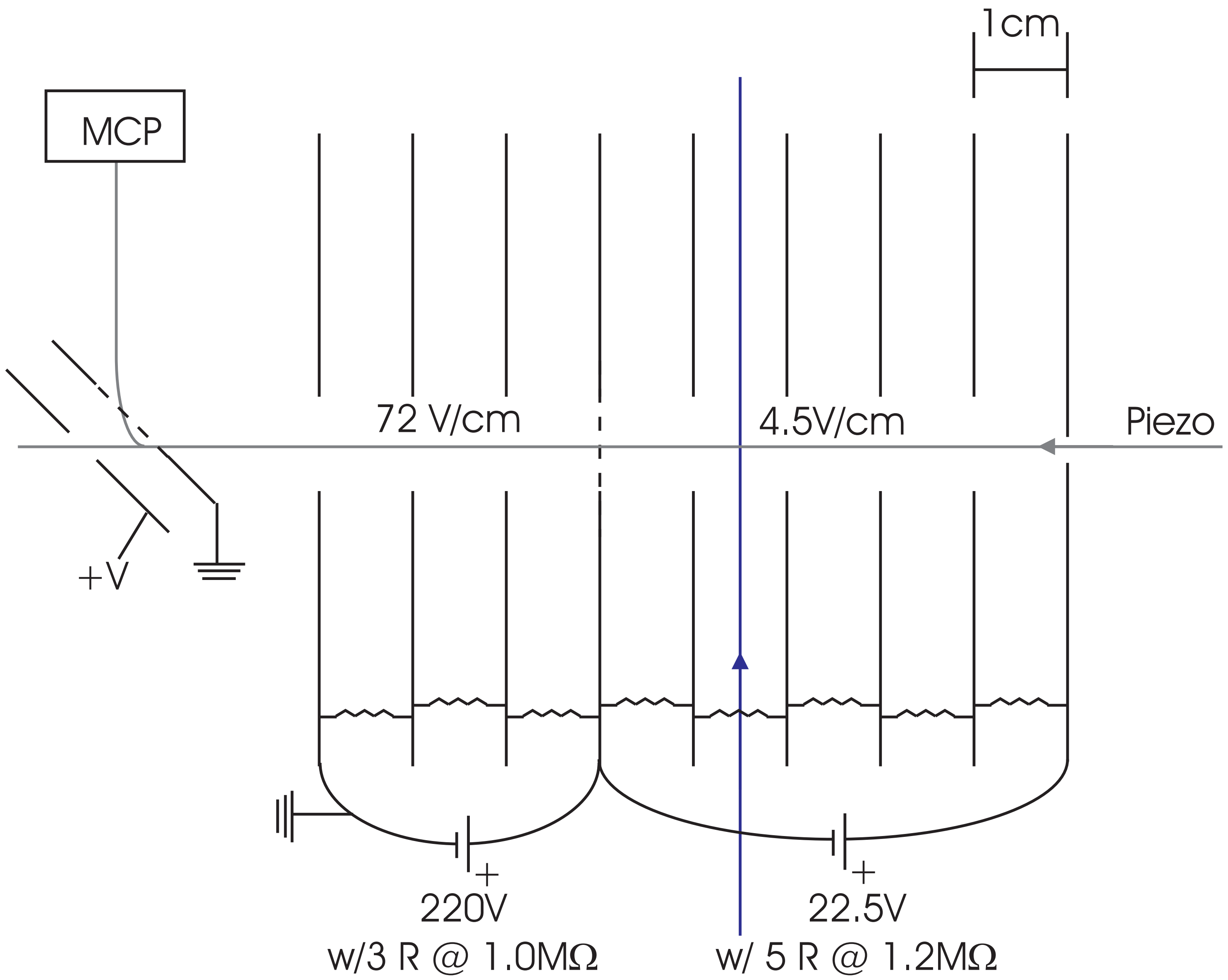

Figure 2.4 Detailed Schematic of Electrode Arrangement.

From either source, the gas undergoes supersonic expansion and adiabatic cooling as it passes into the source chamber at a frequency of 10 Hz with a pulse duration of approximately 60-80 μs. From the source chamber, the molecular beam is collimated by a 4 mm skimmer as it enters the detector chamber. Typical operating pressures for the two chambers are 4 x 10^{-7} torr for the source chamber and 3 x 10^{-7} torr for the detector chamber. Once in the detector chamber, the molecules are ionized and accelerated towards the MCP by an electrode arrangement.

The electrode arrangement can be seen in the bottom left of Figure 2.3 with a more detailed set up of the connections shown in Figure 2.4. In the arrangement, seven metal plate electrodes placed 15 mm apart and measuring 150 x 150 x 1.6 mm each contain a 100 mm diameter hole in the center for the molecular beam to pass through. The electrodes are connected by 1 MΩ resistors and receive 300 V from a DC power supply, which generates the acceleration field directing the ions towards the MCP. Under the MCP, the ions encounter an electrostatic mirror, two electrodes separated by 10 mm at 300 V, that accelerates the ions upward towards the detector. The signal in the MCP is amplified and then recorded by a digital storage oscilloscope (Tektronix TDS3054B).

2.3 Laser Systems

2.3.1 Nd:YAG

Nd:YAG (neodymium-doped yttrium aluminium garnet; Nd:$Y_3Al_5O_{12}$) lasers contain a gain medium crystal (YAG) with a small amount of the yttrium atoms being replaced by triply ionized neodymium (Nd(III)). These lasers can output 1064 nm (fundamental) light as well as 532 nm through frequency doubling and 355 nm through sum frequency generation. To obtain population inversion, the Nd ions go through a four level system depicted in Figure 2.5. The flash lamp optically pumps the ions from the ground state, $^4I_{9/2}$, into an excited state through principle absorption bands in the red and near infrared ($\nu_1 \approx 14285$ cm^{-1}). These excited ions quickly relax to the $^4F_{3/2}$ level, which is a metastable state with a lifetime of 230 μs. The most probable lasing transition from the metastable state with the highest gain is to the $^4I_{11/2}$ state, emitting a photon with a wavelength of 1064 nm. This state has a very short lifetime before the ions relax back to the ground state; therefore, the population in the $^4I_{11/2}$ state remains small. This causes population inversion to occur between the ground state and the upper lasing state ($^4F_{3/2}$).

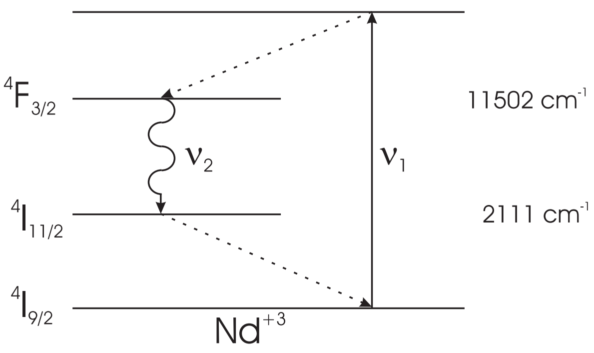

Figure 2.5 Four level system of Neodymium ions in Nd:YAG crystal.

To facilitate this population inversion and stimulated emission , a Q-switch (See dotted box in oscillator at bottom of Figure 2.6 or 2.7) is used to prevent oscillation until optimum population inversion is achieved. A Q-switch consists of a Pockels Cell, a Quarter-wave plate, and a polarizer. The Pockels Cell works like a Quarter-plate when voltage is applied on it (Q-switch open) and has no effect on the beam when there is no voltage (closed). The polarizer only allows horizontally polarized light through, so when the Q-switch is closed, no light will escape causing no oscillation to occur. After the flash lamps excite the Nd ions and build a large population inversion (200 μs), the Q-switch is opened (5 μs at 4 kV) stimulating the emission of photons and allowing oscillation. This quick release in energy results in an output pulse around 680 mJ/pulse, which is useful for nonlinear processes such as second harmonic generation (SHG) and sum frequency generation (SFG) [15].

In our lab, we have two main kinds of Nd:YAG lasers that pump various dye lasers and IR lasers. Each system is described in detail in the following sections.

2.3.1.1 Spectra Physics GCR170-10

One of the Nd:YAG lasers employed in our lab is the Spectra Physics GCR170-10. A schematic showing the Spectra Physics laser can be seen in Figure 2.6. This laser is capable of outputting 1064 nm, 532 nm, and 355 nm; however, we do not use the 1064 nm output in our experiments. Inside the Spectra physics laser, the 1064 nm generated from the oscillator goes through SHG in a KDP (Potassium Dihydrogen Phosphate) crystal to create horizontally polarized 532 nm. Then vertically polarized 1064 nm and the 532 nm undergo SFG in a KDP to create vertically polarized 355 nm. The 355 nm is used for pumping a Dye Laser (Laser Analytical System (LAS) LDL205) containing Coumarine 460 (450 - 484 nm lasing range) as the gain medium, whose output can be frequency doubled to produce horizontally polarized 225-242 nm (bandwidth: 0.15 cm^{-1}). The 532 nm output is used with the output of the LAS laser to generate horizontally polarized 245-252 nm (bandwidth: 2.5 cm^{-1}) through SFG in a BBO (Beta Barium Borate) crystal. The UV systems are described in more detail in Section 2.3.2.

2.3.1.2 Continuum Powerlite 7010 and 8000

Two other Nd:YAG lasers that are used in our lab are the Continuum Powerlite 7010 and the Continuum Powerlite 8000. Both of these lasers are very similar in that they both produce 1064 nm and 532 nm. Specifically for the Continuum 7010, the 1064 nm undergoes SHG in a KDP crystal to generate vertically polarized 532 nm. The 532 nm output is used to pump another Dye Laser (Radiant Dyes RDP02N) containing DCM (624 - 686 nm lasing range) as the gain medium, which can be frequency doubled to obtain horizontally polarized light at about 326 nm (bandwidth: 0.15 cm^{-1}). The UV systems are described in more detail in

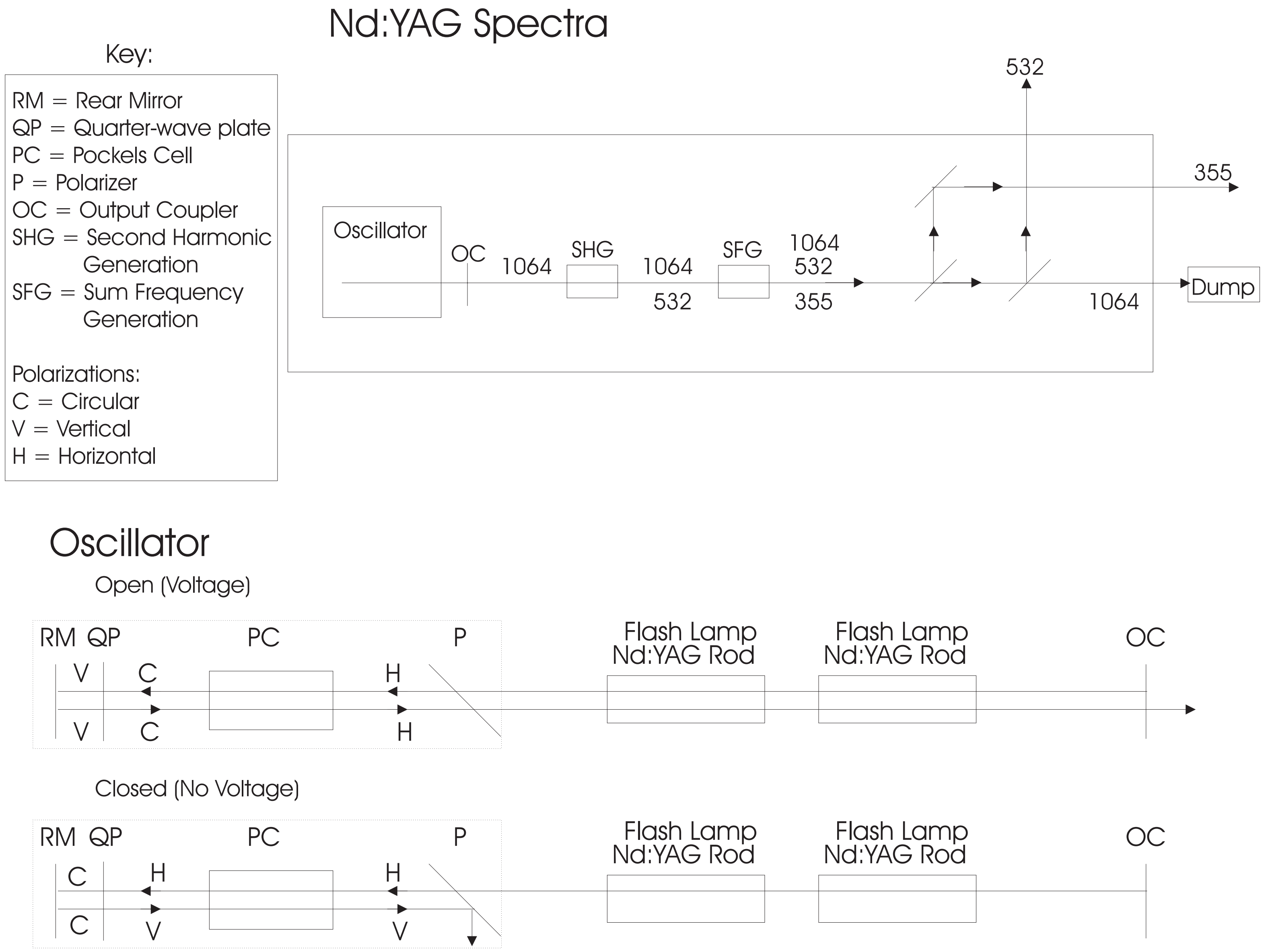

Figure 2.6 Schematic of the Spectra Physics GCR170-10.

Section 2.3.2.

The main difference between the 7010 and the 8000 model is that the Continuum 8000 uses a continuous-wave seed laser (Continuum SI-2000) with a very narrow linewidth. The high reflecting mirror in the oscillator can be moved by a piezoelectric element in order to tune the cavity length to the seed frequency. Then the seed laser sends a resonant frequency into the oscillator of the laser at the time the Q-switch opens. This pulse that is six orders of magnitude stronger than any background noise in the cavity causes a pulse to be generated from the gain medium faster, and with a narrower linewidth, than through noise emission. All the energy from the gain medium is extracted by this pulse, leading to single frequency output [16]. A schematic showing the Continuum Powerlite 8000 laser can be seen in Figure 2.7.

2.3.2 Ultraviolet Laser System

To make ultraviolet light for our experiments, we use one of two Dye laser systems, LAS or RDP mentioned in Section 2.3.1. The path of the pump beam for either of these systems can be seen in Figure 2.9. As the beam from a Nd:YAG laser enters, it is split so that 8% of the pump beam goes into the lower part of the oscillator/preamplifier cell (C1). Once inside the oscillator (dotted box in lower portion of Figure 2.9), the beam is partially reflected back into dye cell C1 by the output coupler (OC). From there, the beam enters a prism beam expander (PDE) that expands the beam vertically by a factor of 12 and translates it downward by about 11 mm. The expanded beam fully illuminates a blazed grating (G), causing higher resolution and smaller bandwidth, and bounces from the tuning mirror (TM) back to the grating where the beam goes back to C1 to be amplified again and head towards the preamplification stage at the upper part of C1. Before preamplification, the beam goes through two Brewster plates, which filter out s-polarized light and allow p-polarized to go through. The 92% of the pump beam that does not go into the oscillator goes through a

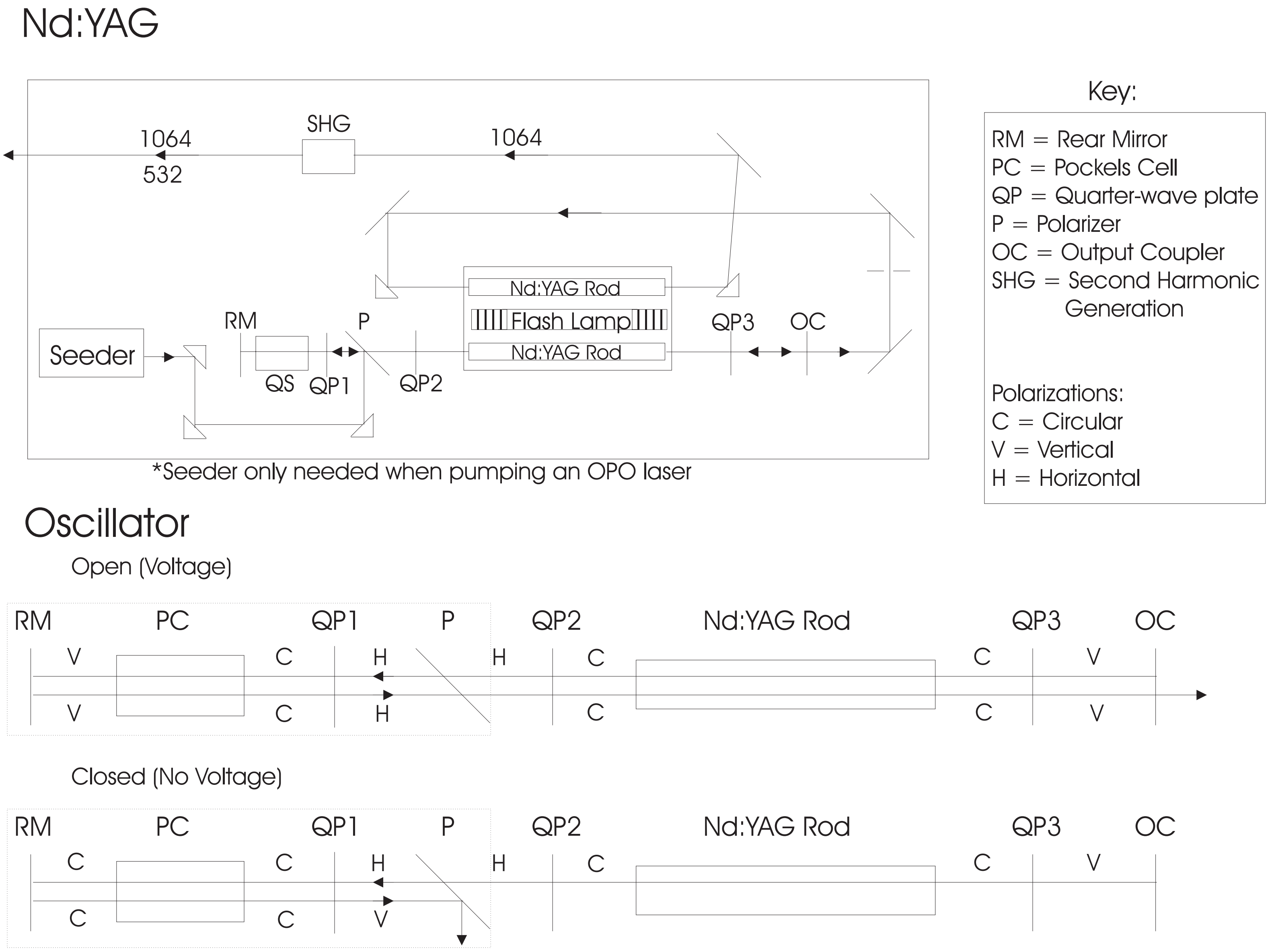

Figure 2.7 Schematic of Continuum Powerlite 8000.

delay line and is split into a preamp beam (20%) directed to the upper part of dye cell C1 and an amplifier beam (80%) directed towards main amplifier cell (C2). Both cells are tilted by 6° to avoid extra oscillation from the cell windows. Wavelength selection, λ, is done through rotation of the TM and can be determined by the grating equation shown in Equation 2.1 and depicted in Figure 2.8. α is the angle between the normal of the grating and the normal of the TM, while β is the angle of incidence of the pump beam onto the grating (85°). m is the diffraction order and d is the grating spacing ($4.2 * 10^{-4}$ mm) [Man].

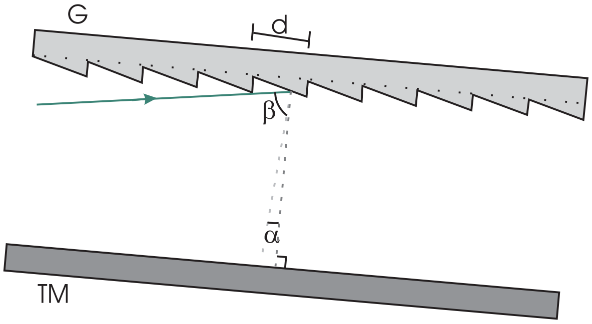

$$m\lambda = d\,[\sin(\alpha) + \sin(\beta)] \qquad (2.1)$$

Figure 2.8 Grating equation notation

2.3.3 Infrared Laser System

IR is generated through pumping the MIRAGE 3000 laser with 532 and 1064 nm from the Nd:YAG Continuum 8000.

2.3.3.1 OPO Laser System: MIRAGE 3000

The horizontally polarized fundamental (1064 nm) and vertically polarized second harmonic (532 nm) of the Nd:YAG laser enter the MIRAGE and are split by a dichroic mirror. The second harmonic goes through a telescope into the Optical Parametric Oscillator (OPO) where a horizontally rotating KTP (potassium titanyl phosphate) crystal generates horizontally polarized signal around 750 nm. Remembering that polarization that is perpendicular

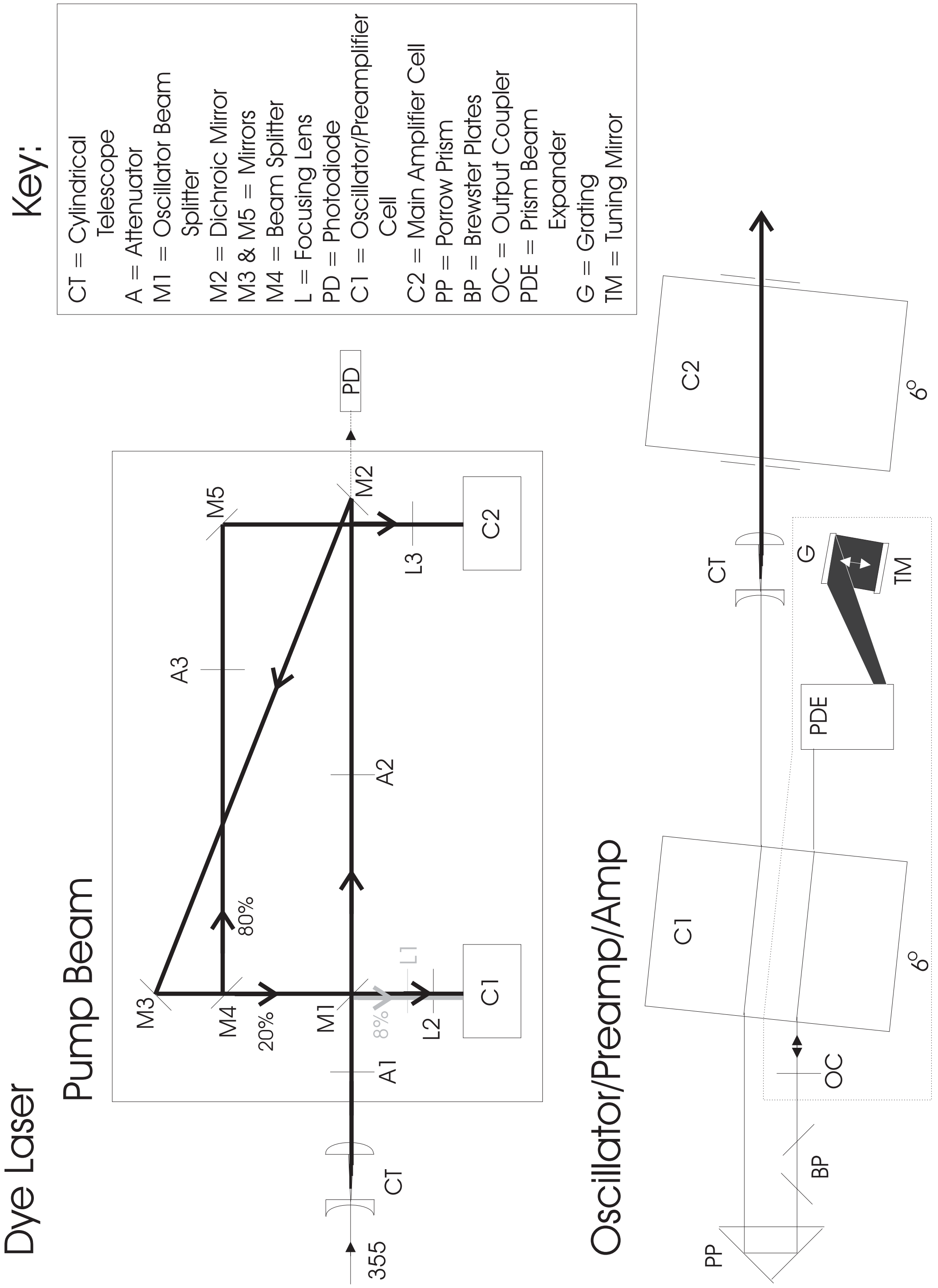

Figure 2.9 Schematic of the Dye Laser system.

to the crystal's plane of rotation is denoted as ordinary polarization, thus polarization parallel to that plane of rotation is denoted as extraordinary polarization, we have the following denoting "o" as ordinary and "e" as extraordinary.

$$\begin{array}{ccccc}\text{o (pump: 532 nm)} & \rightarrow & \text{e (signal: 750 nm)} & + & \text{o (idler: 1.5 }\mu\text{m)}\\ \text{vertical} & & \text{horizontal} & & \text{vertical}\end{array}$$

The signal of the OPO then goes into the Nonresonant Oscillator (NRO) along with 532 nm from the Nd:YAG to create a 1.5 μm idler that is vertically polarized. This idler becomes the signal for the Optical Parametric Amplifier (OPA) stage, which uses the 1.5 μm and 1064 nm from the Nd:YAG in vertically rotating crystals to generate a horizontally polarized idler around 2.7 μm.

$$\begin{array}{ccccc}\text{e (idler: 1.5 }\mu\text{m)} & + & \text{o (1064)} & = & \text{o (signal: 2.7 }\mu\text{m)}\\ \text{vertical} & & \text{horizontal} & & \text{horizontal}\end{array}$$

The paths of these beams can be seen in Figure 2.10.

2.3.3.2 Optical Parametric Oscillator (OPO)

The OPO uses a near grazing incidence design, which can be seen in the lower left-hand corner of Figure 2.10. The components of the OPO are: a rear mirror, KTP crystal, grating (5 cm with 1800 lines/mm), and a tuning mirror. These elements undergo active mode locking with a piezo element where the cavity length is actively-stabilized in order to output a single longitudinal mode of zeroth order while diffracted first order light is reflected back into the cavity with the tuning mirror. The output of each mode reflects off the grating at a different angle, and changing the cavity length changes the reflected angle from the grating. Using a split photodiode, the output pointing of the laser can be used to generate an error signal that provides information to maintain the cavity length at the proper value [17].

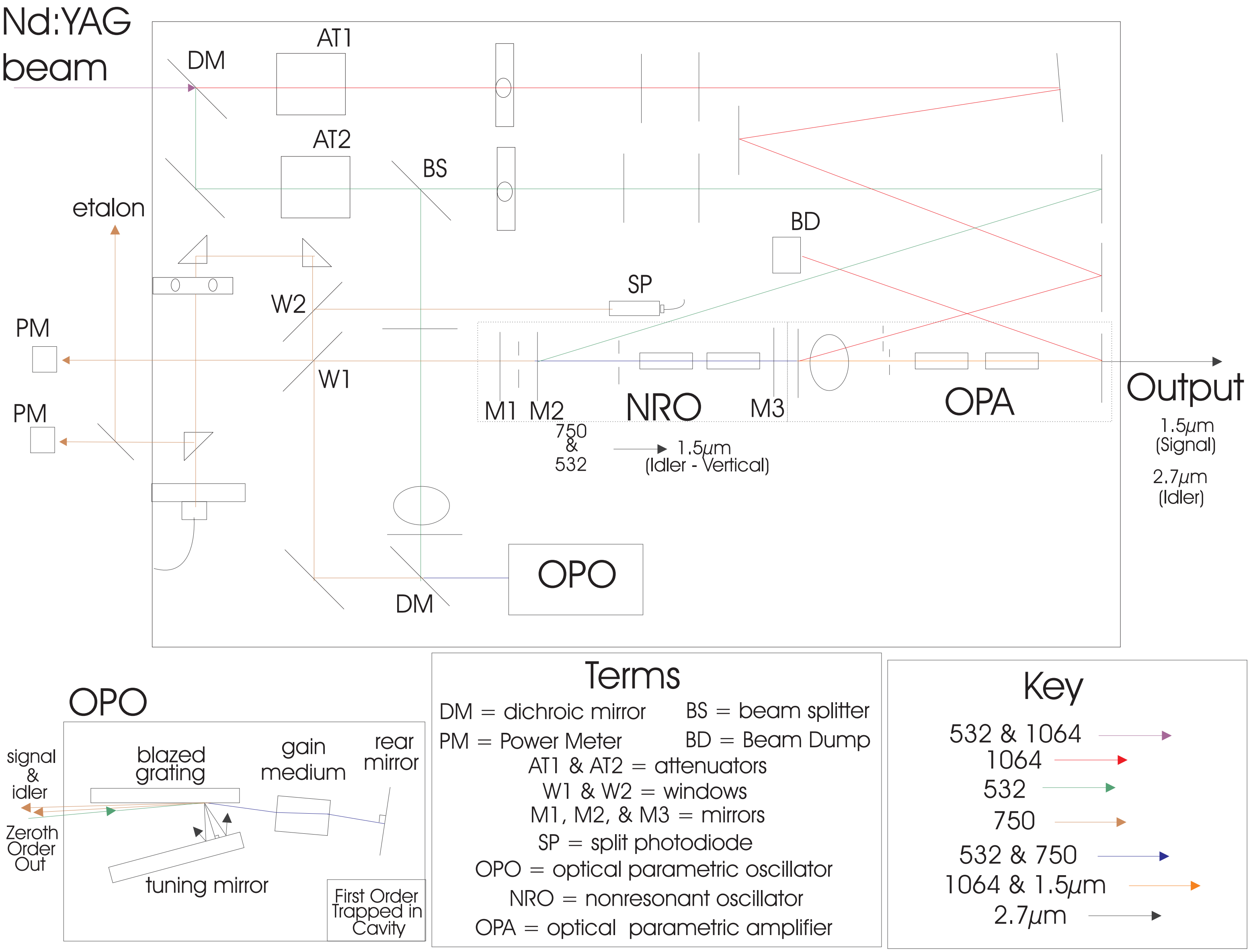

Figure 2.10 IR system diagram including wavelengths and polarizations

2.3.4 Lens Alignment Considerations

Deciding on a lens and where it should be placed as well as its orientation in the laser beam takes many considerations. One of those is the Chromatic Aberration and the other is where possible focus spots will occur. The following sections will take a look at each of these considerations.

2.3.4.1 Chromatic Aberration

Using a website database of index of refraction curves such as:
`http://refractiveindex.info/legacy/?group=CRYSTALS&material=SiO2&option=Ghosh-o&wavelength=0.632`

And using the Lensmaker Formula:

$$P = \frac{1}{f} = (n-1)\left[\frac{1}{R_1} - \frac{1}{R_2} + \frac{(n-1)d}{nR_1R_2}\right] \tag{2.2}$$

Where:

P = lens power
f = focal length
n = index of refraction
R_1 = radius of curvature of lens surface closest to light source
R_2 = radius of curvature of lens surface furthest from light source
d = thickness of lens

We can measure the Chromatic Aberration, focal length change caused by change of incident wavelength, of a lens for 326nm and 225nm.

For a Plano-convex lens, let us assume that the light is hitting the convex side first so as to minimize the effects of monochromatic aberrations.

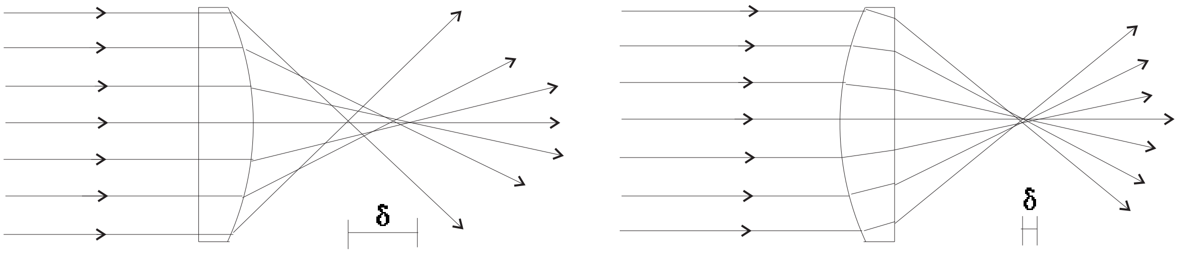

Figure 2.11 Monochromatic Aberrations: Change in focal length of a single wavelength hitting a Plano-convex lens at different points under its two possible orientations. The orientation on the right has a smaller spread than the orientation on the left.

What would be the Chromatic Aberration in a Plano-convex lenses made of Quartz (SiO_2) labeled with a focal length of 200 mm? Note that focal length labels on lenses are normally for about 632nm. With that information, we can get the index of refraction of that wavelength in Quartz and use it to determine the radius of curvature of the lens.

Since the surface furthest from the light source is a vertical line, $R_2 = \infty$. This causes:

$$\frac{1}{R_2} \approx \frac{(n-1)d}{nR_1R_2} \to 0 \tag{2.3}$$

So the Lensmaker Formula, (2.2), greatly simplifies to:

$$\frac{1}{f} = (n-1)\left(\frac{1}{R_1}\right) \tag{2.4}$$

Solving that equation for R_1:

$$R_1 = (n-1)f \tag{2.5}$$

Since the focal length that the manufacturer assigns a lens is given through using 632 nm, it will be necessary to know the index of refraction for that wavelength in order to calculate the radius of curvature.

The index of refraction for 632 nm in SiO_2 is:

$$n_o = 1.54263 \qquad n_e = 1.55168 \tag{2.6}$$

For now, let's focus on the ordinary beam. So the radius of curvature of the lens is:

$$R_1 = (n-1)f = (1.54263 - 1)200 \text{ mm} \approx 108.526 \text{ mm} \tag{2.7}$$

Now with the radius of curvature, we can find the focal lengths of two different wavelengths such as 326 nm and 225 nm.

The index of refraction for 326 nm in SiO_2 is:

$$n_o = 1.57074 \qquad n_e = 1.58075 \tag{2.8}$$

So using the simplified form from (2.4) and the radius of curvature from (2.7), the focal length of 326 nm in this lens is:

$$\frac{1}{f} = (n-1)\left(\frac{1}{R_1}\right) = (1.57074 - 1)\left(\frac{1}{108.526 \text{ mm}}\right) \rightarrow f \approx 190.149 \text{ mm} \tag{2.9}$$

The index of refraction for 225 nm in SiO_2 is:

$$n_o = 1.61906 \qquad n_e = 1.63086 \tag{2.10}$$

Therefore, the focal length of 225 nm in this lens is:

$$\frac{1}{f} = (n-1)\left(\frac{1}{R_1}\right) = (1.61906 - 1)\left(\frac{1}{108.526 \text{ mm}}\right) \rightarrow f \approx 175.308 \text{ mm} \tag{2.11}$$

The difference between the focal point of 326 nm and 225 nm can then be found by subtracting (2.9) and (2.11):

$$\delta = 190.149 \text{ mm } - \ 175.308 \text{ mm } \approx 14.8 \text{ mm} \tag{2.12}$$

Now let us do the same thing for a lens labeled with a focal length of 300 mm: Find R_1 using the index of refraction for 632 nm in SiO_2:

$$R_1 = (n-1)f = (1.54263 - 1)300 \text{ mm} \approx 162.789 \text{ mm} \tag{2.13}$$

Find the focal length of 326 nm:

$$\frac{1}{f} = (n-1)\left(\frac{1}{R_1}\right) = (1.57074 - 1)\left(\frac{1}{162.789 \text{ mm}}\right) \rightarrow f \approx 285.224 \text{ mm} \tag{2.14}$$

Find the focal length of 225 nm:

$$\frac{1}{f} = (n-1)\left(\frac{1}{R_1}\right) = (1.61906 - 1)\left(\frac{1}{162.789 \text{ mm}}\right) \rightarrow f \approx 262.962 \text{ mm} \tag{2.15}$$

Then take the difference in the focal lengths:

$$\delta = 285.224 \text{ mm } - \ 262.962 \text{ mm } \approx 22.3 \text{ mm} \tag{2.16}$$

So now we see the Chromatic Aberration for each lens and also see that when:

$$f \uparrow \ \delta \uparrow \tag{2.17}$$

2.3.4.2 Determining Focus Spots

Another application for the lens maker equation is locating focus spots from back reflections. This is very important because you do not want a focus spot where another optic is located.

First example: Telescope Setup 1

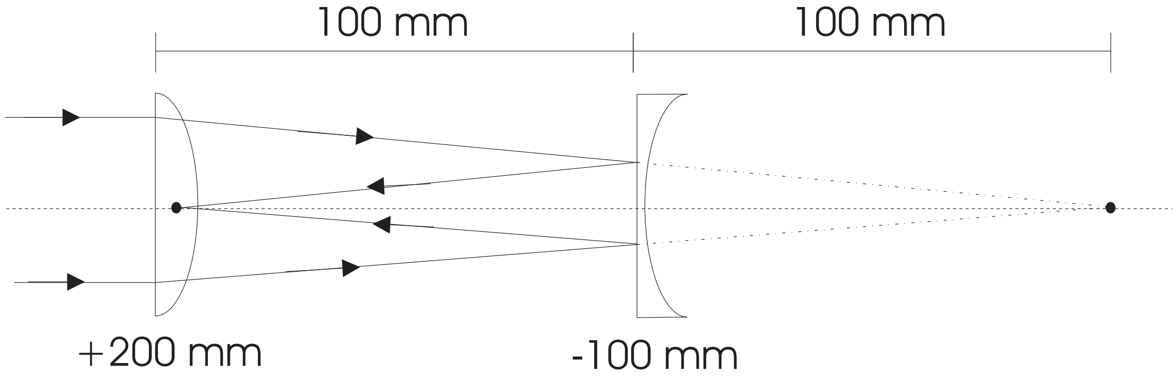

Figure 2.12 Telescope Setup 1.

Looking at the focus from the first Converging Lens:

$$\frac{1}{p} + \frac{1}{q} = \frac{1}{f} \rightarrow \frac{1}{\infty} + \frac{1}{q} = \frac{1}{200 \text{ mm}} \rightarrow q = 200 \text{ mm past the converging lens} \tag{2.18}$$

Then treating the next lens at a flat mirror to look at the possible reflection caused from the first surface of diverging lens. The object is 100 mm past the “mirror”, so the focus of the reflection is at 100 mm in front of the mirror, which is the same location as the converging lens. NOT GOOD! As for the second surface of the diverging lens, the incoming beam will be collimated. When the reflection goes through the diverging lens again, it will diverge and not form a focus.

Second example: Telescope Setup 2

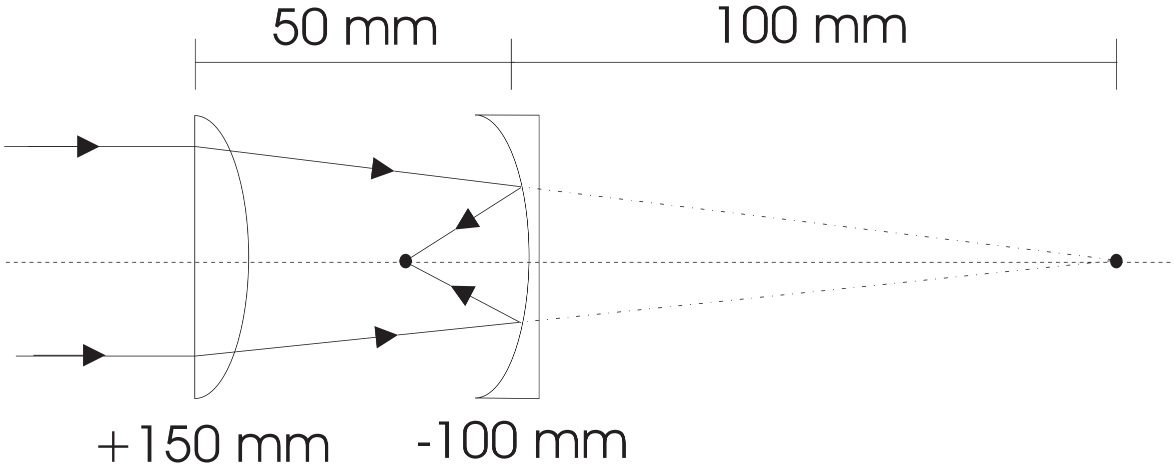

Figure 2.13 Telescope Setup 2.

Looking at the focus from the first Converging Lens:

$$\frac{1}{p}+\frac{1}{q}=\frac{1}{f}\rightarrow\frac{1}{\infty}+\frac{1}{q}=\frac{1}{150\text{ mm}}\rightarrow q=150\text{ mm past the converging lens}\qquad(2.19)$$

Then treating the next lens as a curved mirror to look at the possible reflection caused from the first surface of diverging lens. We know the focal length of the lens, but that is not the focal length of the curved surface because the lens focal length assumes the light going through a material, so the index of refraction is taken into account in the determination of that focal length. Since we want to look at the reflection, the light will not go through the lens, thus we need to use the lens maker equation to figure out the radius of curvature of this "curved mirror" from this diverging lens.

$$\frac{1}{f_d}=(n-1)\left[\frac{1}{R_1}-\frac{1}{R_2}+\frac{(n-1)d}{nR_1R_2}\right]\rightarrow\frac{1}{-100\text{ mm}}=(1.5-1)\left[\frac{1}{R_1}\right]\rightarrow R_1=-50\text{ mm}\qquad(2.20)$$

This means that the focal length of the "curved mirror" is:

$$f_c = \frac{R_1}{2} = -25 \text{ mm} \tag{2.21}$$

However, due to the sign convention of curved mirrors, the focal length should be positive because it is a concave mirror. $f_{cm} = 25$ mm.

Now we can calculate the location of the focused reflection.

$$\frac{1}{d_o}+\frac{1}{d_i} = \frac{1}{f_{cm}} \rightarrow \frac{1}{-100 \text{ mm}}+\frac{1}{d_i} = \frac{1}{25 \text{ mm}} \rightarrow d_i = 20 \text{ mm in front of curved surface} \tag{2.22}$$

2.3.5 Delay Generators

The timing of each component is important for a successful experiment. To regulate the timing for the lasers and the molecular beams, we use BNC555 (Berkeley Nucleonics Corporation, BNC1 and BNC2) and DG535 (Stanford Research Systems, DG535_1 and DG535_2) delay generators. BNC1 is used as the master and controls signaling the BNC2 and DG535_1, while the timing for the DG535_2 is provided from DG535_1. The BNCs can send out pulse signals and the DG535s can send out edge signals and pulse signals. Generating these signals is done through transistor-transistor logic (TTL) circuits where anything below 1 V is considered off (0) and 4-5 V is on (1). Delays used can be seen in Tables 2.2, 2.3, 2.4, and 2.5, and a schematic of all their connections can be seen in Figure 2.14.

For the IR-UV experiments, a 10 μs pulse is sent from BNC1 Channel B to the Jordan source or from BNC1 Channel A to the Piezo source to start the molecular beam. Another 10 μs pulse is sent at 965.6 μs from the DG535_2 Channel AB to fire the flashlamps in the Nd:YAG Continuum 8000 followed by a pulse 257 μs later to fire the Q-switch in order to pump the MIRAGE laser. Additionally, two edge pulses come from the DG533_1 to control the flashlamps (C: 1017.9 μs) and the Q-switch (D: 1212.8 μs) in the Spectra Physics laser to pump the LAS Dye laser. An example of the different delays used in a IR-UV double resonance experiment can be seen in Figure 2.15(a).

The mm-wave experiments in the Test Apparatus sometimes use the LAS or the RDP dye laser. In each case, the molecular beam is controlled through the BNC2 Channel C, which sends out a 10 μs pulse. The LAS laser is timed using the delays for the Spectra Physics laser mentioned in the previous paragraph, and a schematic can be found in Figure 2.15(c). For the RDP dye laser, the BNC2 Channels A and B send out pulses to the flashlamps and Q-switch, respectively, starting at 816 μs followed by a 287 μs wait time for maximum population inversion. Figure 2.15(b) shows an example delay scheme for operating the RDP dye laser.

Table 2.2 BNC1 - Master and Molecular Beams for Scattering Apparatus

Channel	Delay (μs)	Width (μs)	Impedance	Amplitude	Active	Device
A	See Table 2.7	10	high Z	TTL	high	Piezo (scatt)
B	See Table 2.7	10	high Z	TTL	high	Jordan
C	T + 110.806	200	high Z	TTL	high	BNC2
D	T + 0	10	high Z	TTL	high	DG535_1

Table 2.3 BNC2 - Continuum 7010 and Molecular Beam for Test Apparatus

Channel	Delay (μs)	Width (μs)	Impedance	Amplitude	Active	Device
A	T + 816.00	10	high Z	TTL	high	Lamp Fire (7010)
B	T + 1103.00	10	high Z	TTL	low	Q-switch (7010)
C	See Table 2.6	10	high Z	TTL	high	Piezo (test)
D	T + 1115.30	10	high Z	TTL	low	Lamp Charge (7010)

Table 2.4 DG535_1 - Spectra Physics, Mirror for Scattering Apparatus, and Side pulse for Test Apparatus

Channel	Delay (μs)	Width (μs)	Impedance	Amplitude	Norm/Inv	Device
T0	T		high Z	TTL	normal	DG535_2
A	T + 1212.683		high Z	TTL	inverted	Side Pulse (test)
B	T + 1214.198		high Z	TTL	inverted	Mirror Pulse (scatt)
AB	T + 1212.683	1.515	high Z	TTL	normal	Boxcar (Spectra)
C	T + 1017.944		high Z	TTL	normal	Lamp Fire (Spectra)
D	T + 1212.89		high Z	TTL	normal	Q-switch (Spectra)

Table 2.5 DG535_2 - Continuum 8000 and Boxcar for MIRAGE

Channel	Delay (μs)	Width (μs)	Impedance	Amplitude	Norm/Inv	Device
A	T + 965.6		high Z	TTL	normal	Boxcar (MIRAGE)
AB	T + 965.6	10	high Z	TTL	normal	Lamp Fire (8000)
CD	T + 1222.6	10	high Z	TTL	normal	Q-switch (8000)
D	T + 1232.6		high Z	TTL	inverted	Lamp Charge (8000)

Table 2.6 Molecular Beam Delays for Test Apparatus: BNC2 Channel C

Gas Mixture	Delay (μs)
5% CO in Ar	686.0
5% CO in He	814.0
5% NO in Ar	678.0

Table 2.7 Molecular Beam Delays for Scatt Apparatus: BNC1 Channel A (Piezo) and B (Jordan)

Gas Mixture	Jordan (μs)	Piezo (μs)
2% NO 6% CH_4 in He	742.0	
2% NO 3% CH_4 in He	750.512	
2% NO in He	752.52	
1% NO in H_2	798	
5% NO in Ne		856.812
2% NO 4% N_2 in He	736.512	
2% NO 4% CO in He	732.512	
2% NO 2% N_2O in He	724.512	
2% NO 1% N_2O in He	751.512	
2% NO 1% CO_2 in He	746.512	
2% NO 4% C_2H_6 in He	746.512	

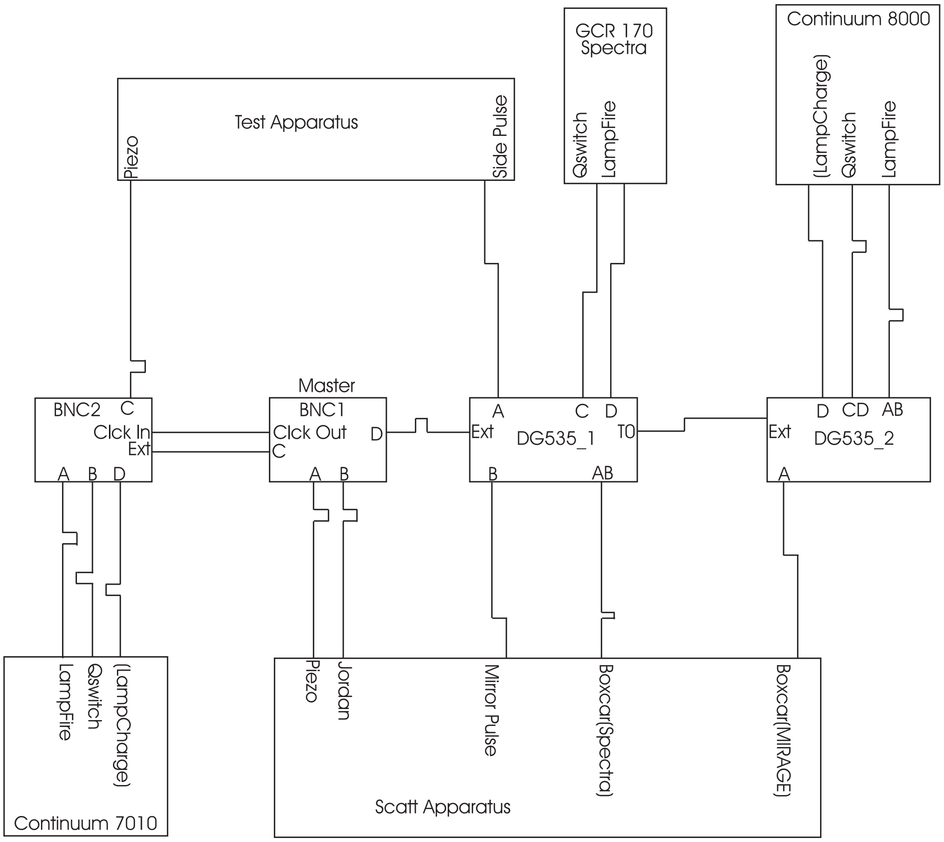

Figure 2.14 Delay Generator Connections

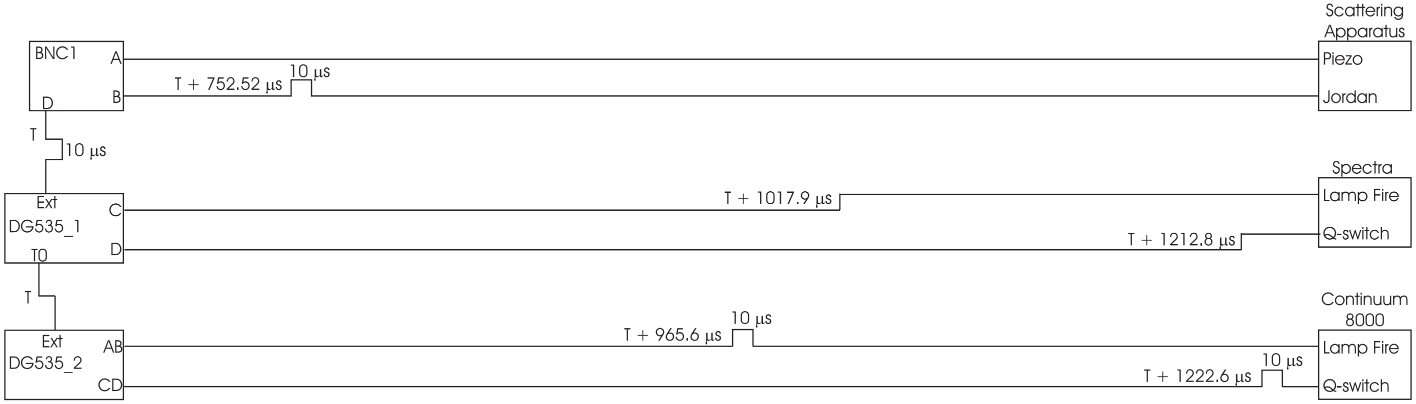

(a) Delays for Scattering Apparatus: NO-He expansion from Jordan

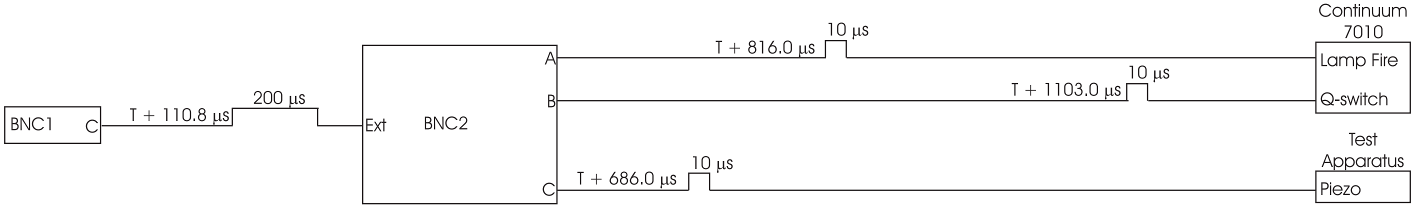

(b) Delays for using RDP: 5% CO in Ar

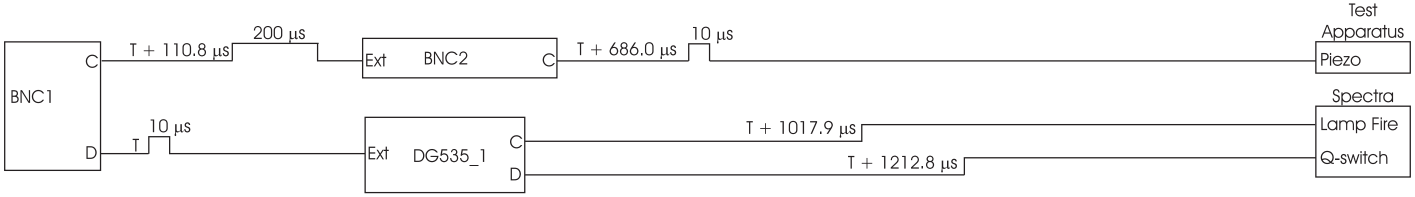

(c) Delays for using LAS: 5% CO in Ar

Figure 2.15 Schematics for Experimental Timings

Chapter 3

The near-IR spectrum of NO($\tilde{X}$ $^2\Pi$)-Ne detected through excitation into the $\tilde{A}$-state continuum: A joint experimental and theoretical study[1]

---

[1] J. Kłos, S.G. Zhang, and H. Meyer. J. Chem. Phys. **144**, 114307 (2016). Reprinted here with permission of the publisher.

Abstract

We present new measurements of the near IR spectrum of NO-Ne in the region of the first NO overtone transition. The IR absorption is detected by exciting the vibrationally excited complex to the $\tilde{A}$-state dissociation continuum. The resulting NO(A) fragment is subsequently ionized in the same laser pulse. Spectra of the two lowest bands, A and B, are recorded. The spectra are compared with calculated spectra based on bound states derived from a new set of high level *ab initio* potential energy surfaces (PES). For the calculation, the PESs are used with either fixed NO intermolecular distance or averaged for the vibrational states of NO ($\tilde{X}$, v=0 or 2). Spectra based on the new PESs reproduce the experimental spectra better than theoretical spectra based on the older PESs of Alexander et al. (*J. Chem. Phys.* **2001**, 114, 5588). Especially, spectra based on the two different vibrationally averaged PESs show a marked improvement in comparison to the one based on the fixed internuclear NO-distance. A fitted set of spectroscopic constants allows to reproduce most of the finer details of the measured spectra. Monitoring simultaneously the NO fragment ion and the parent ion channels while scanning the UV wavelength through the NO A-X hot-band region enabled us to confirm the NO-Ne $\tilde{A}$-state dissociation limit of 44233±5 cm^{-1}. These measurements also confirm the absence of a structured NO-Ne spectrum involving the $\tilde{A}$-state.

3.1 INTRODUCTION

The NO molecule exhibits a multitude of excited electronic states with either valence or Rydberg character.[4, 5] In particular, different Rydberg states have been exploited in laser-induced fluorescence (LIF) and resonance enhanced multi-photon ionization (REMPI) studies for state specific NO product detection.[6, 7, 8] Therefore, it is not surprising that also the spectroscopy of NO-rare gas complexes in excited electronic states correlating with its Rydberg states have been investigated extensively.[9] While earlier work concentrated on the NO-Ar complex[18, 19], also complexes with other rare gas atoms like Ne, Kr, and Xe have been studied.[9, 20, 21] Up to date, there has been no report of any structured spectrum of the NO-He complex.

Using an effective principal quantum number, expectation values for the size of the Rydberg orbital have been calculated to range from 2.9 Åfor the A-state to 6.3 Åfor the E-state.[9] These values can be compared to the van der Waals radii used for the noble gas atoms which range from 1.4 Åfor He to 2.3 Åfor Xe.[10] Except for the A-state, the lowest state with Rydberg character, the Rydberg orbital is larger than the van der Waals diameter of the atomic partner. We therefore expect the noble gas atom to form a strongly bound complex with the NO cation which is surrounded by an electron in the Rydberg orbital. This is consistent with the observed large red shifts of the spectra in higher Rydberg states for all the NO-noble gas systems (Ne through Xe).[9, 20, 21]

For the case of the electronic $\tilde{A}$-state, the situation is not as clear. In this case, the radius of the Rydberg orbital is comparable or even smaller than the van der Waals diameters. Therefore, the bond is controlled by the balance between dispersion interaction and the electron - electron repulsion of the electron clouds of the neutral NO and the noble gas atom. As a result, the potential minimum in the $\tilde{A}$-state is shifted to larger distances in comparison to the higher Rydberg states with stronger ionic interaction. Structured spectra correlating with the NO A-state have been reported only for the complexes with Ar, Kr, and Xe.[22, 23, 24, 25] The spectra of the two latter complexes are characterized by a large number of vibrational bands which increase in intensity with increasing frequency until the intensity vanishes abruptly at the dissociation limit of the $\tilde{A}$-state surface. This behavior confirms that also the repulsive wall of the $\tilde{A}$-state surface is shifted outward causing the Franck-Condon factors to increase with increasing vibrational excitation.

Clearly, the increase in Franck-Condon factors will not stop with the excitation into the $\tilde{A}$-state continuum. Interestingly, one of the first experimental observations of NO-Ar relied on fragment NO(A) fluorescence detection following excitation to the repulsive wall of the $\tilde{A}$-state surface.[26] It also facilitates the investigation of the kinetic energy release of NO fragments resulting from the $\tilde{A}$-state dissociation of various NO van der Waals complexes.[27, 28, 29, 30]

Recently, we have shown for NO-Ar, that it is possible to detect the near IR absorption spectrum of the complex by exciting it into the $\tilde{A}$-state dissociation continuum and subsequently ionizing the resulting NO(A) fragment.[11] Because of the increased Franck-Condon factor, this detection method is significantly more sensitive (at least for some bands of the complex) than the IR-UV double resonance schemes employed in our earlier work.[2, 12] In addition, the increased sensitivity allows us to operate the IR laser in a configuration which provides significantly improved spectral resolution.

In principle, this detection scheme could be applicable also to the study of other NO-X complexes, for example with X being a closed-shell molecule. A potential drawback is the loss of mass selectivity by detecting the NO ion rather than the parent ion of the complex. Because of spectral congestion due to NO-Ar absorption, it will not be possible to use Argon as the seed gas for the molecular beam expansion. As an alternative, we explored the possibility to use Neon instead. When employing the method of dissociation detection to record the near IR spectrum of the NO-Ne complex, we find an intense spectrum of NO-Ne in the NO^+ ion channel. Furthermore, dissociation detection appears to allow for a more uniform detection of the IR absorption than was found in the 2+1 REMPI detection schemes employed in our earlier work.[2] The increased sensitivity of the dissociation detection method allowed us to remeasure the spectrum of the NO-Ne complex with greatly improved signal-to-noise ratio and spectral resolution. The results are presented in this article.

For the NO-Ne complex, Ayles et al. showed theoretically that transitions in the bound-bound $\tilde{A}$-$\tilde{X}$ system of NO-Ne are characterized by very small Franck-Condon factors.[31] These findings are consistent with the fact that, up to date, no structured $\tilde{A}$-$\tilde{X}$ spectrum of NO-Ne has been detected. In the case of the NO-Ar complex, we showed that the $\tilde{A}$-$\tilde{X}$ system can be excited very efficiently beyond the $\tilde{A}$-state dissociation limit at which the observed signal switches simply from the parent ion channel NO^+-Ar to the fragment channel NO^+.[11] Experimentally, the study relied on the preparation of the complex in a ro-vibrational state of the NO($\tilde{X}$, v=2)-Ar surface shifting the electronic absorption from the origin band near 225 nm to the hot-band region at 245 nm. As a result, large background signals from the NO monomer could be avoided.

In reexamining the near IR spectroscopy of the NO-Ne complex, we confirm the assertion of Ayles et al. that a structured $\tilde{A}$-state spectrum is too weak to be detected experimentally. Scanning the UV wavelength through the A-X hotband region while simultaneously monitoring both the parent as well as the NO monomer ion, indeed no indication of a signal in the parent channel was found while there is a strong signal from NO-Ne in the NO^+ channel for frequencies significantly above the $\tilde{A}$-state dissociation limit.

The interaction of NO-Ne in its electronic ground state has been investigated by several groups theoretically and experimentally. Stolte et al. deduced from the analysis of experimentally determined integral scattering cross sections a well-depth of 50 cm^{-1} and a minimum distance of 3.11 Å.[32] The analysis of vibrational structures in an excited state of NO-Ne correlating with the NO H-state in 2+1 REMPI UV spectra yielded a lower binding energy of around 45 cm^{-1}.[33] First spectroscopic information about bound levels of the electronic ground state surface could be derived in an IR-UV double resonance experiment.[2, 34] Rotationally resolved spectra were analyzed with the help of quantum mechanical bound state calculations based on a high level *ab initio* set of potential energy surfaces (PESs) yielding a dissociation energy of $D_0 = 29\ \text{cm}^{-1}$. While the calculated spectrum showed overall good agreement with the experimental spectrum, some details in particular for the excited bands were not in good agreement. At least some of these discrepancies must be attributed to the relatively poor spectral resolution in the measured spectra which also prevented us from completing a satisfactory spectroscopic fit of the spectrum.

Endo et al. used a fit of Fourier transform microwave (FTMW) data to determine the interaction potential for the NO-Ne complex.[35] In this approach, a high level *ab initio* potential surface is calculated and represented by analytical functions which are subsequently optimized in a fit of the resulting bound states to the experimental spectrum. The potential function was optimized by fitting MW transitions between the lowest rotational energy levels with $|P|=0.5$. Bound states of the resulting set of PESs are in excellent agreement with the measured transition frequencies. The dissociation energy of 33.7 cm^{-1} for this surface is slightly larger than the one reported by Alexander et al.[34] Experimentally, a dissociation energy of 28.6 cm^{-1} has been measured in an ion imaging study by Holmes-Ross and Lawrance.[29]

Here, we report another high-quality *ab initio* set of PESs for the NO-Ne system in its electronic ground state employing the RCCSD[T] method (sometimes called CCSD+T(CCSD) in which the triple corrections are calculated without single excitations) using an aug-cc-pVTZ basis set with midbond functions. We used the RCCSD[T] variant of the triple correction family due to the fact that the interaction energies were more attractive and Rezac et al. (Ref. [36]) found that the use of the CCSD[T] method gives smaller errors than the CCSD(T) variant which usually is considered a gold standard. These PESs are similar to the ones reported recently by Cybulski and Fernandez who used the RCCSD(T) method with a d-aug-cc-pVQZ basis set, extended by midbond functions.[37] These two sets of PESs have been used to calculate differential scattering cross sections and compared with high resolution scattering data by Zastrow et al.[38] The authors find excellent agreement with the experimental data for both sets of PESs, but also for the high level *ab initio* PESs of Sumiyoshi and Endo (Ref.[35]). When comparing the data with cross sections based on the older *ab initio* PESs of Alexander et al. in Ref. [34], discrepancies in the position of the diffraction oscillations were found. This is consistent with earlier scattering results by Kim et al. where also deviations in the differential cross sections between theory and experiment were found.[39] On the other hand, Brouard et al. found good agreement between their experimental scattering data and theoretical cross sections calculated for the older set of surfaces.[40]

The new set of PESs reported here has been also used in the theoretical calculation of the electronic excitation of NO-Ne from its ground state to excited electronic states correlating with different Rydberg states of NO.[31, 41] While no comparison of predicted spectra is possible for the $\tilde{A}$-state, excellent agreement was found for the $\tilde{C}$-$\tilde{X}$ spectrum of NO-Ne confirming the high quality of both the ground and excited state surfaces. As another application, theoretical studies of the excited state dynamics of NO in solid Ne could also benefit from using more exact PESs for NO-Ne in different electronic states rather than resorting to simple Lennard-Jones type potentials.[42] In this context, the expanded Rydberg orbital and the resulting shift of the repulsive wall in the $\tilde{A}$-state surface is usually referred to as 'bubble formation'.[43, 44]

In order to assess the quality of the new PESs further, it is desirable to compare spectra generated from its bound states with experimental spectra. In this article, we present the comparison of new experimental spectra with calculated spectra based on the results of bound state calculations for the new set of high level *ab initio* PESs averaged for the appropriate

NO vibrational levels. The theoretical results are also used as the input for a spectroscopic fit of the experimental spectra.

The paper is organized as follows. Relevant details of the experiments are described in Section 3.2. Section 3.3 summarizes the results and their discussion. It presents the analysis of the IR spectra recorded in the region of the first overtone transition of NO. The analysis starts with the fit of the calculated energy levels in terms of spectroscopic constants. The latter are then used to calculate different spectra which can be compared with the measured ones. It also summarizes the results for the wavelength dependence of the NO-Ne ionization efficiency in its electronic $\tilde{A}$-state. Conclusions are presented in Section 3.4.

3.2 EXPERIMENT

The experiments are performed in a molecular beam scattering apparatus which has been described in detail previously.[45, 46, 47] Briefly, a mixture of 5% NO in Neon is expanded either from a home-built piezo electric valve ([ger]) or from a Jordan molecular beam source at a backing pressure of 2.5 bar and a repetition rate of 10 Hz. The 50-80 μs long pulses travel from the source chamber through skimmers into the detection chamber. The pulses are intersected under 78^o by the IR laser beam and under 90^o by the UV probe laser. Both laser beams are focussed onto the molecular beam with lenses of 500 mm focal length. Typically the UV laser pulse is fired about 15 ns after the IR laser pulse. Both laser pulses are polarized horizontally, i.e. in the plane defined by the laser beams which includes the molecular beam axis. The lasers intersect the molecular beam inside an electrode arrangement which accelerates the ions created by laser photo-ionization towards an electrostatic mirror and subsequently towards a micro-channel plate (MCP) detector. The detector signal is amplified and recorded with a digital storage oscilloscope (Tektronix TDS3054B).

Single longitudinal mode IR radiation around 2.7 μm is generated with an optical parametric oscillator (OPO) (Continuum Mirage 3000) pumped with an injection seeded Nd:YAG laser (Continuum 8000). For the experiments reported here, the first amplification stage of the OPO is operated in a single forward path configuration improving the spectral resolution by almost a factor of two to about 0.015 cm^{-1} (450MHz) while the output energies are reduced to about 1.5 mJ per pulse. A relative frequency scale is established by monitoring the fringes of an external etalon (FSR =0.200918 cm^{-1}) and assuming a linear frequency change between two consecutive fringes.[2] During a scan of the IR laser, we also monitor the first overtone vibrational spectrum of NO in a photoacoustic cell in order to establish the absolute frequency scale.[48, 49]

UV probe radiation around 245nm (200-300 μJ/pulse) is produced by sum frequency generation in betabarium borate (BBO) of the output of a dye laser (LAS LDL 20505) operating on the dye Coumarin 460 with the residual second harmonic of the Nd:YAG pump laser (Spectra Physics GCR170-10). The resulting dye laser output allows us to cover the wavelength range of the hot-band transition NO(A, v'=0) ← NO(X, v"=2).[50] The bandwidth of the hot-band UV radiation is found to be around 2.0-2.5 cm^{-1}. The dye laser output also allows us to generate UV radiation near 225nm through second harmonic generation in the same BBO crystal.[12] Because of the failure of the original control electronics for this dye laser, we replaced the two stepping motors used for rotating the tuning mirror and non-linear optical crystal assembly with new motors from Oriental Motors including drivers.[hmw] The motor drivers are directly controlled by our own experimental software package via a USB to serial interface.

3.3 Results and Discussion

3.3.1 Spectroscopic fit of energy levels

The assignment of different ro-vibrational bands of the NO-Ne complex in the region of the first NO overtone, has been given in our earlier work.[2] The near IR spectrum is dominated by two bands, labeled A and B, which are assigned as the origin band in terms of the van der Waals vibrational modes (we ignore here the overtone vibration of the NO chromophore) and an excited band involving one quantum of rotation around the intermolecular axis of the near T-shaped complex. Although not a strictly good quantum number, the projection P of the total angular momentum (with quantum number J) onto the intermolecular axis greatly facilitates the assignment of the spectra. Along this line, band A represents rotational excitation between levels with |P|=0.5, while band B involves transitions between levels with |P|=0.5 and |P|=1.5. The observed fine structure in these bands is due to end-over-end rotation of the complex and splittings of the energy levels induced by the interaction with the Ne atom.

In order to allow for a compact representation of the different energy levels, we employ a model Hamiltonian defined through spectroscopic constants.[9, 12] In a zeroth order approximation, we can view the complex as a rigid symmetric top with electronic structure causing the rotational levels to be fourfold degenerate. The degeneracy is lifted partially through electrostatic interaction causing the energy levels to split into two ω-components ($\omega = \pm 0.5$) labeled in the following by '+' and '-' sub- or superscripts.[51] Ultimately, the remaining degeneracy is lifted through P-type doubling yielding levels distinguished by a symmetry label ϵ.[52]

We use the following expression appropriate for a T-shaped complex involving an open shell diatom and a rare gas atom:

$$E_{vJP\omega\epsilon} = E_{vP\omega} + B_\omega J(J+1) + V_\omega(J+\tfrac{1}{2}) + \epsilon \sum_{n=0}^{2} \tfrac{1}{2} D_{2n}^{\omega} (J+\tfrac{1}{2})^n \tag{3.1}$$

For the comparison and discussion of different sets of spectroscopic constants, we find it more convenient to convert this set of constants to one appropriate for a linear complex whose energy levels are described by the expression [12]:

$$\begin{aligned} E_{vJP\omega\epsilon} = E_{vP} + B_{vP0}J(J+1) + B_{vP1}(J+\tfrac{1}{2}) \\ + \sum_{n=0}^{2}(\epsilon F_{2n} + \tfrac{\omega}{|\omega|}V_{2n} + \epsilon\tfrac{\omega}{|\omega|}C_{2n})(J+\tfrac{1}{2})^n \end{aligned} \tag{3.2}$$

Spectroscopic constants are fitted for the bound states of the PESs for NO($\tilde{X}$, r=r$_e$)-Ne, NO($\tilde{X}$, v=0)-Ne, and NO($\tilde{X}$, v=2)-Ne. Energy levels with |P|=0.5, and 1.5 are reproduced in the fit within 0.001 cm^{-1}. Larger deviations up to 0.1 cm^{-1} are found for levels with |P|=2.5 which are close to the dissociation limit. As an example, we show in Figure 3.1, the fit results for the J-dependence of the two parity levels with ω=+0.5 and |P|=0.5 for the vibrational overtone level.

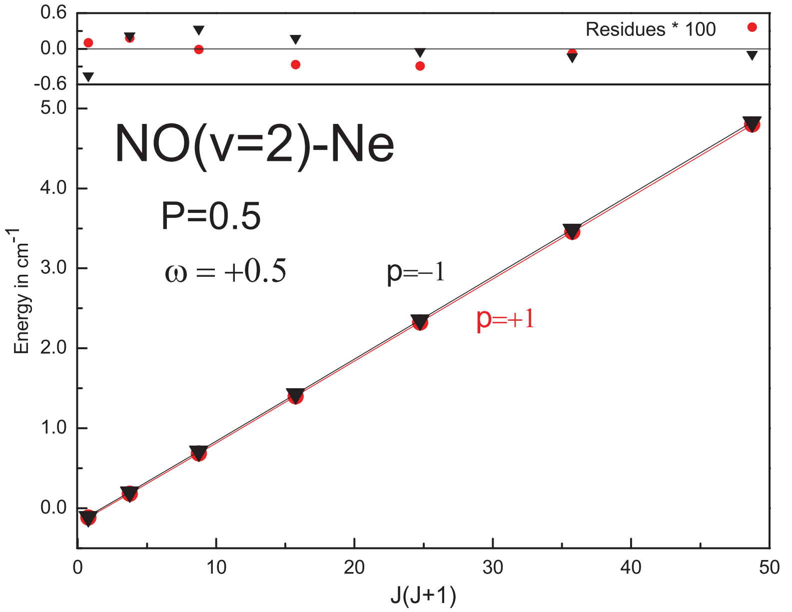

Figure 3.1 Energy levels in cm^{-1} with ω=+0.5 and |P|=0.5 for the NO($\tilde{X}$, v=2)-Ne PESs as a function of J(J+1) (red circles = positive parity p=+1, black triangles = negative parity p=-1): Comparison of CC levels with least squares fit result of spectroscopic constants. The inset in the top of the Figure shows the residues multiplied by 100.

A compilation of the derived spectroscopic constants is listed in Tables 3.1 and 3.2. There are only small differences in the constants determined for the three different PESs. Especially small are the differences between the results for the NO($\tilde{X}$, r=r$_e$)-Ne surface and the one averaged for the vibrational NO ground state. The main difference is a small reduction in the rotational constant B_0 for the vibrationally averaged surface indicating a slight increase in the intermolecular distance. The changes are more pronounced for the v=2 surface. In this case, a significant reduction is also found for the electrostatic splitting constant V_{20}. An important difference is found in the relative position of the levels with $|P| = 1.5$ with respect to the ones for $|P| = 0.5$. Here, the PESs for NO($\tilde{X}$, v=2)-Ne yield energy levels which are shifted down by almost 0.1 cm^{-1} in better agreement with the experimental spectra. Changes in the other constants are not significant, especially when considering the spectral resolution of the experiment.

For comparison, we have included into the tables also the results for the fit of the bound states of the older *ab initio* PESs from Alexander et al. (Ref. [34]) and for the spectroscopic fits of the original experimental IR spectra (Ref. [2]). The older *ab initio* PESs yield constants which are noticeably different from the ones found for the newer PESs. The rotational constants are predicted to be too low while the electrostatic splitting constants come out too large. As expected, there is very little change in the fit of the original and the new experimental spectra. Interestingly, the results for the new PESs approach the experimentally fitted constants and thus confirm the better quality of the new set of surfaces.

3.3.2 Analysis of the near IR spectra

Near-IR spectra of the NO-Ne complex have been recorded in the region of the first overtone vibration of the NO monomer. In the present experiment, the IR absorption is detected by exciting the complex into the $\tilde{A}$-state dissociation continuum. As shown by Ayles et al. in Ref. [31], the electronic $\tilde{A}$-state of the complex is shifted to larger intermolecular

Table 3.1 Fitted spectroscopic constants in cm^{-1} (defined in Eq. 9) describing the energies of the lowest bound states with |P|=0.5.

PES	E_{vP}	B_1	B_0	V_{20}	V_{21}	V_{22}	C_{20}	C_{21}	F_{20}	F_{21}
r=r_e	0.310	0.0073	0.1085	0.3668	0.021	0.0036	0.0072	0.0036	0.0003	0.0019
v=0	0.310	0.0073	0.1083	0.3662	0.021	0.0036	0.0070	0.0036	0.0000	0.0020
v=2	0.300	0.0075	0.1079	0.3554	0.022	0.0036	0.0074	0.0036	0.0001	0.0021
PES Ref. [34]	0.000	0.0000	0.1070	0.4220	0.000	0.0070	0.0070^a	0.0036^a	0.0003	0.0019
Fit Ref. [2]	0.000	0.0000	0.1130	0.3300	0.000	0.0068	0.0040	0.0060	0.0000	0.0008
Fit this work	0.271	0.0025	0.1108	0.3278	0.011	0.0048	0.0095	0.0043	0.0000	0.0008

a. Average value of constants fitted separately for $\omega = \pm 0.5$.

Table 3.2 Fitted spectroscopic constants in cm^{-1} (defined in Eq. 9) describing the energies of the lowest bound states with |P|=1.5.

PES	E_{vP}	B_1	B_0	V_{20}	V_{21}	V_{22}	C_{20}	C_{21}	F_{20}	F_{21}
r=r_e	4.267	0.0149	0.1056	0.4947	0.0027	0.0008	0.0042	0.0016	0.0017	0.0006
v=0	4.272	0.0153	0.1052	0.4847	0.0024	0.0009	0.0046	0.0018	0.0015	0.0006
v=2	4.174	0.0158	0.1047	0.4650	0.0018	0.0011	0.0051	0.0020	0.0018	0.0007
PES Ref. [34]	4.051	0.0000	0.1045	0.5040	0.0000	0.0008	0.0027^a	0.0002^a	0.0017	0.0006
Fit Ref. [2]	3.830	0.0000	0.1100	0.4500	0.0000	0.0010	0.0000	0.0000	0.0000	0.0000
Fit this work	4.089	0.0063	0.1075	0.4385	0.0018	0.0018	0.0000	0.0000	0.0000	0.0000

a. Average value of constants fitted separately for $\omega = \pm 0.5$.

distances in comparison to the electronic ground state. As a consequence, the complex reaches only states in the electronic transition with good Franck-Condon factors which are localized near the repulsive wall of the $\tilde{A}$-state surface. Subsequently, it will dissociate producing an electronically excited NO fragment which is efficiently ionized in the UV laser pulse. In our experiments, we fix the UV laser to frequencies near 40815 cm^{-1}. For a typical IR photon energy of 3724 cm^{-1}, the complex is excited to states lying 44539 cm^{-1} above the vibronic ground state. Using the dissociation energy of 44228 cm^{-1} reported by the Lawrance group (Ref. [29]), we find that the complex is excited to states about 311 cm^{-1} above the $\tilde{A}$-state dissociation limit. Because at this energy rotational states up to n $\approx$ 10 (n representing the quantum number for the diatomic angular momentum excluding spin) can be populated, we expect a relatively uniform detection of different levels of the NO($\tilde{X}$, v=2)-Ne complex.

In Figures 3.2 and 3.3, we present the comparison of dissociation detected spectra for the region of bands A and B with spectra based on the fitted spectroscopic constants listed in Tables 3.1 and 3.2. In the figures, we also include as trace (a) the original experimental spectrum recorded through 2+1 REMPI detection via a Rydberg state of NO-Ne correlating with the H-state of NO.[2] To facilitate the assignment of rotational lines, we include several rotational frequency combs for different R-, Q-, and P-branches. The sub- and superscripts indicate the involved ω-labels for the initial and final levels, respectively. As a guide, several line positions are labeled with the initial total angular momentum quantum number reduced by 0.5, i.e. by J-0.5.

Clearly, the dissociation detected spectrum (trace (b) in Figure 3.2), shows better signal-to-noise ratio as well as better spectral resolution. Most noticeable is the splitting of the Q-branch in Band A which is well resolved in the new spectrum in contrast to the earlier work. Furthermore, several clumps of lines are not correctly recorded in the earlier double resonance experiment. For example, to the red and blue side of the split Q-branch, there are a number of lines with similar intensity which are not recorded as such in the 2+1 REMPI spectrum. On the red side, a doublet is almost missing while on the blue side one doublet appears as a line with an intensity similar to the Q-branch components.

For band B (see Figure 3.3), we can identify now several rotational branches in contrast to our earlier spectra. Especially the Q^+_--branch near 3727 cm^{-1} to the red of the band center is now clearly recognizable. But also for the R-branches on the blue side the branch pattern is now more pronounced. These differences must be taken as evidence that dissociation detection provides a much more uniform detection method. This improved uniformity in detection results in a much more realistic recording of intensities and therefore rotational branches can be more easily identified as such. This allowed us to perform a more rigorous spectroscopic fit of the spectrum as is evidenced by the excellent reproduction of the experimental spectrum.

The spectroscopic fit was done similarly to our earlier work on NO-Ar and NO-Xe.[12, 11, 53] It is important to stress that we used as the initial input for the fit, the spectroscopic constants determined from the results of the theoretical calculations as described in Section IV.A. Because of the complexity of the spectra, we only used one set of spectroscopic constants for both the initial and final NO vibrational levels. Thus, we did not distinguish between constants for the two different vibrationally averaged PESs. As discussed below in the context of the comparison of the results for theoretical calculations based on two different vibrational averages, there is some evidence that also the experimental spectra indicate some of those differences.

The origin is found to be at 3724.02 cm^{-1}, i.e. shifted with respect to the corresponding monomer transition by 0.17 cm^{-1} to the blue. The small shift can be taken as additional evidence of the small difference between the bound states of the NO($\tilde{X}$, v=0)-Ne and NO($\tilde{X}$, v=2)-Ne PESs. The fitted spectrum is calculated for a temperature of 1.9 K which is consistent with the rotational temperature observed for the NO monomer under these expansion conditions. The theoretical stick spectrum is convoluted with a Voigt profile with a width of about 0.03 cm^{-1} which is slightly less than the observed width of individual lines in the experimental spectrum. As a result, rotational structures are more easily identified with the help of the theoretical spectrum. In any case, the fitted spectrum reproduces almost all structures in the experimental spectrum extremely well. Even the calculated intensity patterns of different branches agree well with the experimentally observed ones. Nevertheless, the spectroscopic fit in our original work did yield constants that are in good agreement with the ones found in the fit of the new spectra.

Using the spectroscopic constants given in Tables 3.1 and 3.2, we generate theoretical spectra that are compared with the experimental spectra in Figures 3.4 and 3.5. Here, trace (a) shows the spectrum generated from the bound states calculated for the NO($\tilde{X}$, r=r_e)-Ne PESs while trace (b) is generated using as initial and final states the bound states of the PESs for NO($\tilde{X}$, v=0)-Ne and NO($\tilde{X}$, v=2)-Ne, respectively. The fit of the experimental spectrum is shown as trace (c) while the experimental spectrum is given as trace (d). The overall appearance of the theoretical spectra agrees very well with the experiment for both bands. The displacement of the different rotational branches caused by the electrostatic splitting is correctly predicted by the calculation. In band A, the R- and P- branches are displaced away from the central Q-branch indicating that the electrostatic splitting in the theoretical treatment is slightly overestimated. In contrast, the splitting of the Q-branch is predicted slightly too small. For band B, we notice that the overall position of the band is shifted to the blue in comparison to the experimental spectrum. A careful inspection of the R-branches in this band reveals that the predicted rotational constant is slightly too small.

Interesting is also the comparison of spectra for different NO-Ne PESs. Clearly, there is a significant improvement when the appropriate vibrationally averaged PESs are used for the generation of the spectra. Most noticeable is the overall shift of band B to slightly smaller frequencies. As can be seen most clearly for band A, the different rotational branches are also shifted in a direction closer to the experimental data. Because there is very little difference in the spectroscopic constants for the NO($\tilde{X}$, r = r_e)-Ne and the NO($\tilde{X}$, v = 0)-Ne surfaces, the changes must be attributed mainly to the change in the constants of the vibrationally excited PESs. This manifests itself also in the contours for the two components of the Q-branch in band A. While for the spectra for NO($\tilde{X}$, r = r_e)-Ne, as well as for the fitted spectrum, the same spectroscopic constants are used for the initial and final energy NO vibrational levels, both Q-branch components have similar symmetric contours. This contrasts the situation, where the two sets of constants appropriate for the vibrationally averaged PESs are used. In this case, we find the red component to be shaded more strongly to the red as compared with the shading towards the blue of the blue component. Although not as pronounced, a similar change in the contour is also observed in the experimental spectrum indicating a small dependence of the spectroscopic constants on the NO vibrational state.

3.3.3 IONIZATION DEPENDENCE

In order to explore the $\tilde{A}$-state dissociation characteristics of the NO-Ne complex, we scanned the UV wavelength through the hot-band region of the NO A-X system with the IR frequency fixed to a known resonance of the NO-Ne complex. During these scans, we monitored simultaneously ion signals for the arrival times of NO^+ and NO^+-Ne at the detector. Examples of the ion signals recorded in the NO^+-channel using about 300 uJ/plse are shown in Figure 3.6. The measured ionization curves are displayed as a function of the combined UV and IR photon wavenumbers. In this way, the curves reflect directly the dissociation threshold for NO($\tilde{A}$)-Ne if we assume that, upon reaching the threshold, an excited NO fragment is formed and subsequently ionized. While signals could be observed for the NO^+ channel, we did not find any clear signal in the parent ion channel consistent with the findings reported by Wright et al.[31]

Unfortunately, we could not fix the IR frequency to one of the two NO-Ne Q-branch components that dominate the spectrum. In comparison to NO-Ar the near-IR spectrum of NO-Ne exhibits an extremely small blue shift (+0.17 cm^{-1}) with respect to the origin of the first overtone spectrum of the NO monomer. As a result, the NO-Ne Q-branch structures (3723.982 cm^{-1} and 3724.054 cm^{-1}) are so close to the Q11(0.5) lambda doublets of the NO-monomer at 3724.067 cm^{-1} and 3724.079 cm^{-1} that prohibitively large NO monomer background signals result when the IR is fixed to one of the components. We therefore choose lines at 3724.695 cm^{-1} (traces (a) and (b) in Figure 3.6), 3724.749 cm^{-1} (trace(c)), and 3728.300 cm^{-1} (trace(d)). The lines are marked with an asterisk in Figures 3.2 or 3.3. The first line corresponds to the first member of the Q_{+}^{-}-branch in band A, i.e. it involves both parity levels with J = 0.5 and P = 0.5. The second line is a superposition of the second member of the Q_{+}^{-}-branch and the third member of the R_{+}^{+}-branch of band A. Therefore levels with J values 1.5 and 2.5 are prepared. The third line represents the superposition of the first and second members of the R_{-}^{-}-branch and the R_{+}^{+}-branches in band B, respectively. For this line, levels with P = 1.5 and J up to 2.5 are prepared in the IR excitation step. In the bottom of the figure, we also show as trace (e) the corresponding curve for the NO-Ar complex. As will be discussed below, the curve for NO-Ar is actually shifted by 60 cm^{-1} to lower wavenumbers.

In order to check for a possible loss of signal due to vibrational predissociation, we reduced the relative time delay between the two laser pulses. As an example, traces (a) and (b) were recorded with overlapping laser pulses. But also under these conditions, no signal in the parent ion channel could be detected. On the other hand, when the two pulses overlap in time, we observe strong two-photon resonances of the NO monomer confirming the correct spatial alignment of the lasers. A two-photon spectrum of NO calculated for 9K, is shown together with trace (b). If the laser pulses do not overlap, we still find extremely weak double resonance signals due to the NO monomer. In this case, the signals are due to off-resonant pumping of NO rotational levels either with j=0.5 (trace (c)) or j=1.5 (trace (d)). Calculated one-photon spectra probing these levels are displayed together with traces (c) and (d). Several of these UV resonances were used for UV wavelength calibration.[50]

As a note of caution, we point out that the observed measurements suffer from a relatively poor signal-to-noise ratio. All used IR lines are quite narrow and weak. Thus, small drifts or fluctuations in the IR laser frequency increase the noise making the identification of signal or structures more difficult. The reproducibility of the general trends are demonstrated through the curves shown as traces (a) and (b) which were recorded under identical experimental conditions. The curves clearly demonstrate the strong signal rise with increasing UV frequency independent of the relative laser delay or the chosen fixed IR frequency. All curves indicate an upper limit of the detection threshold for NO^+ near 44250 cm^{-1}. Interestingly, we also observe a broad peak around 44285 cm^{-1}. Structures like these have been also observed in the case of NO-Ar (compare trace (e) in Figure 3.6). In the case of NO-Ar, the observed structures correlate with the thresholds for the production of NO(A) fragments in different rotational states n.[11] The first broad maximum indicates states with n = 0-2, while the second maximum allows for the production of states with n up to 4. If we assume similar effects in the dissociation of NO-Ne, we can shift the NO-Ar curve in such a way that it is aligned with the observed maximum. Obviously, it is not clear which of the observed NO-Ar maxima corresponds to the one found for the NO-Ne complex. If we align the second maximum of the NO-Ar curve, we find a threshold of 44233.5 ± 5.0 cm^{-1}. This value can be compared with the dissociation threshold of 44228.4 ± 2.5 cm^{-1} reported by the Lawrance group.[29] Obviously, our result does not represent a completely independent measurement of the dissociation limit, but it is perfectly consistent with the result of the ion imaging experiments of Holmes-Ross and Lawrance.

3.4 Conclusions

In this article, we describe the measurement of the first two bands in the near-IR spectrum of NO-Ne through NO $\tilde{A}$-state dissociation detection. The enhanced Franck-Condon factors for excitation into the $\tilde{A}$-state continuum provide significantly increased detection efficiency which enables us to record spectra with improved spectral resolution. At energies high above the dissociation limit, a large number of fragment channels is open causing the method to provide a more uniform detection than other double resonance schemes. The resulting spectra allow an easier identification of groups of lines or rotational branches and therefore enable or facilitate a spectroscopic fit. Finally, the near IR spectra for NO-Ne demonstrate that $\tilde{A}$-state dissociation detection is feasible also for NO-X complexes which do not show a structured A-X spectrum. On the downside, the relatively strong spectra found for NO-Ne will likely limit the use of Ne as a seed gas in the investigation of other NO-X systems. This leaves an expansion in He as the only viable option which is now exclusively implemented in our laboratory.

Using a model Hamiltonian, the fit of the experimental spectra results in calculated spectra that reproduce even small features in the experiment very well. The measured spectra are compared with results of bound state calculations based on a new set of high level *ab initio* PESs. The overall agreement between the experimental and the theoretical spectra is significantly improved over the results based on the earlier *ab initio* PESs of Alexander et al. For the first time, we compare also spectra generated from PESs averaged over the NO intermolecular distances in different ways. Using the PESs correctly averaged over the NO vibrational wavefunctions appropriate for the overtone transition results in better agreement than using PESs for the NO distance fixed at its minimum value.

From structures in the ionization curves for the NO-Ne complex prepared in different levels associated with the first vibrational overtone of NO, we find a dissociation limit of

44233.5±5.0 cm^{-1} in agreement with results reported by the Lawrance group.

3.5 Acknowledgements

The authors would like to thank Millard Alexander for his encouragement and many discussions. J. K. is grateful to the US National Science Foundation for financial support under Grant No. CHE-1213332 to Millard Alexander. S. Z. and H. M. gratefully acknowledge the financial support provided by the National Science Foundation under grant No. CHE-0957260.

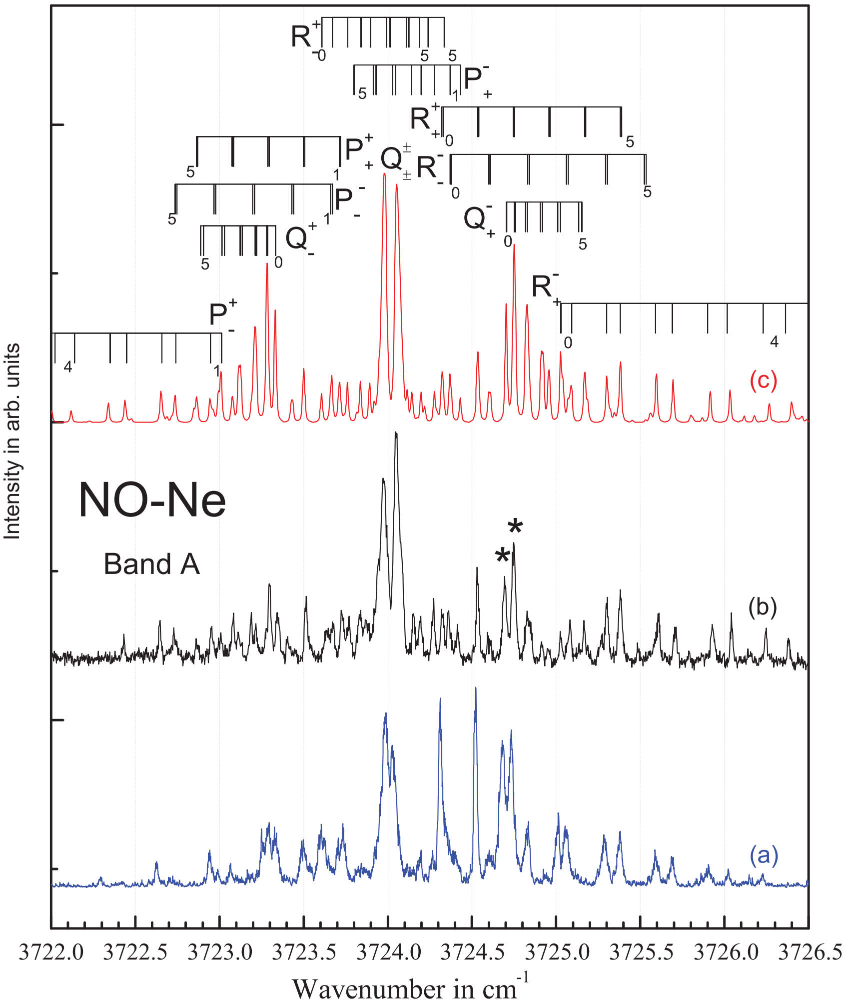

Figure 3.2 Comparison of experimental spectra of band A (trace (a): Fixed UV 2+1 REMPI of NO-Ne via the $\tilde{H}$-state, see Ref. [2], trace (b): dissociation detection, this work) with fitted spectrum (trace(c)). Ladders for several rotational branches are included (see text for detail). Lines marked with an asterisk represent the IR frequencies used in the UV-scans recording the ionization curves of NO-Ne.

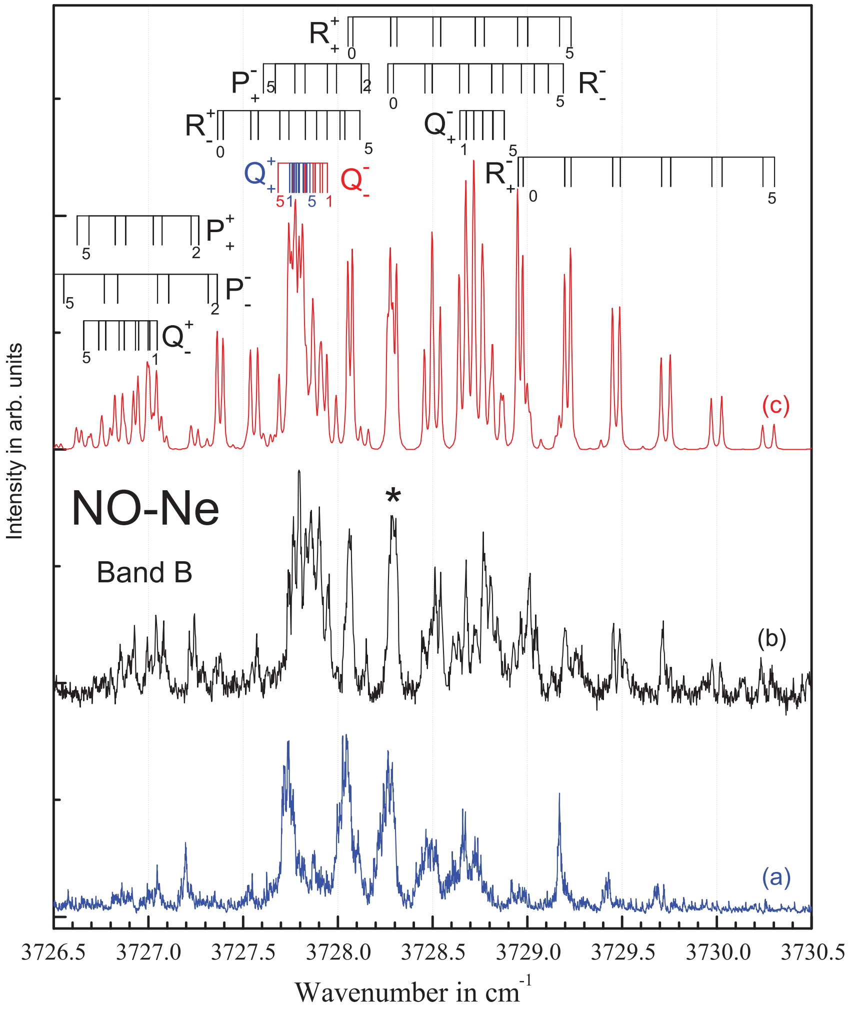

Figure 3.3 Comparison of experimental spectra of band B (trace (a): Fixed UV 2+1 REMPI of NO-Ne via the $\tilde{H}$-state, see Ref. [2], trace (b): dissociation detection, this work) with fitted spectrum (trace(c)). Ladders for several rotational branches are included (see text for detail). The line marked with an asterisk represents the IR frequency used in a UV-scan of the ionization curves of NO-Ne. See text for details.

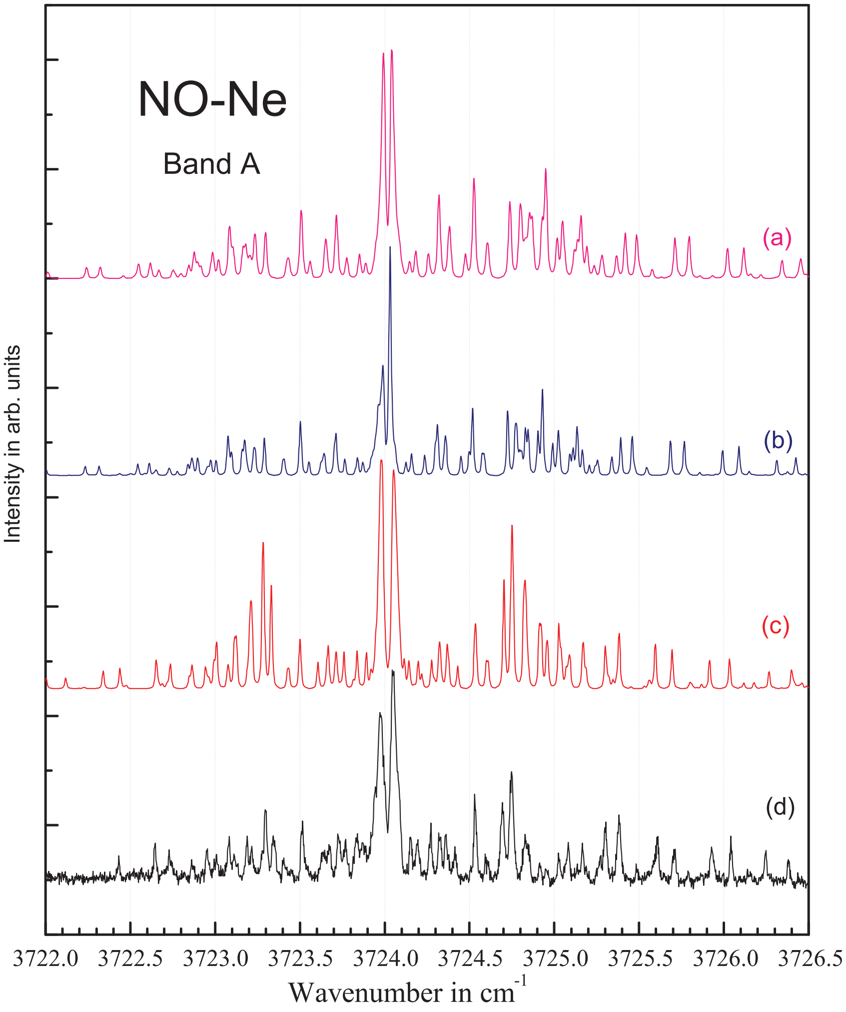

Figure 3.4 Comparison of calculated spectra (trace (a): NO($\tilde{X}$, r=r$_e$)-Ne, trace(b): NO($\tilde{X}$, v=0,2)-Ne, trace(c): spectroscopic fit) with experimental spectrum trace(d): Band A.

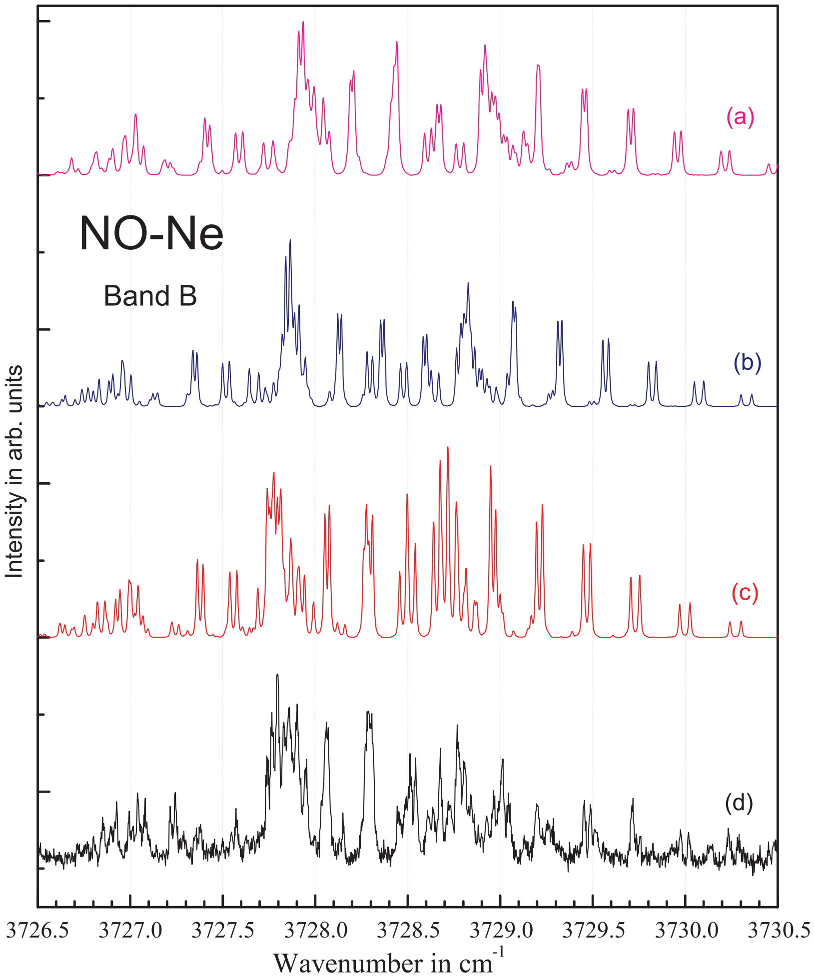

Figure 3.5 Comparison of calculated spectra (trace (a): NO($\tilde{X}$, r=r$_e$)-Ne, trace(b): NO($\tilde{X}$, v=0,2)-Ne, trace(c): spectroscopic fit) with experimental spectrum trace(d): Band B.

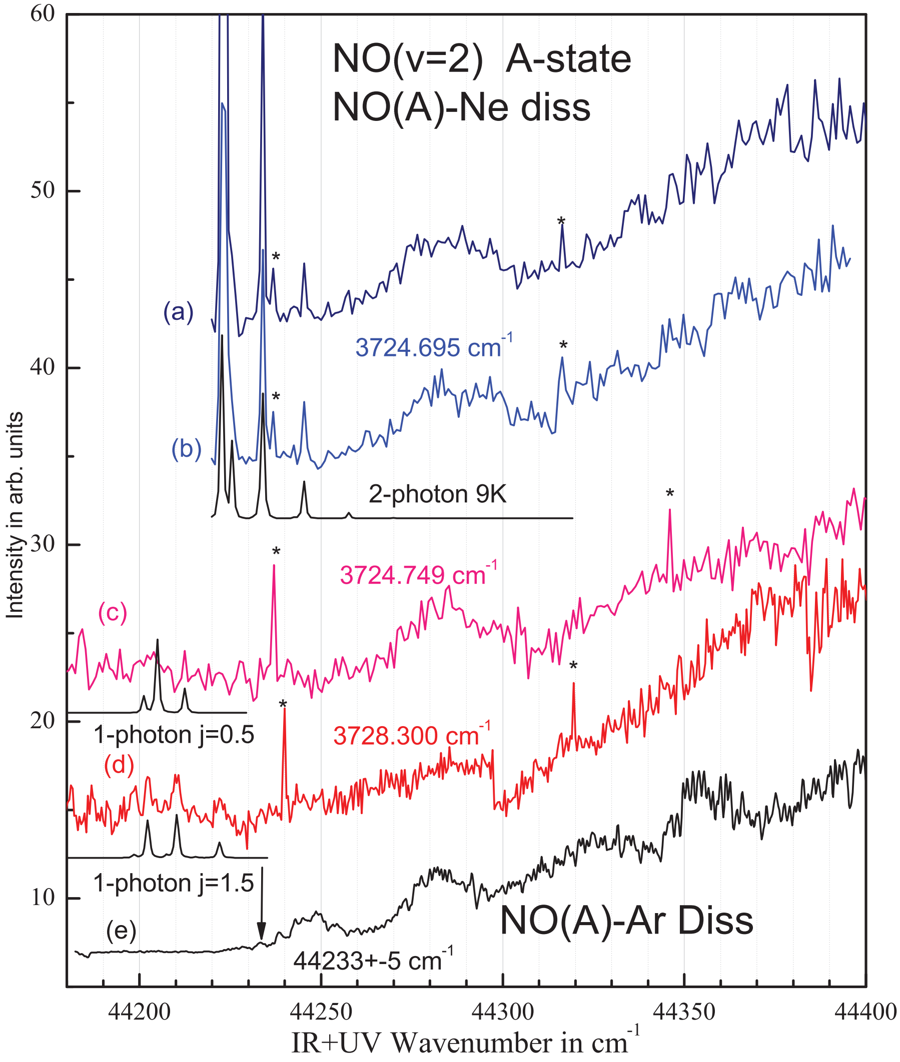

Figure 3.6 Comparison of the NO-Ar ionization curve (trace(e)) shifted to the red by 60 cm^{-1} with different NO-Ne ionization curves with the IR fixed at 3724.695 cm^{-1} (traces (a) and (b)), 3724.695 cm^{-1} (trace(c)), and 3728.300 cm^{-1} (trace (d)). See text for details. Lines marked with an asterisk are unidentified NO background lines not induced by the IR laser.

Chapter 4

The near-IR spectrum of NO($\tilde{X}$ $^2\Pi$)-He detected through excitation into the $\tilde{A}$-state continuum: A joint experimental and theoretical study[1]

---

[1] V. Beutner, S. G. Zhang, H. Meyer, and J. Kłos. J. Chem. Phys. **145**, 124318 (2016). Reprinted here with permission of the publisher.

Abstract

We present the first measurement of a bound-state spectrum of the NO-He complex. The recorded spectrum is associated with the first overtone transition of the NO moiety. The IR absorption is detected by exciting the vibrationally excited complex to the $\tilde{A}$-state dissociation continuum. The resulting NO(A) fragment is subsequently ionized in the same laser pulse. We recorded two bands centered around the NO monomer rotational lines, $Q_{11}(0.5)$ and $R_{11}(0.5)$, consistent with an almost free rotation of the NO fragment within the complex. The origin of the spectrum is found at 3724.06 $cm^{-1}1$ blue shifted by 0.21 $cm^{-1}1$ from the corresponding NO monomer origin. The rotational structures of the spectrum are found to be in very good agreement with calculated spectra based on bound states derived from a set of high level *ab initio* potential energy surfaces ((Kłos et al. *J. Chem. Phys.* **2000**, 112, 2195)).

4.1 Introduction

Complexes of NO with different rare gas atoms have served as prototypes for the investigation of the interaction of an open-shell diatom with a closed shell rare gas atom.[54, 9] Especially, the interaction of NO with Ar has been studied extensively in different scattering experiments [55, 56], and spectroscopically in different regions of the electro-magnetic spectrum.[9, 57, 11] Also interactions with Ne [40, 38, 35, 58], Kr [59, 60] and Xe [61, 53] have been studied in collision experiments or through spectroscopy of the corresponding van der Waals complexes.

Up to date, there are no reports on the spectroscopic detection of the NO-He complex. Information about the interaction for this system relied almost exclusively on different collision experiments. Most recently, the group of Meerakker employed Stark deceleration of the NO beam to prepare NO in a single quantum state. Using a counter-propagating molecular beam arrangement, they were able for the first time to resolve the diffraction oscillations in individual completely state-resolved inelastic differential scattering cross sections for different NO - rare gas systems.[62] The measured scattering data were compared to calculated cross sections using the most reliable potential energy surfaces (PES) to date and were found to be in excellent agreement with quantum mechanical scattering calculations. For the interaction with neon and argon, these ab-initio potential surfaces were shown to predict also the bound spectra for the associated van der Waals complexes very well.[57, 12, 37, 58]

The first signal attributed to NO-He was found in VMI experiments related to studying the photodissociation of NO-Ar complexes.[63] Similar experiments were subsequently performed by the Lawrance group on NO - rare gas complexes.[64, 29, 3] For the NO-Ar complex, they also demonstrated that even very small populations in excited rotational levels can result in a significant apparent reduction of the extracted binding energy due to a large variation in Franck-Condon factors for the $\tilde{A}$ - $\tilde{X}$ system.[64]. In these studies, the electronic ground state binding energies of the complexes of NO with He, Ne and Ar were determined as 3.0 ± 1.8, 28.6 ± 1.7, and 93.5 ± 0.9 $cm^{-1}1$, respectively.

Foundations of the theoretical framework for dealing with the open shell diatom - closed shell atom systems were laid by Nielson et al. and Alexander.[65, 66] Alexander and Corey used the potentials from Nielson et al. to develop and employ different approximations for the quantum mechanical calculation of inelastic cross sections for the scattering of NO from He and Ar.[67] Later, Yang and Alexander determined an improved set of PESs for NO-He based on the coupled electron pair approximation (CEPA) and used it to calculate quantum mechanical cross sections with a full close coupling method.[68] These calculations were in excellent agreement with the measured integral (Ref. [6]) and differential (Ref. [69]) cross sections. Improved ab-initio PESs using the coupled cluster method were subsequently determined by Lee and Wright.[70] This set of PESs is similar to the one determined previously by Yang and Alexander. Larger differences were found with the PESs of Zolotoukhina and Kotake who employed an MP4/MP2 study.[71] Up to date, the most reliable PESs are the ones from Kłos et al. who employed the RCCSD(T)-method.[72] The global minima of the two surfaces are D_e= 29 and 25 $cm^{-1}1$ while the binding energy of the lowest level is found to be D_0 = 7 $cm^{-1}1$. The considerable difference between the two D-values reflects the large zero point vibrational energy for this system. Spectra generated from the bound states determined for these PESs will be compared with our experimental near-IR spectrum of the NO-He complex. The D_e values are similar to values D_e = 17-20$cm^{-1}1$ determined by Keil et al. analyzing total differential scattering cross section for NO + He assuming different potential forms.[73] As mentioned earlier, Holmes-Ross et al. determined a smaller binding energy for this system.[29] Very likely the derived value reflects contributions from excited states populated in their molecular beam similar to the findings in our experiments.

Other interesting aspects of the NO-He interaction, mainly in electronically excited states, have been targeted in experiments embedding NO into superfluid He-droplets.[74] Polyakova et al. studied the two-photon excitation of the embedded NO to the analog of the electronic A-state of the monomer and its subsequent ionization yielding different ionic clusters fragments. The changes in the electronic state characteristics cause complicated relaxation processes in combination with transport within the droplet.

Recently, we employed a new variant of IR-UV double resonance spectroscopy of NO containing van der Waals complexes. In this method, the IR absorption of the complex is detected by exciting the vibrationally excited complex to the dissociation continuum associated with the ground vibrational level of its electronic $\tilde{A}$-state. Following rapid dissociation, the NO(A) fragment is efficiently ionized within the same UV laser pulse. We successfully employed this technique to remeasure the IR spectra of NO-Ar and NO-Ne in the region of the first vibrational overtone of the NO monomer.[11, 58] In our earlier work on NO-Ne, we had employed excitation to bound levels of higher Rydberg states in a two-photon resonance enhanced multiphoton ionization (REMPI) process.[2] Although for this system, no structured $\tilde{A}$-$\tilde{X}$ spectrum has been found experimentally, we find excitation to the $\tilde{A}$-state continuum to be very efficient. This allowed us to remeasure the IR spectrum of this complex with increased sensitivity and spectral resolution.[58] On the down side, these results demonstrate clearly that neon or argon cannot be used as a seed gas when trying to extend this method to the study of other NO-X complexes, for example, complexes of NO with different closed shell molecules. As an alternative, we investigated the use of helium as a seed gas. It was during the course of this work that we detected the first bound NO-He spectrum when we measured reference IR spectra using similar NO/He gas mixtures, but without the partner molecule X.

The paper is organized as follows. A brief description of the experimental set-up and procedure is given in Section 4.2. In section 4.3, we discuss briefly the optimization of a helium seeded pulsed molecular beam, and present the results for the UV wavelength dependence of the detection of vibrationally excited NO-He, and, finally, the spectroscopic analysis of its near-IR spectrum. Conclusions are presented in Section 4.4.

4.2 Experiment

The experiments were performed in a molecular beam scattering apparatus, which has been described in detail previously.[45, 46, 47] Briefly, the apparatus consists of two differentially pumped source and detector chambers. Two different molecular beam sources opposing each other are mounted in the 500 mm diameter source chamber. We use either a home-built piezo-electric valve [ger] or a commercial valve (Jordan Company). Molecular beam pulses travel through skimmers in the walls of the detector chamber. The latter is welded to a flange on top of the source chamber. Side ports on the detector chamber are connected to ports in the source chamber through bellows. One allows for connecting a separate diffusion pump to the detector chamber while the other allows for direct access of the laser beams. The different laser beams intersect the molecular beam pulses in an electrode arrangement, which can accelerate laser generated ions towards a micro-channel plate (MCP) detector via an electrostatic mirror arrangement.

The laser set-up is very similar to the one used in our previous IR studies employing dissociation detection.[11, 58] UV radiation is generated from the output of a dye laser (LAS LDL 20505) operating on the dye Coumarin 460 and pumped by the third harmonic of a Nd:YAG laser (Spectra Physics GCR170-10). We use second harmonic generation in a betabarium borate (BBO) crystal to generate light around 225 nm. Alternatively, hot-band UV around 245 nm is generated through sum frequency generation of the dye output with the residual 532 nm radiation of the Nd:YAG laser in the same BBO crystal. The resulting output allows us to cover the wavelength ranges for the NO A - X fundamental and first overtone bands.[50] Typically, pulse energies of 150-200 μJ are employed in the dissociation detection step for the complex NO-He. The UV beam is focussed with a 500 mm lens onto the molecular beam.

IR radiation near 2.7 μm is generated with a single longitudinal mode OPO laser (Continuum Mirage 3000) pumped with an injection seeded Nd:YAG laser (Continuum Powerlite 8000). In order to increase the output power, the first amplification stage is used in a non-resonant oscillator configuration. This doubles the output power (2-3 mJ) at the expense of an increased linewidth (0.03 cm^{-1}). During a scan, we monitor the fringes of an external etalon (free spectral range = 0.200918 cm^{-1}) and the first overtone absorption spectrum of NO in a photo-acoustic cell. Using the known absorption spectrum of NO, we can establish an absolute frequency scale for each IR scan.[48, 49] The IR beam is also focussed onto the molecular beam with a 500 mm lens.

4.3 Results and Discussion

In order to measure IR spectra of NO-X seeded in He through dissociation detection, it is necessary to minimize contributions to the NO ion signal due to other species like NO-He or larger NO containing clusters. Ideally, a molecular beam seeded with He should be characterized by sufficient adiabatic cooling, so that complexes between NO and the partner of interest, X, are formed at extreme dilution of NO and X. In particular, the cooling itself should not rely on higher concentrations of either of the constituents thus avoiding the likely formation of larger clusters. In comparison to neon or argon, the low mass of helium atoms makes collisional cooling of heavier molecules during the expansion much less efficient. Higher backing pressures can only partially compensate the reduced cross sections because of the limited pumping speed of the vacuum system. As a consequence, higher temperatures are typically observed for helium seeded gas pulses from different molecular beam sources. This makes the production and detection of dimers in a He seeded pulsed molecular beam quite challenging.

We optimized the operating conditions of the molecular beam source for the production of cold molecular beam pulses generated through the expansion of various gas mixtures of He with trace amounts of NO and various molecules like CH_4, N_2 or CO. NO-complexes with the latter molecules can be directly detected through REMPI. It turned out that cold He seeded molecular beam pulses can be achieved using low concentrations in combination with high backing pressures and large nozzle-to-skimmer distances. Especially, the latter parameter proved to be critical. Comparing different molecular beam sources used in our lab, we found the commercial Jordan source to show a superior performance in comparison to our home-built piezo electric source.

In order to identify possible contributions to the NO ion signal during an IR scan employing A-state dissociation detection, we recorded spectra for similar NO/He mixtures but without the partner molecule. It was under these circumstances that we discovered, using the Jordan molecular beam source, the very weak spectrum shown in Fig. 4.1 as trace (c) and assigned to the NO-He complex. Spectrum (d) in the bottom of Fig. 4.1 was recorded when the same gas mixture was expanded from the piezo-electric valve. The signal-to-noise ratio for this spectrum does not allow to discern any lines, which can be unambiguously assigned to NO-He. As mentioned earlier, it is very likely that the achieved beam temperature is not cold enough to allow for a measurable NO-He density. In this figure, we also include a simultaneously recorded photo-acoustic spectrum of NO (trace (a)) together with the calculated room temperature spectrum (trace (b)). Lines in spectrum (a), which are not reproduced in the calculated spectrum are due to water impurities in the cell.

4.3.1 Dependence on UV wavelength

The NO-He spectrum consists of groups of lines centered around the monomer lines $Q_{11}(0.5)$ and $R_{11}(0.5)$ with signals at these latter frequencies dominating the spectrum. Well resolved, relatively strong lines are found to the blue of the $Q_{11}(0.5)$ line while a number of weaker lines are found to the red forming a symmetric pattern. Since the $Q_{11}(0.5)$ line position forms the center of these two groups of lines, the spectrum indicates the absence of a significant red shift. Furthermore, the higher energy part of the spectrum centered around the $R_{11}(0.5)$ line

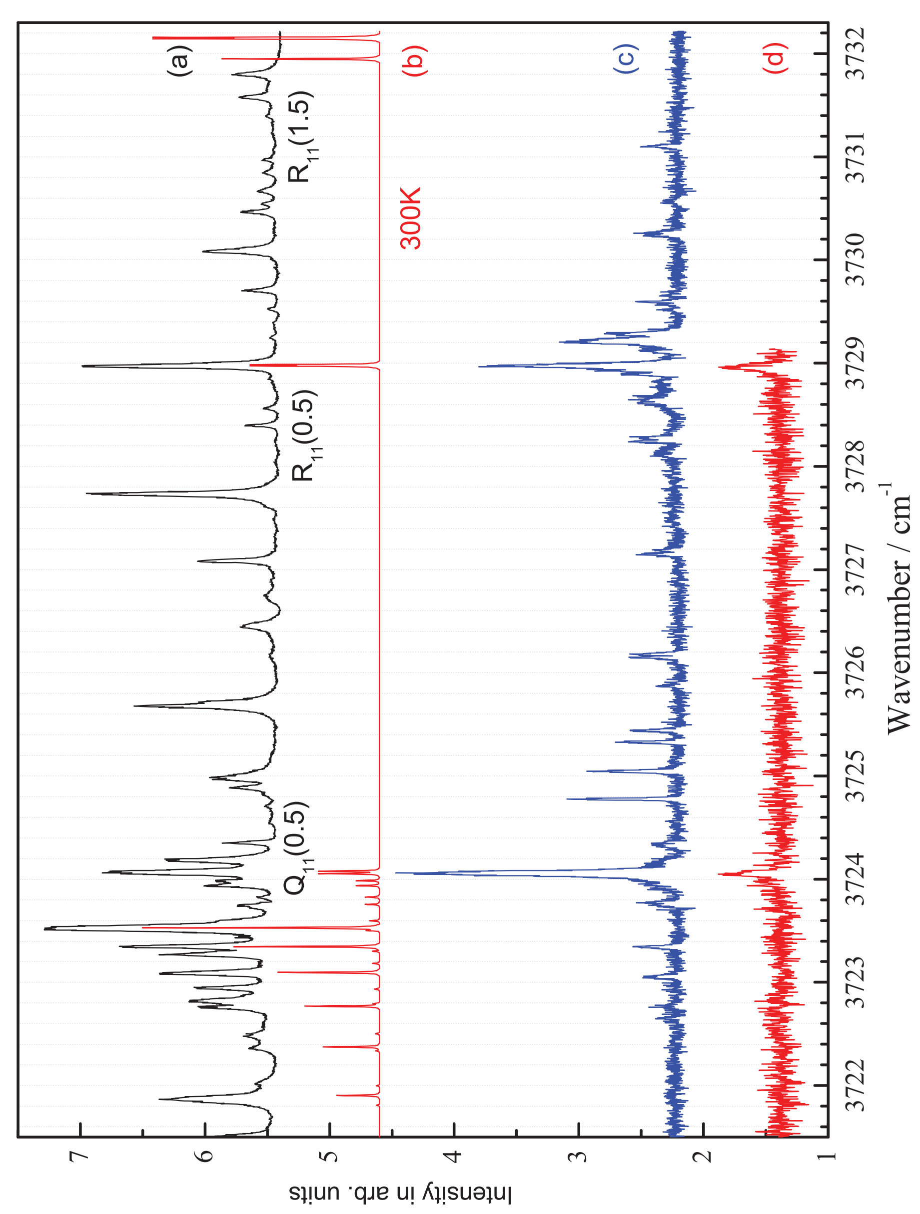

Figure 4.1 Experimental near-IR spectrum (trace (c)) of NO-He recorded at 40737 cm^{-1}1 using a 2% NO in He mixture at 27 psi in the Jordan source. Spectrum (d) was recorded at 40725 cm^{-1}1 expanding the same gas mixture from the piezo-electric molecular beam source. Spectrum (a) represents the simultaneously recorded photo-acoustic cell spectrum of NO. Spectrum (b) is a calculated NO spectrum assuming a temperature of 300 K. Lines in (a), which are not reproduced in (b) are due to water impurities in the cell.

position is a clear indication that the NO monomer is almost freely rotating in the complex.

Since the signal is recorded at the NO monomer ion mass, there is the possibility that the intensity recorded at the frequencies of the lines, $Q_{11}(0.5)$ and $R_{11}(0.5)$, comprises a contribution from the monomer. In order to assess the relative contributions at these frequencies, we scanned the IR frequency through the region of the lines to the blue of the $Q_{11}(0.5)$ line for different UV wavenumbers. The resulting uncalibrated IR spectra are displayed in Fig. 4.2. For each UV wavenumber, two spectra are recorded as scans with increasing (blue) and decreasing (red) frequency. In this way, we find some indication for the reproducibility of these weak signals. Because of the mechanical backlash of the IR laser, spectra with opposing scan directions appear displaced in frequency and therefore are more easily compared.

When comparing the intensities of the signal at the $Q_{11}(0.5)$ line position with the stronger NO-He lines to the blue, we notice that the spectra taken at larger UV wavenumbers are identical within the experimental uncertainty. Especially the ratio of amplitudes of the $Q_{11}(0.5)$ and the NO-He lines does not change. In contrast, we find that, at smaller UV wavenumbers, a monomer contribution causes a significant increase of the signal at the $Q_{11}(0.5)$ position. This increase reflects the approach of the wavenumber range 40475-40487 $cm^{-1}1$ in which the two NO(v=2, j_{NO}=0.5) doublet levels are probed resonantly. As a result, we conclude that the NO monomer causes only minor contributions to the dissociation detected NO-He spectrum for wavenumbers, which exceed the resonances by more than 200 $cm^{-1}1$. This also explains the two very weak lines in spectrum (d) of Fig. 4.1 recorded with a UV wavenumber of 40725 $cm^{-1}1$. The absence of any of the weaker NO-He lines is consistent with the fact that the two observed weak lines are solely due to the NO monomer reflecting the increased temperature for the molecular beam generated with the piezo-electric source.

On the one hand, the NO monomer contributions are minimized when the NO-He spectra are recorded at shorter wavelengths reducing the off-resonance excitation/ionization of NO. On the other hand, calculations of Holmes-Ross et al. indicate a strong wavelength

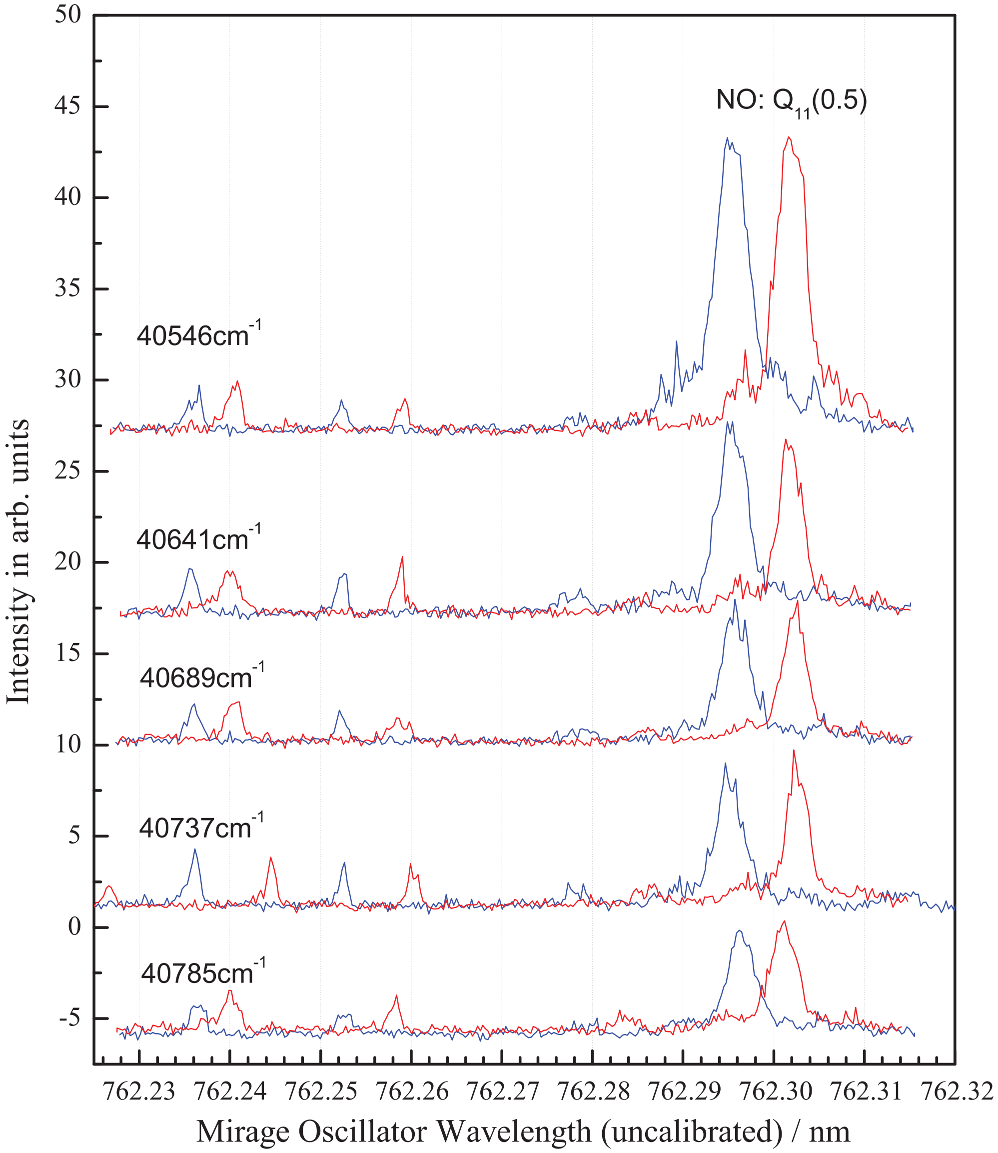

Figure 4.2 Dependence of near-IR spectra of NO-He on the detection UV wavelength. NO - He spectra are displayed as a function of the uncalibrated wavelength of the OPO oscillator. For each indicated UV wavelength, two spectra representing increasing (blue) or decreasing (red) wavenumbers are displayed. The scans cover the region to the blue of the monomer $Q_{11}(0.5)$ line. See text for details.

dependence of the $\tilde{A}$-state photodissociation cross section. In particular, these authors could show that the maximum of the cross section shifts from larger to smaller wavenumbers in going through the sequence NO-Ar, NO-Ne, and NO-He, respectively.[3] They calculated the wavelength dependence of the cross section using the most accurate currently available PESs for these systems.

Their results are reproduced in Fig. 4.3 together with our measurements (red squares) for the vibrationally excited NO-He complex. In these measurements, we fixed the IR laser to 3729.20 $\mathrm{cm}^{-1}1$ (i.e. the first major NO-He line to the blue of the $\mathrm{R}_{11}(0.5)$ line) and recorded the ion signal for different UV wavelengths with extensive averaging in order to reduce the experimental uncertainty to less than 5%. Additional uncertainties are caused by small drifts in the IR laser frequency during the averaging process, which are much more difficult to quantify. We estimate the true uncertainty to be in the order of at least 10-15%. In order to facilitate the comparison with the calculated cross sections in Fig. 4.3, we plot our data as a function of the UV wavenumber shifted up by 3729.20 $\mathrm{cm}^{-1}1$. Furthermore, our data are scaled with one overall factor to best match the magnitude of the calculated cross section. The resulting wavelength dependence is in good qualitative agreement. The position of the maximum around 44360 $\mathrm{cm}^{-1}1$ agrees well with the theoretical data. At smaller wavenumbers near the NO monomer resonances, experimental data are missing due to the large monomer background contributions as explained above. The decay towards larger wavenumbers is much more gradual for the calculated cross section than what is observed for the experimental data. A possible explanation lies in the fact that the experimental data represent the overall dissociation/ionization efficiency of a vibrationally excited complex rather than just the photodissociation cross section for the ground state complex. For completeness, we also indicate with arrows the wavenumbers used in our earlier experiments on NO-Ar and NO-Ne. Here, the optimized UV wavenumbers also coincide well with the calculated maxima of the corresponding photodissocation cross section, thus

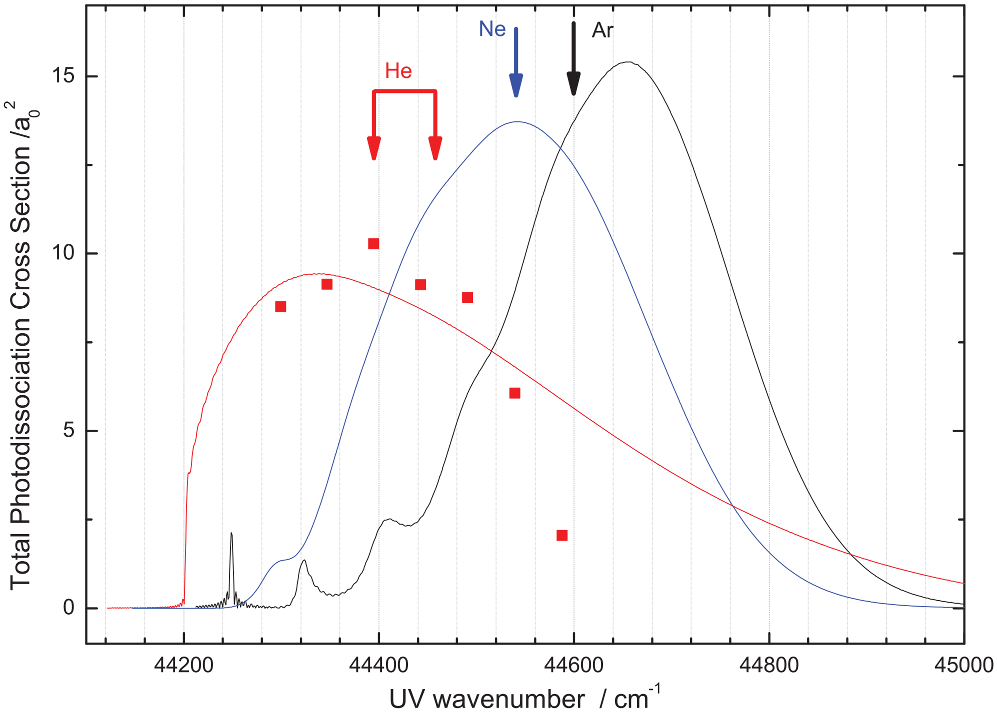

Figure 4.3 Total photodissociation cross sections for excitation into the $\tilde{A}$-state continuum calculated by Holmes-Ross et al. in Ref. [3] for the indicated NO-rare gas complexes: NO-He (red), NO-Ne (blue), and NO-Ar (black) The measured detection efficiency (red squares) for NO-He is plotted as a function of the hot-band UV wavenumber shifted up by 3729.20 $cm^{-1}1$, i.e. the fixed wavenumber of the IR laser used to prepare the vibrationally excited complex. The arrows indicate the maximum efficiency experimentally identified and used in our experiments on the different NO - rare gas systems.

confirming the predicted trend for the different NO-rare gas complexes. These data attest to the great accuracy of the current PESs of the NO-rare gas systems and the subsequent dynamical treatment.

4.3.2 COMPARISON WITH BOUND STATES CALCULATION

The PESs of Kłos et al in ref. [72] were calculated fixing the NO interatomic separation to the monomer r_e value. Here, we report an experimental spectrum build on the 2-0 NO overtone transition. Therefore, the bound states probed are those of PESs associated with the corresponding vibrational states of NO. In our recent work on NO-Ne, we compared spectra based on a single bound-state data set calculated for fixed NO internuclear distance $r=r_e$ with spectra based on bound states calculated for PESs that had been constructed as averages over the NO vibrational states v=0 and v=2.[58] While differences could be noticed, overall the changes were very small. For example, we found a small shift of less than 0.1 $cm^{-1}1$ for the position of the first excited band, band B. Furthermore, the weak interaction causes a very small blue shift of the origin of the experimental spectrum with respect to the origin of the corresponding monomer spectrum. Considering the even smaller polarizability of He compared to Ne, we expect a similar situation for the NO-He system. This reasoning is corroborated by the observed 0.21 $cm^{-1}1$ blue shift of the experimental spectrum with respect to the monomer origin at 3723.8526 $cm^{-1}1$.[48] In this context, it is important to realize that the NO-He band origin coincides perfectly with the position of the monomer $Q_{11}(0.5)$ - line confirming the weakness of the interaction. Therefore, we feel justified in comparing spectra generated from the single bound state data set calculated for the monomer r_e value with the experimental spectra. As discussed in detail below, the excellent agreement between the spectra justifies this approximation. Nevertheless, existing small differences can at least partially be attributed to differences in the effective PESs for the two vibrational states of NO.

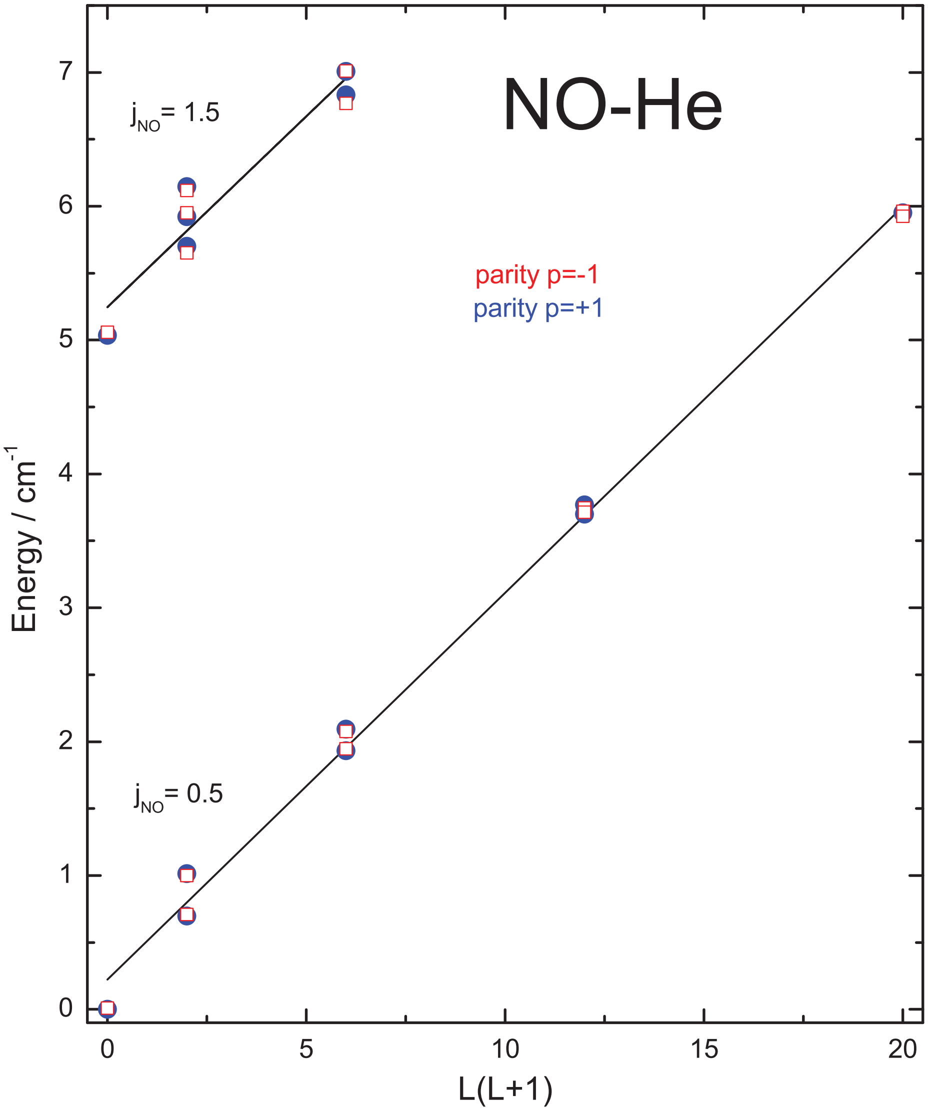

Figure 4.4 Calculated energy levels in cm^{-1} as a function of L(L+1): blue solid circles = positive parity p = +1, red open squares = negative parity p=-1. The solid lines represent the linear least squares fit result assuming a representation in the form of Eq. 4.1. See text for details.

As pointed out by Kłos et al., the energy levels of the complex can be labeled with the approximate quantum numbers L and j_{NO} for the orbital and internal NO angular momenta, respectively.[72] This notion is confirmed when plotting the energies as a function of L(L+1) as shown in Fig. 4.4. We find two sets of data, which show a nearly identical linear dependence on L(L+1). The zero intercepts, 0 cm^{-1}1 and $\approx$ 5 cm^{-1}1, are consistent with the rotational energy of the NO monomer in levels with quantum numbers $\mathrm{j}_{NO} = 0.5$ and $\mathrm{j}_{NO} = 1.5$, respectively. Interpreting the slope as a rotational constant $B = \hbar^2/2\mu R^2$ for the end-over-end rotation of the complex, we find an averaged intermolecular distance R = 4.05 Å, which is slightly larger than the calculated expectation value of 3.94 Å for the ground level. The linear dependence and the intercepts suggest the approximate energy expression:

$$E^{(0)}_{j_{NO},L} = B_{NO} j_{NO}(j_{NO}+1) + BL(L+1) \tag{4.1}$$

Remaining small deviations from this expression reflect the influence of the weak interaction potential. It is responsible for coupling the individual angular momenta leaving the quantum numbers J for the total angular momentum and p for the parity as good quantum numbers. Thus each approximate energy level is split into two parity sets of levels with J-values in the range $|L - j_{NO}| \leq J \leq (L + j_{NO})$. This behavior suggests a space-fixed formulation of the Hamiltonian with a basis set consisting of simultaneous eigenfunctions to the square of the total angular momentum operator, its z-component, and the operators for the squares of the orbital and internal NO angular momenta. Within this formulation, coupling between basis states with a fixed J, but differing in L and j_{NO}, is caused solely by the potential operator while the kinetic energy operator is diagonal.

In the space-fixed representation, transition dipole matrix elements involving two different basis states denoted by quantum numbers (J, M, j_{NO}, $|\omega|$, L, p) and (J′, M′, j'_{NO}, $|\omega'|$, L′, p′) are given by:

$$
\begin{aligned}
\tilde{T} &= \frac{1-pp'}{2}\,\delta_{\omega\omega'}\delta_{LL'}\delta_{MM'}[J][J'][j][j'](-)^{L+M-\omega}\mu_0 \\
&\quad\times \begin{pmatrix} j'_{NO} & 1 & j_{NO} \\ -\omega & 0 & \omega \end{pmatrix} \begin{pmatrix} J' & 1 & J \\ M & 0 & -M \end{pmatrix} \begin{Bmatrix} J' & L & j'_{NO} \\ j_{NO} & 1 & J \end{Bmatrix}
\end{aligned} \tag{4.2}
$$

Here, we have assumed that the transition is mediated exclusively by a parallel transition dipole moment μ_0 of the NO monomer. The quantum numbers j_{NO} and ω refer to the angular momentum of the NO moiety and its projection onto the internuclear axis of NO, respectively. Because the electronic part of a basis state is defined as a symmetrized state in regards to the electronic wavefunction of NO, the state is labeled by the absolute value of ω and its parity p. For the quantum number j_{NO}, we expect transitions with $\Delta j_{NO} = 0, \pm 1$. Because only energy levels with $j_{NO} = 0.5$ are populated in the molecular beam, possible transitions are restricted to $\Delta j_{NO} = 0$, and +1. Since we assume that the transition dipole moment is confined exclusively to the NO monomer, we expect transitions to be built solely on the $Q_{11}(0.5)$ and $R_{11}(0.5)$ monomer lines consistent with the observed experimental spectrum.

As is evident from Eq. 4.2, and, as also shown for closed shell complexes by Hutson in Ref. [**?**], the direct dipole moment contribution to the transition dipole moment operator causes the selection rule $\Delta L = 0$ in addition to the standard dipole selection rules involving J and p. Deviation from this rule will be caused by induced dipole moments, e.g. due to dipole or quadrupole moments. We expect these types of contributions to be very small because of the small polarizibility of the He atom. On the other hand, contributions of basis states with different L to individual eigenstates will also cause a breakdown of the $\Delta L = 0$ selection rule. Indeed, we find for the individual eigenfunctions, in addition to a dominant L basis state, small contributions due to basis states with L+1 or L-1. Typically, the probabilities are in the order of 10-25 % of the one for the dominant L-state. As a result, weak rotational branches with $\Delta L = 0$, and ±1 are observed. Even for the levels characterized by $j_{NO} = 0.5$, a rotational R-branch with $\Delta L = +2$ becomes allowed. The intensity of these branches in the experimental spectra might be further enhanced due to partial saturation of the transitions.

In our calculation of the spectrum, we use an approximate linestrength by allowing relaxed selection rules for ΔL through the introduction of a ΔL dependent weight factor. Furthermore, we replaced the space-fixed projection quantum number M in the second 3j-symbol with the approximate body-fixed one P. The assignment of P to the different eigenfunctions is accomplished by comparing the CC results with the ones from a CS calculation as described in Section II. In this way, it is straight forward to distinguish parallel and perpendicular components of the transition moment.

In Fig. 4.5, we compare the dissociation detected near-IR spectrum of NO-He (trace (c)) with a calculated spectrum (trace (a)) based on the bound states calculation for the PESs of Kłos et al. in Ref. [72]. The spectrum is calculated assuming a rotational temperature of 1.2 K, which allows for noticeable contributions from levels with an energy up to around 3.8 $\text{cm}^{-1}1$. Note that the next higher levels have energies of at least 5 $\text{cm}^{-1}1$. Interestingly, these findings could explain the observed smaller binding energy found by Holmes-Ross et al.[29]

The experimental spectrum of NO-He consists of two groups of lines centered around the NO monomer lines $\text{Q}_{11}(0.5)$ and $\text{R}_{11}(0.5)$. Thus, they can be classified as either preserving the approximate quantum number j_{NO} or changing it by one unit. Within these two groups, the lines separate into additional sets reflecting the change in the approximate orbital quantum number L. As such they provide clear evidence for transitions with $\Delta L = 0, \pm 1$, and $+2$. Similar to normal rotational branches, transitions with $\Delta L = -1$ are located to the red of the NO monomer lines while transitions with $\Delta L = 0$ and $+1$ are near or to the blue, respectively.

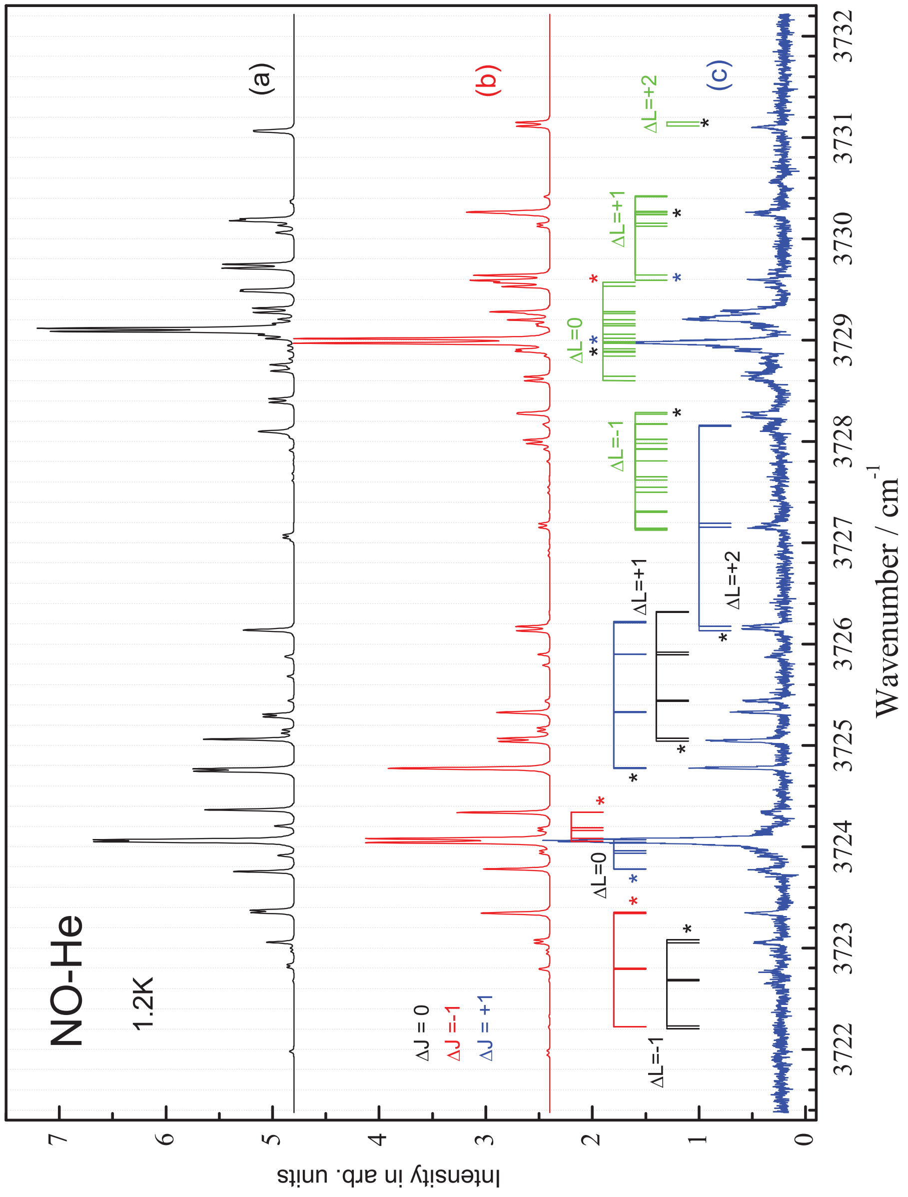

Figure 4.5 Comparison of calculated spectra using the original results of the CC calculations (trace (a)) and using modified energy levels (trace(b)) with the experimental spectrum (trace(c)). Frequency combs identify standard rotational branches ($\Delta J = -1$ red, $\Delta J = 0$ black, and $\Delta J = +1$ blue), which, in addition, are labeled with the simultaneous change in the approximate quantum number L. Lines accessing higher lying energy levels are only identified through frequency combs (green) distinguishing the change in L.

For the j_{NO} preserving lines, we can distinguish further standard rotational branches characterized by the simultaneous change in total angular momentum J: $\Delta J = 0$, ± 1. The associated frequency combs are indicated in Fig. 4.5 using different colors: $\Delta J = -1$ (red), $\Delta J = 0$ (black), and $\Delta J = +1$ (blue). Note that for each marked transition in fact two lines with different parity contribute. Especially, the first members, marked with asterisks in Fig. 4.5, show a noticeable parity splitting. In most cases, only the first two members of the branch are actually observed in the spectrum. Furthermore, we did not show the two branches for transitions with $\Delta J = 0$ and $\Delta L = 0$, which are responsible for the intense but unresolved peak at the position of the monomer line $Q_{11}(0.5)$.

For the lines near the monomer $R_{11}(0.5)$ line, we can also distinguish groups associated with different ΔL-transitions, in particular $\Delta L = 0, \pm 1$. Because these transitions access high lying levels near the dissociation limit, many sub-branches with well defined changes in ΔJ and ΔL have only one member. Therefore, we only display in Fig. 4.5 frequency combs for the groups of lines with $\Delta L = 0, \pm 1$. In addition, transitions starting in the lowest levels are marked with asterisks.

The overall agreement between the two spectra is excellent. The calculated line positions and patterns provide convincing evidence for the assignment of the experimental spectrum to the NO-He complex. Most line positions are reproduced within a tenth of a wavenumber. Slightly larger deviations are found for the group of lines around the frequency of the monomer line $R_{11}(0.5)$.

We assess the deviations quantitatively by generating a spectrum (trace (b) in Fig. 4.5) based on the modification of individual energy levels in order to improve the agreement with the experimental spectrum. In this way, it is possible to reproduce all lines observed in the experimental spectrum. In Fig. 4.6, the resulting energy levels (shown red) are compared with the calculated ones shown in black. Especially levels with $j_{NO} = 0.5$ show very small deviations while some of the higher energy levels with $j_{NO} = 1.5$ indicate larger deviations.

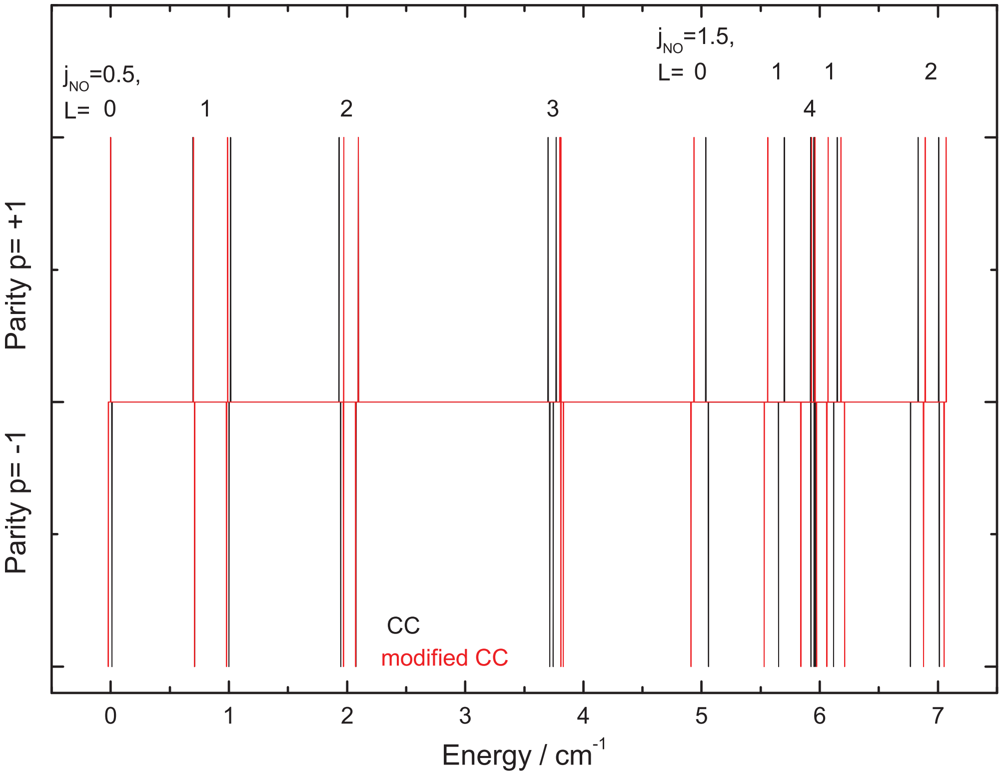

Figure 4.6 Comparison of calculated CC energy levels (black) in cm^{-1} with the modified energy levels (red), which reproduce the experimental spectrum. Levels with positive parity are shown in the upper half while the corresponding levels with negative parity are displayed in the lower half. For different groups of levels, the approximate quantum numbers j_{NO} and L are given in the top part of figure.

Nevertheless, the overall good agreement clearly demonstrates the high quality of the set of *ab initio* PESs of Ref. [72].

4.4 CONCLUSIONS

In this article, we describe the first measurement of a bound state spectrum of the NO-He complex associated with the first vibrational overtone of the NO monomer. The spectrum is detected through UV excitation into the NO $\tilde{A}$-state dissociation continuum. This method allows the detection of the complex despite the fact that no bound spectrum involving the $\tilde{A}$-state is known or even exists. Furthermore, it takes advantage of the increased Franck-Condon factors associated with the excitation into the continuum. Because ultimately a NO monomer ion is detected, there is a possible ambiguity in regards to the origin of such a signal. It turns out that complexes of NO-Ne and NO-Ar have rich and intense near IR spectra, which excludes these rare gases as seed gases for a molecular beam expansion targeting, for example, a complex of NO with a closed shell molecule.

In this work, we have demonstrated that we can generate cold molecular beams with He as a seed gas. We also find that, in contrast to NO-Ne and NO-Ar, the near-IR spectrum of NO-He is sparse and weak. The combination of these characteristics enables us to employ the method of $\tilde{A}$-state dissociation detection to the recording of near IR spectra of other NO complexes, in particular, with molecular partners.

The experimental spectrum of NO-He agrees very well with a spectrum based on a full quantum mechanical CC calculation using the set of PESs of Reference [72] in combination with an approximate linestrength. The good agreement confirms not only the assignment to the NO-He complex, but also the quality of the *ab initio* PESs.

4.5 Acknowledgements

The authors would like to thank Millard Alexander for his encouragement and many discussions. J. K. is grateful to the US National Science Foundation for financial support under Grant No. CHE-1565872 to Millard Alexander. V. B., S. Z. and H. M. gratefully acknowledge the financial support provided by the National Science Foundation under grant No. CHE-0957260. We also would like to thank G.E. Hall and W.H. Lawrance for providing us with the data of the photodissociation cross sections for the NO - rare gas systems.

Chapter 5

REMPI detected mm-wave absorption: CO Results

5.1 Motivation

Information about how components of a complex rotate and how freely that rotation occurs can be determined by observing rotational spectra. However, purely rotational lines are challenging to identify. IR-UV spectroscopy can provide partially resolved rotational structure, but the complexity makes its analysis difficult. Using just mm-waves would provide fully resolved rotational structure, but these photons contain hardly any energy and are very difficult to detect on their own. Combining mm-waves with resonance-enhanced multiphoton ionization (REMPI) detection, even weak mm-wave absorption is observable through ion detection in combination with electron amplification in a microchannel plate detector (MCP).

5.2 Experimental Setup

In our experiment, a molecular beam is generated when a gas mixture adiabatically expands into vacuum. The mm-waves are vertically polarized and aligned anti-parallel to the molecular beam resulting in longer interaction times. The mm-wave absorption is detected by probing one of the involved energy levels with single color REMPI.

The setup was tested and optimized by observing mm-wave absorption of CO. The lowest rotational transition of CO at 115 GHz is probed with REMPI via the electronic C $^1\Sigma^+$ state and electronic B $^1\Sigma^+$ state. Both the observed depletion of the lower energy level as

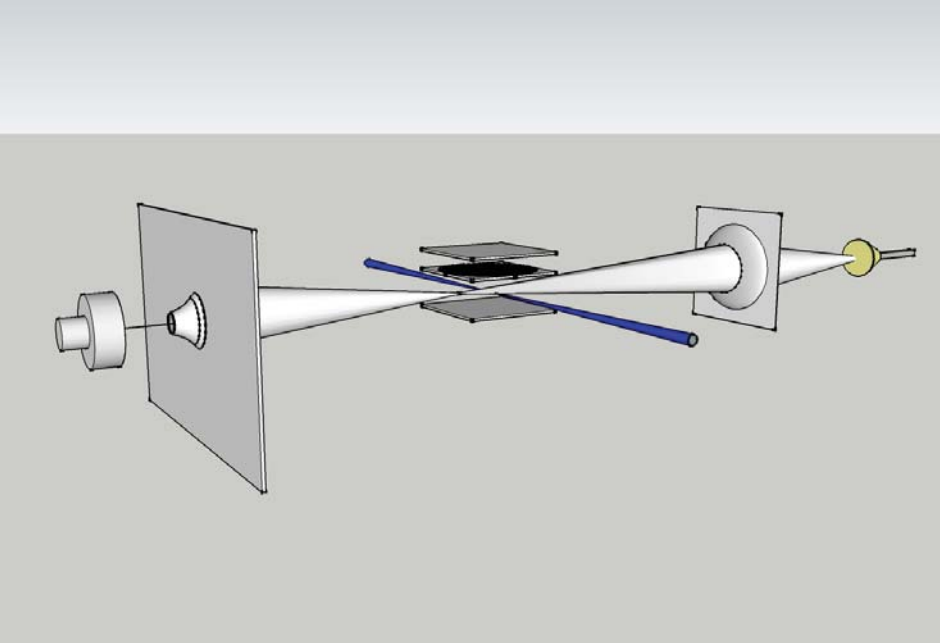

Figure 5.1 Test Apparatus Schematic showing the molecular beam passing through a skimmer from the left, mm-waves focused by a lens on the right, and a UV beam intersecting perpendicularly.

well as the enhancement of the excited level indicate strong saturation of the transition. The transitions observed can be seen in Figure 5.2.

5.3 Results

5.3.1 Saturation Effect

During the experiment, we observed large, broad peaks which will be called "Doppler Profiles". After reducing the millimeter wave power, we could see that full power was causing a saturation effect, as seen in Figure 5.3. Calculating the percent saturation for the R(0) line

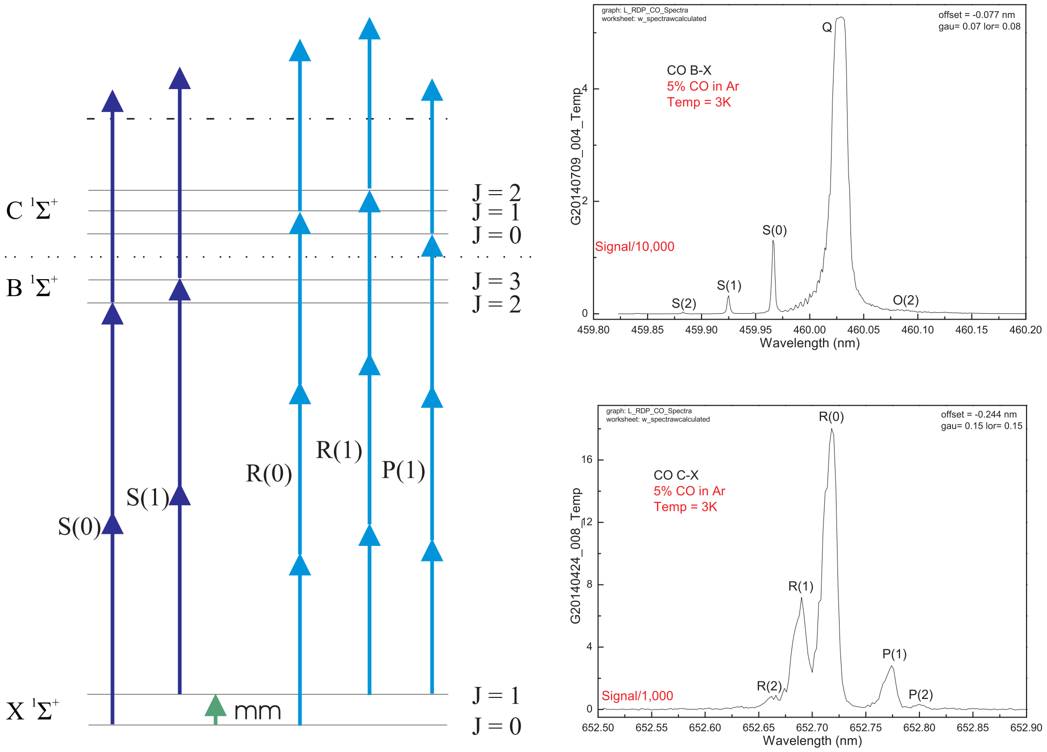

Figure 5.2 CO B-X(86,945.2 cm^{-1}): 2+1 REMPI ≈ 230 nm (43,478 cm^{-1}). mm-wave = 115.271201796 GHz (3.8450314 cm^{-1} = 2.600759 mm). CO C-X(91,916.5 cm^{-1}): 3+1 REMPI ≈ 326 nm (30,675 cm^{-1}). mm-wave = 115.27097 GHz (3.8450236 cm^{-1} = 2.6007642 mm)

in an Ar beam at 3K, we obtain:

$$\frac{N_1(\infty) - N_1(0)}{N_1(0)} * 100 = -42\% \tag{5.1}$$

We see a greater depletion than this in the Doppler profiles in the Figure 5.3.

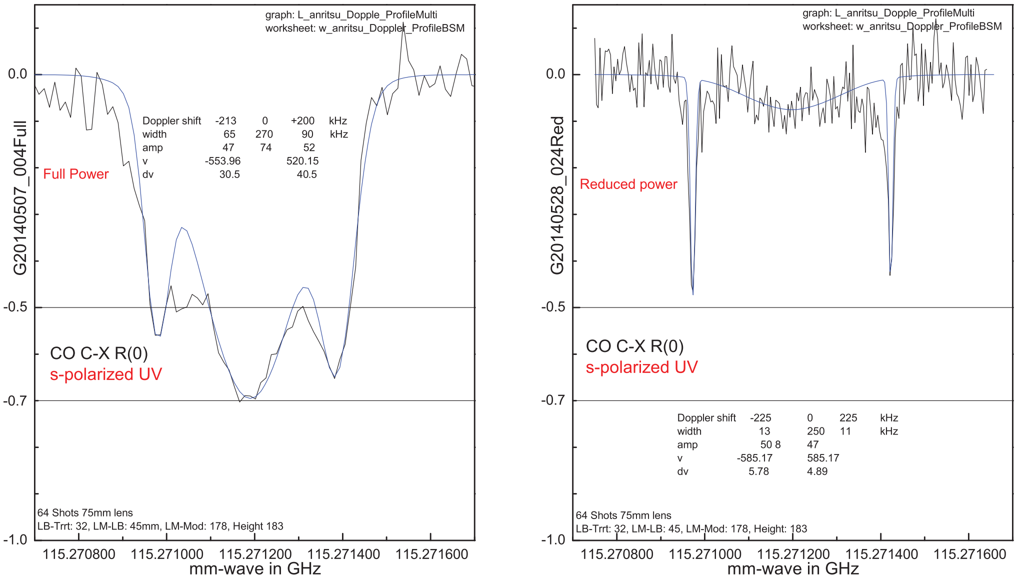

Figure 5.3 Example of Saturation effect: CO C-X R(0) in Ar. Full Power (left) $> 50\%$. Reduced Power (right) $\leq 50\%$.

5.3.2 Beam Velocity and Doppler Effect

When the molecular beam leaves the nozzle, the beam begins to spread out based on the velocity distribution. Over time, the faster molecules will be in front while the slower ones will be at the end of the pulse. This can be observed by changing the molecular beam delay, faster molecules observed by larger delay while slower molecules observed with a smaller delay. Additionally, changing the concentration of the molecule in the carrier gas also affects the velocity distribution. As seen below, a lower concentration causes the molecules to be faster, thus the delay needs to be adjusted accordingly. All of these velocity's were calculated by using the Doppler Effect equation and taking into account the directions of the mm-waves and molecular beam, where the frequency observed by the molecular beam

(f) is the resonance frequency.

$$v = c\left(\frac{f}{f_0} - 1\right) \tag{5.2}$$

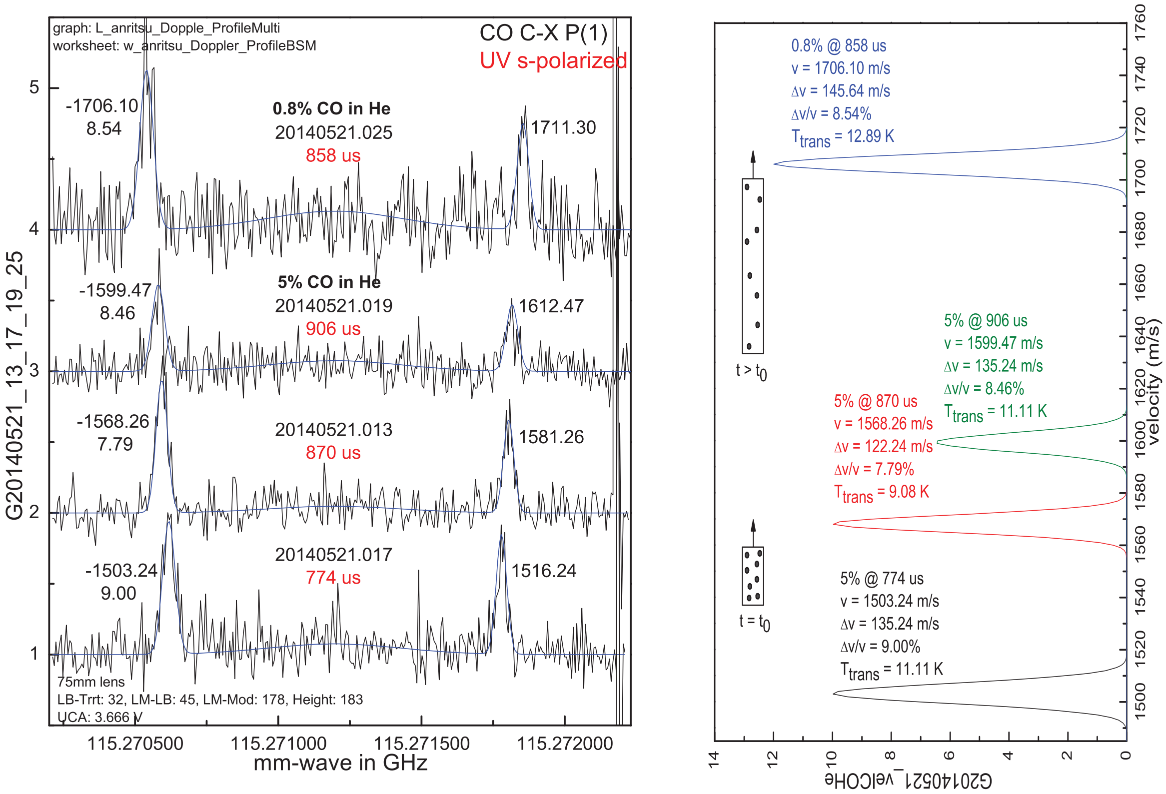

Figure 5.4 He expansion Doppler profiles on P(1) line. Reduced power: UCA 3.666V. Speed of molecular beam at different beam delays: 774, 870, and 906 μs (5%) and 858 μs (0.8%). 5% FWHM: 774-902 μs. 0.8% FWHM: 778-922 μs.

5.3.3 POLARIZATION DEPENDENCE

Rotating the UV polarization using a Fresnel Rhomb revealed a polarization effect for the P(1) and R(1) lines. This polarization effect can be examined mathematically using Euler angles and the rotation operator to rotate the millimeter waves onto the UV. Using $j_i = 1$ and $m = 0$ and using the selection rule of linear polarization of $m = m'$:

$$\hat{\mathrm{D}}(\alpha,\beta,\gamma)\,|jm\rangle = \sum_{m'} \exp(-i\alpha m')\mathrm{d}^{(1)}_{m'0}(\beta)\,|1m'\rangle \tag{5.3}$$

$$\text{s-pol UV:} \qquad \alpha = 90^o \quad \beta = \gamma = 0^o$$

$$\mathrm{P}(1)\ m' = 0 \ : \ |10\rangle \tag{5.4}$$

$$\mathrm{R}(1)\ m' = 0, \pm 1 \ : \ |10\rangle \tag{5.5}$$

$$\text{p-pol UV:} \qquad \alpha = 180^o \quad \beta = \gamma = -90^o$$

$$\mathrm{P}(1)\ m' = 0 \ : \ 0 \tag{5.6}$$

$$\mathrm{R}(1)\ m' = 0, \pm 1 \ : \ -\frac{1}{\sqrt{2}}\left(|11\rangle + |1-1\rangle\right) \tag{5.7}$$

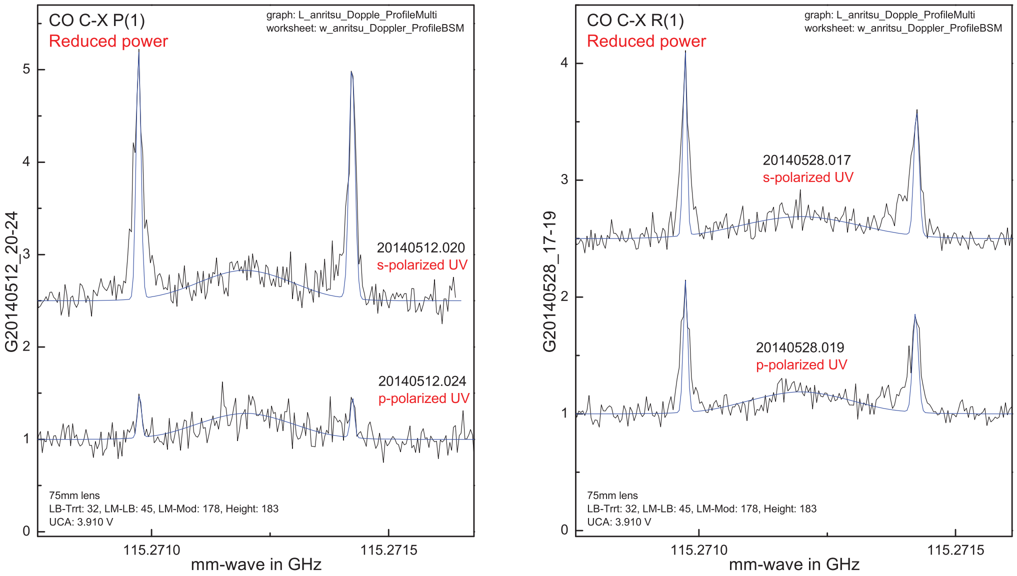

Figure 5.5 Reduced power: Polarization effect observed for P(1) and R(1) lines.

5.3.4 Rabi Oscillations

Additionally, Rabi Oscillations were observed while scanning the millimeter wave power. Assuming a π-pulse with a flat-top intensity profile having an interaction time of 150 μs, the frequency is found to be:

$$\Omega_r = \frac{\pi}{\tau} = \frac{\pi}{150\ \mu\text{s}} = 20.944\ \text{kHz} \tag{5.8}$$

With a beam waist of 1.5 cm and the dipole moment of ground state CO being 0.11 D ($J = 0$ and $M = 0$):

$$\mu_{ab} = \left(\sqrt{\frac{(J+1)^2 - M^2}{(2J+1)(2J+3)}}\right)\mu = \sqrt{\frac{1}{3}}\mu = 0.064\ \text{D}$$

$$P = \frac{\pi \text{w}_0^2 I_0}{2} \tag{5.9}$$

$$I_0 = \frac{c}{8\pi}|E|^2 \quad \text{(cgs Gaussian units } 4\pi\epsilon_0 \to 1) \tag{5.10}$$

$$E = \frac{\Omega_r \hbar}{\mu_{ab}} \tag{5.11}$$

$$P = \frac{c\text{w}_0^2}{16}\left|\frac{\Omega_r \hbar}{\mu_{ab}}\right|^2 = 509.8\frac{\text{erg}}{\text{s}} = 50.98\ \mu\text{W} \tag{5.12}$$

5.3.5 Full Power Line Profile

When looking at these profiles with full power, we notice that the middle peak is not affected by the polarization effect. This leads to wondering where exactly this middle portion comes from in the machine.

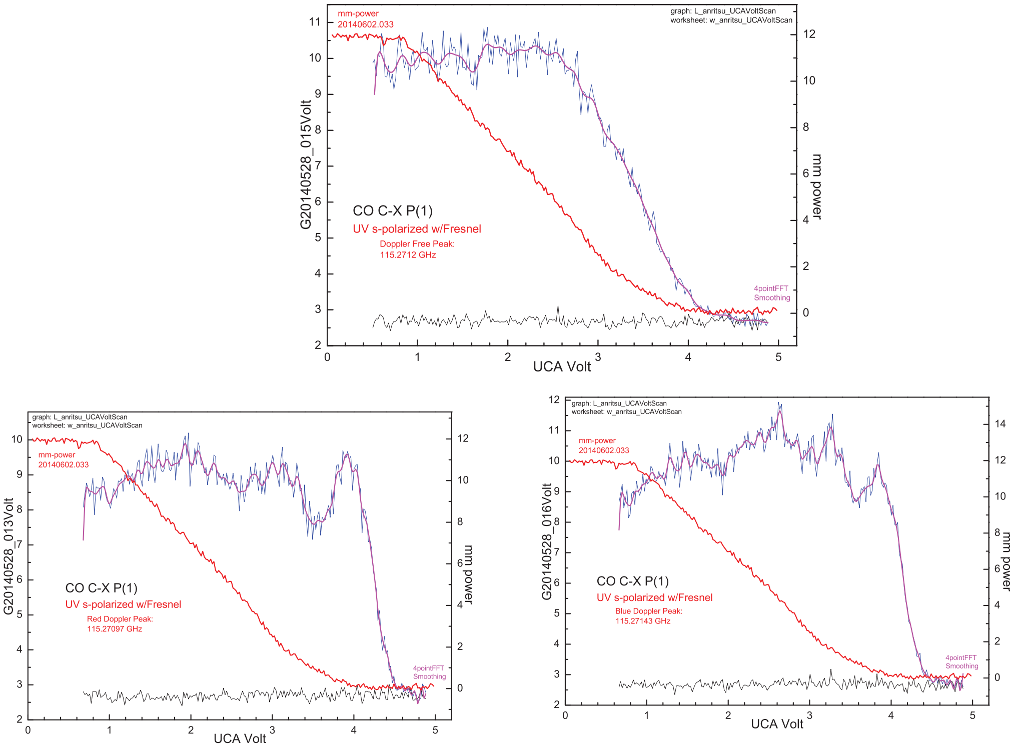

Figure 5.6 5% CO in Ar: UCA Voltage Scan of Doppler Free Region (top), Red Shifted peak (left), and Blue Shifted peak (right) plotted with mm-wave output power as measured by a pyroelectric sensor. Rabi Oscillations of the Red and Blue Shifted Doppler peak are observed.

5.3.6 FREQUENCY MODULATION

So where does this Doppler free region come from in the machine? Frequency modulation (FM) was used to generate the figure below. Using the speed of Ar in vacuum as 590 m/s, we see that the free component is about 15 μs long $\approx$ 9mm, which is about the length of the skimmer. This makes sense due to the shape of the skimmer causing millimeter waves with undefined $\vec{k}$ vectors, some of which could be perpendicular to the molecular beam as

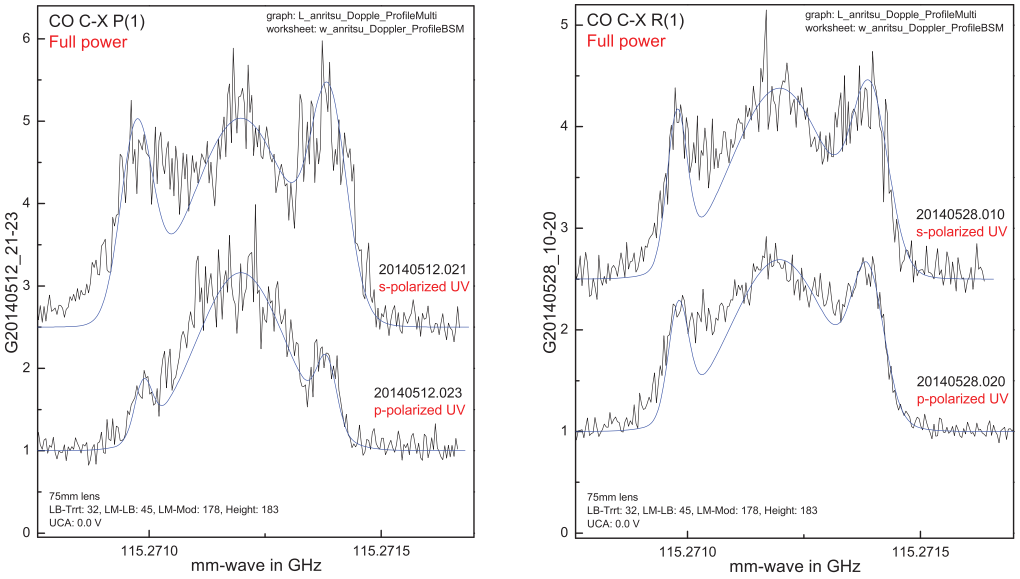

Figure 5.7 Full power: Polarization effect not seen in the Doppler Free region

opposed to antiparallel as was assumed in the polarization calculation. The red component begins about 30 μs (18mm) before the free component. Blue component starts after the free component when the mm-waves have had time to reflect off of the skimmer back onto the molecular beam.

5.4 CONCLUSIONS

- Saturation Effect (all) and Polarization effect (P(1) & R(1)) observed
- Rabi Oscillations observed for Red and Blue Doppler peaks
- Observed velocity distribution of He beam
- FM employed to distinguish origin of Doppler signals

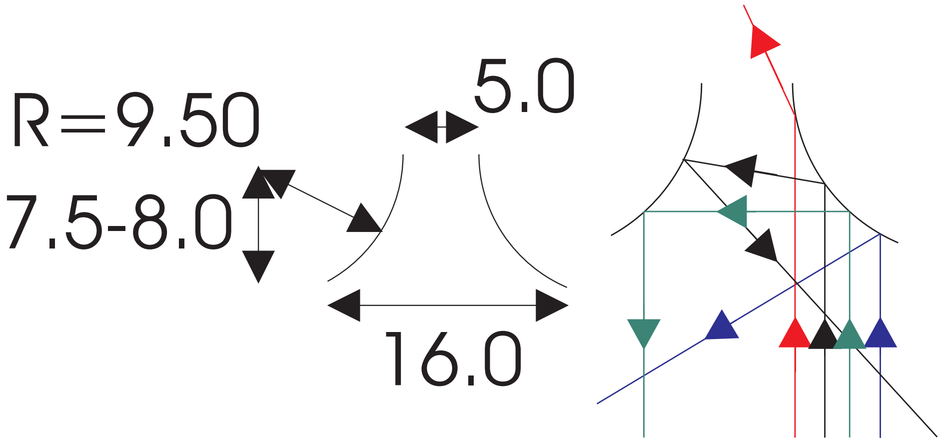

Figure 5.8 Skimmer showing dimensions in mm (left). Skimmer showing possible reflections of the mm-waves: 29^o, 45^o & 45^o, 50^o & 19^o, and 77^o (right).

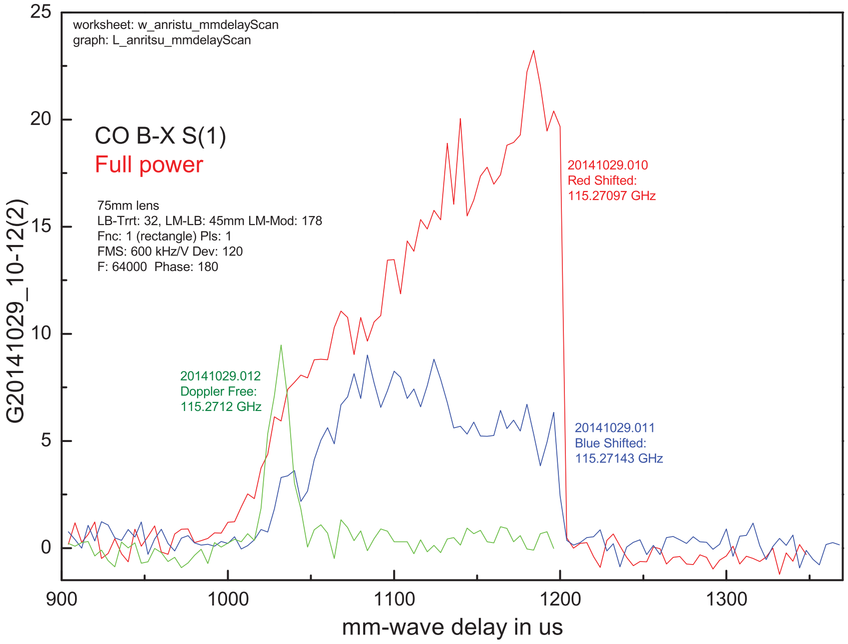

Figure 5.9 mm-wave beam delay scan held constant at Doppler Free (green), Red Shifted (red), and Blue Shifted (blue) resonance frequencies.

Chapter 6

Conclusion

In this thesis, techniques for detecting IR and mm wave absorption are explored. Initially, I explored vacuum system techniques and experimental setups used to collect data. Then, chapter 3 demonstrates the effectiveness of measuring the near IR spectrum of NO-X complexes through excitation into the dissociation continuum of NO-Ne. Due to the electronic $\tilde{A}$-state of the complex being shifted to larger intermolecular distances than the ground state, exciting into the $\tilde{A}$-state continuum offers enhanced Franck-Condon factors. There was also better signal-to-noise ratio and spectral resolution as compared to other techniques. In chapter 4, I show documentation of the first measured near IR spectrum of NO-He in the region of the first NO overtone transition. The IR absorption was measured by fixing the UV such that if vibration excitation occurred, the UV would then excite the complex into the $\tilde{A}$-state continuum. The spectra for NO-He is very weak with less rotational lines populated as opposed to NO-Ar and NO-Ne, which causes He to be best suited as a seed gas for studying NO-X complexes. Caution must be used with He because it is a light atom, meaning collisional cooling will not be as efficient as for Ne or Ar. Higher backing pressures and smaller concentrations of the molecules in the gas will allow for cooler temperatures. The next chapter details the testing of a new experimental setup to preform mm-UV double resonance experiments. This new technique of measuring mm-wave absorption through REMPI allows analysis of fully resolved rotational structure.

BIBLIOGRAPHY

[1] *Vacuum Technology: It's Foundations, Formulae and Tables*, Leybold-Heraeus (1972).

[2] Y. Kim, J. Fleniken, and H. Meyer, J. Chem. Phys. **114**, 5577 (2001).

[3] H. L. Holmes-Ross, R. J. Valenti, H. G. Yu, G. Hall, and W. D. Lawrance, J. Chem. Phys. **144**, 044309 (2016).

[4] K. P. Huber and G. Herzberg, *Molecular Spectra and Molecular Structure, IV. Constants of Diatomic Molecules* (Van Nostrand Reinhold, New York, 1979).

[5] E. Miescher and K. P. Huber, in *International Review of Science, Physical Chemistry Series Two*, Vol. 3, edited by D. A. Ramsay (Oxford University Press, Butterworths, London, 1976) p. 37–74.

[6] H. Joswig, P. Andresen, and R. Schinke, J. Chem. Phys. **85**, 1904 (1986).

[7] M. Mons and I. Dimicoli, Chem. Phys. **130**, 307 (1989).

[8] H. Meyer, J. Chem. Phys. **107**, 7721 (1997).

[9] Y. Kim and H. Meyer, Int. Rev. Phys. Chem. **20**, 219 (2001).

[10] A. Bondi, J. Phys. Chem. **68**, 441 (1964).

[11] H. Meyer, J. Chem. Phys. **136**, 204308 (2012).

[12] B. Wen, Y. Kim, H. Meyer, J. Kłos, and M. Alexander, J. Phys. Chem. A **112**, 9483 (2008).

[13] J. Moore, C. Davis, and M. Coplan, *Building Scientific Apparatus: A Practical Guide to Design and Construction* (Addison-Wesley, 1989).

[14] W. Gentry, in *Atomic and Molecular Beam Methods*, Vol. 1, edited by G. Scoles (Oxford University Press, New York, 1988) p. 54–82.

[15] *Quanta-Ray Lab-Series Pulsed Nd:YAG Lasers User's Manual*, Spectra-Physics (2003).

[16] *Single-Frequency Injection Seeding Laser User's Manual*, Continuum (1994).

[Man] *User Manual Pulsed Dye Laser LDL 105/205*, Laser Analytical System GmbH.

[17] *Operation and Maintenance Manual for the Mirage 3000 and 3000B Laser*, Continuum (1993).

[18] K. Sato, Y. Achiba, H. Nakamura, and K. Kimura, J. Chem. Phys. **85**, 1418 (1986).

[19] J. Miller and W. Cheng, J. Phys. Chem. **89**, 1647 (1985).

[20] D. Bergeron, A. Musgrave, R. Gammon, V. Ayles, J. Silber, T. Wright, B. Wen, and H. Meyer, J. Chem. Phys. **124**, 214302 (2006).

[21] B. Wen, H. Meyer, V. Ayles, A. Musgrave, D. Bergeron, J. Silber, and T. Wright, Phys. Chem. Chem. Phys. **10**, 375 (2008).

[22] K. Tsuji, K. Shibuya, and K. Obi, J. Chem. Phys. **100**, 5441 (1994).

[23] M. McQuaid, G. Lemire, and R. Sausa, Chem. Phys. Lett. **227**, 54 (1994).

[24] J. Miller, J. Chem. Phys. **86**, 3166 (1987).

[25] S. Gamblin, S. Daire, J. Lozeille, and T. Wright, Chem. Phys. Lett. **325**, 232 (2000).

[26] P. Langridge-Smith, E. C. M., and D. H. Levy, J. Chem. Phys. **74**, 6513 (1981).

[27] D. S. Wright, H. L. Holmes-Ross, and W. D. Lawrance, Chem. Phys. Lett. **435**, 19 (2007).

[28] W. G. Roeterdink, K. E. Strecker, C. C. Hayden, M. Janssen, and D. W. Chandler, J. Chem. Phys. **130**, 134305 (2009).

[29] H. L. Holmes-Ross and W. D. Lawrance, J. Chem. Phys. **135**, 014302 (2011).

[30] W. Hopkins, M. Lipciuc, S. Gardiner, and C. Vallance, J. Chem. Phys. **135**, 034308 (2011).

[31] V. Ayles, R. Plowright, M. Watkins, T. Wright, J. Kłos, M. Alexander, P. Pajón-Suárez, J. Rubayo-Soneira, and R. Hernández-Lamoneda, Chem. Phys. Lett. **441**, 181 (2007).

[32] H. Thuis, S. Stolte, J. Reuss, J. van den Biesen, and C. van den Meijdenberg, Chem. Phys. **52**, 211 (1980).

[33] J. Fleniken, Y. Kim, and H. Meyer, J. Chem. Phys. **109**, 8940 (1998).

[34] M. Alexander, P. Soldán, T. Wright, Y. Kim, H. Meyer, P. Dagdigian, and E. Lee, J. Chem. Phys. **114**, 5588 (2001).

[35] Y. Sumiyoshi and Y. Endo, J. Phys. Chem. A **114**, 4798 (2010).

[36] J. Rezac, L. Simova, and P. Hobza, J. Chem. Theory Comput. **9**, 364 (2013).

[37] H. Cybulski and B. Fernández, J. Phys. Chem. A **116**, 7319 (2012).

[38] A. von Zastrow, J. Onvlee, S. Vogels, G. Groenenboom, A. van der Avoird, and S. van de Meerakker, Nat. Chem. **6**, 216 (2014).

[39] Y. Kim, H. Meyer, and M. Alexander, J. Chem. Phys. **121**, 1339 (2004).

[40] M. Brouard, H. Chadwick, C. Eyles, B. Hornung, B. Nichols, J. Scott, F. Aoiz, J. Kłos, S. Stolte, and X. Zhang, Mol. Phys. **111**, 1759 (2013).

[41] O. Ershova, J. Kłos, N. A. Besley, and T. Wright, J. Chem. Phys. **142**, 034311 (2015).

[42] L. Uranga-Piña, C. Meier, and J. Rubayo-Soneira, J. Chem. Phys. **135**, 164504 (2011).

[43] C. Jeannin, M. T. Portella-Oberli, S. Jimenez, F. Vigliotti, B. Lang, and M. Chergui, Chem. Phys. Lett. **316**, 51 (2000).

[44] F. Vigliotti, L. Bonacina, M. Chergui, G. Rojas-Lorenzo, and J. Rubayo-Soneira, Chem. Phys. Lett. **362**, 31 (2002).

[45] H. Meyer, J. Chem. Phys. **101**, 6686 (1994).

[46] H. Meyer, J. Chem. Phys. **101**, 6697 (1994).

[47] Y. Kim, S. Ansari, B. Zwickl, and H. Meyer, Rev. Sci. Instr. **74**, 4805 (2003).

[ger] The original piezoelectric pulsed molecular beam valve was developed in the group of Prof. D. Gerlich at the University of Chemnitz, Germany.

[48] C. Amiot, R. Bacis, and G. Guelachvili, Can. J. Phys. **56**, 251 (1978).

[49] A. Pine, J. Johns, and A. Robiette, J. Mol. Spectrosc. **74**, 52 (1979).

[50] J. Danielak, U. Domin, R. Kępa, M. Rytel, and M. Zachwieja, J. Mol. Spectrosc. **181**, 394 (1997).

[hmw] Details of the modification, electronic hardware, and wavelength calibration are given at https://www.physast.uga.edu/research/meyer-group/laser-controllers.

[51] W. H. Green and M. I. Lester, J. Chem. Phys. **96**, 2573 (1992).

[52] M. L. Dubernet, P. A. Tuckey, and J. Hutson, Chem. Phys. Lett. **193**, 355 (1992).

[53] H. Meyer, J. Kłos, and M. H. Alexander, J. Phys. Chem. A **117**, 11906 (2013).

[54] M. Heaven, Ann. Rev. Phys. Chem. **43**, 243 (1992).

[55] A. Schiffman and D. Chandler, Int. Rev. Phys. Chem. **014**, 371 (1995).

[56] D. Chandler and S. Stolte, in *Gas Phase Molecular Reaction and Photodissociation Dynamics*, edited by K. Lin and P. Kleiber (Transworld Research Network, Kerala, 2007) p. 1–63.

[57] Y. Sumiyoshi and Y. Endo, J. Chem. Phys. **127**, 184309 (2007).

[58] J. Kłos, S. G. Zhang, and H. Meyer, J. Chem. Phys. **144**, 114307 (2016).

[59] B. Wen, H. Meyer, J. Kłos, and M. H. Alexander, J. Phys. Chem. A **113**, 7366 (2009).

[60] J. Kłos and M. Alexander, J. Phys. Chem. Lett. **5**, 3296 (2014).

[61] J. Kłos, F. Aoiz, M. Menéndez, M. Brouard, H. Chadwick, and C. Eyles, J. Chem. Phys. **137**, 014312 (2012).

[62] J. Onvlee, S. Vogels, A. van der Avoird, G. C. Groenenboom, and S. T. van de Meerakker, New J. Phys. **017**, 055019 (2015).

[63] B. F. Parsons, D. W. Chandler, E. C. Sklute, and E. Wade, J. Phys. Chem. A **108**, 9742 (2004).

[64] H. L. Holmes-Ross and W. D. Lawrance, Chem. Phys. Lett. **458**, 15 (2008).

[65] G. C. Nielson, G. Parker, and R. Pack, J. Chem. Phys. **64**, 2055 (1976).

[66] M. H. Alexander, Chem. Phys. **92**, 337 (1985).

[67] G. Corey and M. Alexander, J. Chem. Phys. **85**, 5652 (1986).

[68] M. Yang and M. H. Alexander, J. Chem. Phys. **103**, 6973 (1995).

[69] H. Meyer, J. Chem. Phys. **102**, 3151 (1995).

[70] E. P. F. Lee and T. G. Wright, J. Chem. Phys. **109**, 157 (1998).

[71] T. N. Zolotoukhina and S. Kotake, J. Chem. Phys. **99**, 2855 (1993).

[72] J. Kłos, G. Chalasinski, M. T. Berry, R. Bukowski, and S. M. Cybulski, J. Chem. Phys. **112**, 2195 (2000).

[73] M. Keil, J. T. Slankas, and A. Kuppermann, J. Chem. Phys. **70**, 541 (1979).

[74] E. Polyakova, D. Stolyarov, and C. Wittig, J. Chem. Phys. **124**, 214308 (2006).